Microwave Sensing, Signals and Systems (MS3)
Mekelweg 4,
2628 CD Delft
The Netherlands
https://radar.tudelft.nl

MS3-2025-5913101

M.Sc. Thesis

Design of Sparse MIMO Radar Antenna Arrays Using DPS with Integrated CRB Evaluation

Jiaqi Li

Faculty of Electrical Engineering, Mathematics and Computer Science
Delft University of Technology

Design of Sparse MIMO Radar Antenna Arrays Using DPS with Integrated CRB Evaluation

Thesis

submitted in partial fulfillment of the
requirements for the degree of

Master of Science

in

Electrical Engineering

by

Jiaqi Li
born in Shijiazhuang, China

This work was performed in:

Microwave Sensing, Signals and Systems (MS3) Group
Department of Microelectronics
Faculty of Electrical Engineering, Mathematics and Computer Science
Delft University of Technology

Delft University of Technology
Department of
Microelectronics

The undersigned hereby certify that they have read and recommend to the Faculty of Electrical Engineering, Mathematics and Computer Science for acceptance a thesis entitled **“Design of Sparse MIMO Radar Antenna Arrays Using DPS with Integrated CRB Evaluation”** by **Jiaqi Li** in partial fulfillment of the requirements for the degree of **Master of Science**.

Dated: June 23th, 2025

Chairman: ______________________

dr. F. Fioranelli

Advisors: ______________________

Arie G.C. Koppelaar

____

Anusha Ravish Suvarna

Committee Members: ______________________

dr. G. Joseph

Abstract

This thesis presents a novel approach based on Joint Deep Probabilistic Subsampling with Cramér-Rao Lower Bound Integration (J-DPSC) for sparse antenna array design in distributed radar systems. The method addresses the critical challenge of achieving high angular resolution in autonomous driving applications while maintaining low hardware complexity. The proposed J-DPSC framework extends Deep Probabilistic Subsampling with theoretical foundations based on worst-case dual-target Cramér-Rao Lower Bound analysis. This enables simultaneous optimization of both transmitter and receiver arrays across mono-static, bi-static, and joint operational modes. A Neighborhood Masking Mechanism ensures physical realizability of the designed arrays.

Extensive simulations validate that our proposed sparse arrays achieve performance comparable to fully populated arrays while using significantly fewer elements. The results demonstrate peak sidelobe levels up to -10 dB with minimal resolution sacrifice ($\leq 0.1°$) for two-sensor distributed radar networks. The approach allows extension to three-sensor configurations for potential applications with multi-node networks. Monte Carlo evaluations across varying SNR levels and source (i.e., targets) separations show consistent superiority over random selection methods.

Summarizing, this work advances sparse array design methodology by bridging machine learning techniques with estimation theory, enabling a more generalized and flexible design tool for distributed radar networks in next-generation autonomous driving applications.

Acknowledgments

I never imagined this moment would come so quickly. Writing acknowledgments is a key indicator that I am about to complete my two-year master's program in the Netherlands. Looking back to the day I was ready to take flight from Beijing, life in the Netherlands seemed both attractive and mysterious to me. At this moment, I can confidently say it was the right choice, providing me with an excellent journey through both academic and life experiences.

Turning to the main topic, I would like to thank NXP for giving me the opportunity to conduct my master's thesis at this leading automotive radar company. In particular, I would like to express my deep gratitude to my supervisor Arie Koppelaar, who has been tremendous support throughout this journey. He is an exceptionally kind person who always answers my questions promptly and provides interesting insights for my further exploration. His careful review of my reports, reading every word I wrote with meticulous attention, exemplifies a level of dedication I never expected from such an experienced professional. Working with him has been effortless since he is always open to discussion and willing to listen, and his sense of humor creates a wonderful working atmosphere. I have learned tremendously from our discussions, particularly regarding career development, which has been invaluable.

I would like to express my sincere thanks to my daily supervisor Anusha Ravish Suvarna at NXP. Despite our similar ages, her knowledge and technical expertise far exceed mine, and I have learned immensely from her guidance. She can quickly target mistakes I missed during my thesis work, ensuring I stay on the right track, for which I am deeply grateful. She has also shared her own experiences and insights regarding thesis work, providing great assets that I could not have gained independently.

I would like to thank my supervisor Prof. Francesco Fioranelli for providing me with the opportunity to pursue my thesis in his research group, Microwave Sensing, Signals and Systems. Without your support, the work at NXP could not have been completed. I am constantly inspired by your enthusiastic energy for research. You have guided me to think about the motivation and fundamental principles behind technical aspects, teaching me to see the big picture rather than getting lost in details. I truly appreciate your careful examination of my reports and conference papers, which has helped me tremendously. Every discussion with you has provided valuable insights for my career development. It was definitely the right choice to visit your office and get to know you—you are not only a great supervisor but also a great friend.

I would also like to thank Jeroen Overdevest from NXP, who provided career opportunities and suggestions for my future development. Many thanks to Jihwan Youn from NXP US, who provided insights that proved invaluable for my thesis. Special thanks to Iris Huijben and Hans van Gorp for enthusiastically replying to my emails about your work—without your help, I could not have understood it so quickly and correctly.

Finally, I wish to recognize all my friends—both those I met in the Netherlands and those scattered across the world—who have offered true companionship. My profound gratitude goes to my family, who have remained my basis of strength with their persistent support and belief in my potential, sustaining me through the challenges of this academic pursuit.

Jiaqi Li
Eindhoven, The Netherlands
June 23th, 2025

Acronyms

ADAS Advanced Driving Assistance System

BCS Bayesian Compressive Sensing

CNN Convolutional Neural Network

CRLB Cramér-Rao Lower Bound

DML Deterministic Maximum Likelihood

DoA Direction of arrival

DoD Direction of Departure

DPS Deep Probabilistic Subsampling

DPSC Deep Probabilistic Subsampling with CRB Integration

DTW Detection Tolerance Window

FFT Fast Fourier Transform

FoV Field-of-View

GA Genetic Algorithm

$\boldsymbol{J-DPSC}$ Joint Deep Probabilistic Subsampling with CRB Integration

L2S Learn-to-Select

MIMO Multiple Input Multiple Output

MLW Main Lobe Width

MRAs Minimum Redundancy Arrays

NMM Neighborhood Masking Mechanism

OMP Orthogonal Matching Pursuit

PSL Peak Side-lobe Level

RMSE Root Mean Square Error

SLL Side-lobe Level

SNR Signal-to-Noise Ratio

SVM Support Vector Machines

ULAs Uniform Linear Arrays

Contents

List of Figures

List of Tables

Introduction

1

In this chapter, we introduce the foundational aspects of our research on sparse antenna array design for automotive radar systems. We begin by exploring the motivation behind our work, highlighting the critical need for enhanced angular resolution in autonomous driving applications while meeting practical hardware constraints. Next, we clearly define our problem statement, focusing on the optimization of non-co-located transmitter and receiver configurations using the Cramér-Rao Lower Bound (CRLB). The comprehensive literature review examines radar networks, classical sparse array layouts, and both conventional and machine learning approaches to array optimization. Finally, we present our research novelty, introducing the proposed Joint Deep Probabilistic Subsampling with CRLB Integration (J-DPSC) approach that addresses key gaps in existing methodologies, before outlining the structure of the remaining part of the thesis.

1.1 Motivation

Over the past two decades, automotive radar has been a cornerstone of innovation in millimeter-wave technology, enhancing driver comfort and safety in both autonomous and human-driven vehicles. Applications like adaptive cruise control, lane change assistance, blind spot detection, and cross-traffic alerts rely on radar systems to extract crucial information—such as range, relative velocity, and direction of arrival (DoA)—by analyzing reflected EM waves from targets. Figure 1.1 shows various such radar subsystems that are used in Advanced Driving Assistance System (ADAS).

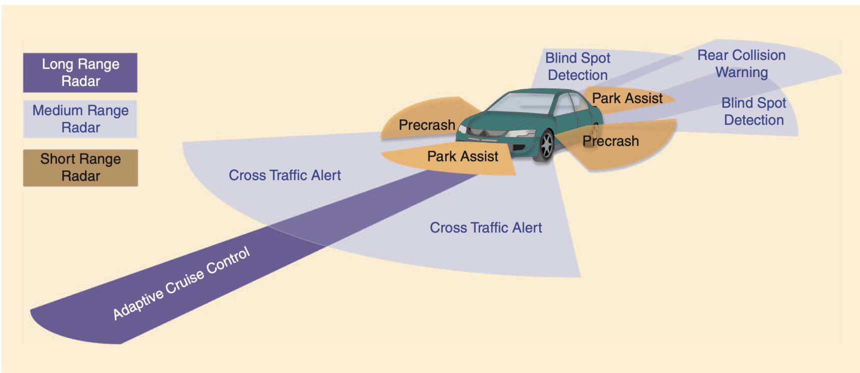

Figure 1.1: Radars for a variety of applications are used in an ADAS [1]

With the rising demand for autonomous driving, there is an increasing need for higher angular resolution and precision in object detection and prediction, especially in dense urban environments where safety is paramount. DoA estimation stands as a key component for accurate target detection and localization, directly impacting the system's ability to distinguish between closely spaced objects and track multiple targets simultaneously. High angular resolution enables vehicles to make reliable predictions about the trajectories of surrounding vehicles and pedestrians, facilitating safe navigation in complex traffic scenarios.

Achieving higher resolution in the angular domain typically requires a larger radar aperture; however, physical sensor size and placement constraints within vehicles limit this approach. Larger conventional arrays require more antenna elements, which increases system complexity, manufacturing costs, and power consumption. This creates a fundamental challenge: how to achieve high angular resolution while meeting low hardware cost and complexity for practical automotive implementation.

Multiple-Input Multiple-Output (MIMO) technology offers one solution by creating an effective aperture larger than the physical size would suggest, using virtual channels formed between transmit and receive antennas to enhance angular resolution. Building on this concept, sparse antenna array design emerges as a complementary approach. By strategically placing antenna elements with non-uniform spacing, rather than the conventional half-wavelength uniform spacing, sparse antenna arrays can achieve comparable performance to fully populated arrays while using significantly fewer elements. This approach maintains essential array capabilities with reduced hardware complexity by requiring fewer RF chains and ADC channels. The underlying principle relies on carefully designing the array geometry to minimize redundancy in spatial sampling while avoiding grating lobes and ambiguities in direction finding. Through mathematical optimization of element positions, sparse antenna arrays are particularly valuable for cost-sensitive automotive applications.

To address these limitations further, distributed radar systems have emerged as a promising extension of sparse antenna array concepts. By employing multiple smaller sensors across the fascia of a vehicle that work collaboratively, these systems can effectively simulate a larger aperture without the associated physical drawbacks. This approach offers advantages such as reduced sensor complexity, lower installation constraints, and the ability to perform precise estimations from a single measurement, thereby enhancing the overall performance of automotive radar in ADAS. For these reasons, improving the performance of coherent sensor networks from an algorithmic and signal processing perspective is a rich research area.

1.2 Problem statement

This thesis addresses the optimization of sparse antenna array designs in automotive applications through novel approaches. The research develops a general methodology applicable to arbitrary numbers of transmitters and receivers, demonstrating the broad value and scalability of our proposed framework. While our approach is universally applicable, we focus specifically on optimizing 4-transmitter and 4-receiver configurations within a single sensor platform, as this represents the current state-of-the-art sensor size for the NXP corner radar application. We use the Cramér-Rao Lower Bound as the primary theoretical foundation for our optimization framework.

The central challenge lies in developing efficient methods to determine optimal positioning for both transmit and receive antennas, allowing for flexible operation in either mono-static or bi-static sensing modes. Explicitly speaking, the algorithm should be able to deal with non-co-located array optimization for both transmitters and receivers. A general approach is expected to adapt to different types of distributed radar systems. It should be stressed that rather than focusing on complex antenna synthesis at the (physical) component level, this work emphasizes high-level antenna positioning optimization and corresponding beam pattern formation to achieve superior detection performance.

A key innovation of this research is the application of machine learning techniques, particularly Deep Probabilistic Subsampling (DPS) [2], to solve the optimization problem. This ML-driven approach enables the handling of larger and more complex antenna configurations while simultaneously reducing the computational complexity of the cost function evaluation. The thesis aims to demonstrate that our novel modification of Deep Probabilistic Subsampling can effectively achieve sparse array configurations design for distributed radar systems to yield near-optimal solutions with significantly reduced computational requirements compared to traditional optimization methods. Our approach extends beyond simply applying existing DPS techniques by incorporating minimal spacing considerations for antenna placement directly into the DPS framework, while simultaneously reducing the downstream task model complexity. This represents a significant methodological contribution that adapts DPS specifically for the practical constraints and requirements of distributed radar array optimization.

Through this work, we seek to advance the state-of-the-art in sensor array design by bridging estimation and detection theory with modern artificial intelligence approaches, potentially enabling more capable and efficient sensing systems for various applications.

1.3 Literature review

In this section, an overview of radar networks for distributed radar systems is presented first. This is followed by a discussion of the current state of the art in sparse antenna array design. The literature review is structured into three main parts: the first part analyzes several classical sparse array layouts; the second and third parts compare conventional signal processing algorithms with machine learning approaches for array optimization.

1.3.1 Radar networks

In the literature, radar systems that utilize multiple separated sensors or transmitters are known as radar networks [3]. Radar networks, in general, refer to groups of cooperating radar units, which may include mono-static radars and multi-static radar systems. Unlike conventional automotive radar setups where each radar operates independently, these radar networks—with cooperating units such as two radar sensors—can measure cross paths in addition to the direct paths. This capability allows them to capture both mono-static responses (where the transmitter and receiver are the same unit) and bi-static responses (where the transmitter and receiver are different units) [3].

The coherency of a radar network is a critical factor to consider, encompassing spatial, temporal, frequency, and phase aspects [4]. Specifically, we are concerned with the issue of phase coherency between different sensors. In scenarios where there is no coherency or synchronization between sensors and only mono-static responses are measured, DoA estimation from individual sensors may not achieve the desired angular resolution due to limited aperture size [5] and ambiguities arising from the limitations of multilateration techniques [6]. To reduce these ambiguities, information from range measurements [7] and velocity evaluations [8] is utilized. In incoherent networks with synchronized sensors operating cooperatively—which constitute the distributed radar systems discussed earlier—these networks lack phase coherency and therefore do not provide coherent processing gain. However, by exploiting angular diversity, robustness is increased [9].

Phase coherent radar networks share the advantages of incoherent networks but offer additional coherent processing gain and larger apertures for DoA estimation [10]. The analysis and application of mono-static and bi-static responses from two-sensor networks are among the most common practices [11]. In distributed systems, the baseline—the distance between sensors—determines the total aperture of the radar network, which can lead to angular ambiguity problems. While DoA estimation remains unambiguous when antenna elements are spaced at $\lambda/2$ intervals, angular ambiguity problems arise when the large baseline creates sparse virtual antenna arrays. This occurs because the increased separation between sensors strengthens side-lobes that effectively act as grating lobes, complicating the interpretation of target locations [12].

1.3.2 Sparse antenna array design

The following sections examine sparse antenna array design approaches across three categories: classical sparse array layouts with established geometrical patterns, classical sparse array design methods that mathematically optimize element placement, and recent machine learning strategies that leverage artificial intelligence for array configuration.

1.3.2.1 Classical sparse array layouts

Before exploring research on conventional signal processing and machine learning algorithms for sparse antenna array design, it's valuable to examine classical sparse array layouts to establish a conceptual foundation.

Unlike Uniform Linear Arrays (ULAs), which feature uniform spacing between elements resulting in high redundancy, sparse arrays employ non-uniform element spacing to create the same aperture as a ULA with fewer elements. Higher resolution can be achieved by reducing redundant spacing between antennas while increasing the array's overall length. Minimum Redundancy Arrays (MRAs) represent a class of linear arrays specifically designed to minimize this redundancy [13]. MRAs position antenna elements on a uniform grid with strategically omitted elements at specific grid points.

This concept has been successfully extended to MIMO array configurations as well [14], which are more useful for practical implementation.

Beyond grid-limited MRAs, other sparse array types include Co-Prime arrays [15], which utilize two uniform subarrays with co-prime inter-element spacing. Building upon this approach, nested arrays and super-nested arrays were subsequently introduced [16], offering closed-form solutions for antenna positioning. These sparse array configurations effectively reduce the number of required antenna elements by eliminating redundant information while demonstrating improved DoA estimation performance, particularly when using subspace-based methods such as MUSIC estimation [17]. It should be emphasized that traditional and simple DoA estimation algorithms like matched filter remain applicable with these arrays, due to their excellent beampattern characteristics. Low-complexity algorithms are often preferable when they can achieve comparable performance, particularly in scenarios where only a single snapshot is available for processing.

A particularly significant advantage of these array structures is their ability to estimate more target DoAs than there are physical sensors in the array—a capability that has been effectively demonstrated using nested arrays [15]. This property, known as increased degrees of freedom, represents a substantial advancement in array processing technology.

1.3.2.2 Classical sparse array design methods

Having examined the classical sparse array configurations and their structural advantages, we now turn our attention to the algorithms that seek optimal sparse arrays under different scenarios.

Nature-inspired algorithms are quite popular for sparse array design. In [18], genetic algorithms for sparse array optimization enabled joint MIMO topology and DoA algorithm design but suffered from a complex cost function, low generalization, and inability to independently optimize transmitter and receiver positions. Simulated annealing has been applied to do the task in another work [19]. Their approach demonstrated practical value through validation with real hardware implementations. However, this method was computationally intensive, risked settling on local optima, and required difficult trade-off decisions. The complexity is the main challenge that these two methods need to deal with. Meanwhile, a method called particle swarm optimization which is similar to genetic algorithm but computationally less heavy has emerged [20].

Recently, convex optimization has emerged as an efficient tool in this topic. Convex optimization has proven effective in solving complex array design challenges across multiple applications. In [21], techniques were applied for maximally sparse arrays while accounting for mutual coupling effects, addressing a significant real-world constraint often simplified in theoretical models. Authors in [22] further advanced the field by applying convex optimization to multiple beam synthesis of passively cooled 5G planar arrays, addressing both radiation performance and thermal constraints simultaneously. More recently, [23] extended the convex optimization tool to high level sensor selection based on CRLB theory, which indicates valuable selection patterns for different types of CRLB. While these techniques excel at providing mathematically optimal solutions under various constraints, their primary limitation is the computational complexity that can increase significantly with array size. A significant recent advancement comes from [24] developing a novel approach to joint transmit and receive sensor selection by exploiting the properties of the virtual array's multiplicity vector. This approach substantially reduces computational complexity compared to conventional methods, particularly as the number of targets increases. Their numerical results show that the proposed "Multiplicity" algorithm maintains comparable estimation performance to direct alternating optimization while requiring significantly less computation time, with the advantage becoming more pronounced with larger numbers of targets. However, it is debatable whether it can be developed for non-co-located array optimization.

Parallel to these developments, compressive sensing has established itself as another prominent methodology for sparse array design, offering a mathematically elegant framework based on sparsity principles. In the domain of classical compressive sensing, [25] presented a pioneering framework for MIMO radar using spatial compressive sensing techniques. Their work offered a comprehensive mathematical foundation for random array geometries in MIMO radar, deriving bounds on the measurement matrix coherence and establishing the isotropy property. However, their approach faces limitations with computational complexity that increases significantly with array size and constraints, potentially limiting its applicability for real-time processing in high-dimensional scenarios. In parallel, [26] developed an entropy-based algorithm for sparse array design specifically optimized for Bayesian compressive sensing (BCS). Their method leverages the statistical information inherent to BCS, particularly the entropy of recovered estimation vectors, to intelligently place sensor elements for maximum information gain. Through experimental validation with corner reflectors and extended targets, they demonstrated that BCS-based sparse arrays could achieve superior detection probability and angular resolution with significantly fewer elements than conventional methods. Despite these advances, the approach suffers from computational implementation overhead and potential SNR reduction with fewer array elements, requiring further investigation for practical deployments. A comprehensive comparison of classical signal processing algorithms for sparse array design is presented in Table 1.1.

1.3.2.3 Learning-based sparse array design methods

With the explosion of artificial intelligence in recent years, machine learning strategies have also been applied to sparse array design. [27] introduces a deep learning approach for cognitive radar antenna selection, framing it as a multi-class classification problem. Their convolutional neural network (CNN) outperformed Support Vector Machines (SVM) in classification accuracy and improved DoA estimation by over random selections. In [28], they proposed a relative straightforward way to jointly optimize antenna positions and a DNN-based estimator, using backpropagation to minimize DoA error directly. However, this approach comes with high computational costs due to the numerous trainable parameters across multiple layers. They also suffer from limited interpretation, which raises additional concerns. In [29], the authors proposed Learn-to-Select (L2S), a scalable framework employing multiple Softmax networks with orthogonalization constraints. Unlike classification-based methods, L2S

Table 1.1: Comparison of Classical Algorithms for Sparse Array Design in Literature

Category	Ref.	Advantages	Limitations
Nature-Inspired Algorithms	[18]	Genetic algorithm optimization; Joint array topology and DoA design	Complex cost function; Low generalization; Cannot optimize Tx/Rx jointly
	[19]	Simulated annealing; Real hardware validation; Practical value demonstrated	Computationally intensive; Local optima risk; Difficult trade-offs
	[20]	Particle swarm optimization; Less computational burden than GA	Complexity still remains challenging
Convex Optimization	[21]	Maximally sparse design; Mutual coupling consideration; Real-world constraints	Complexity scales with array size and constraints
	[22]	Multiple beam synthesis; Thermal and radiation constraints	Computational complexity with constraints
	[23]	CRLB-based sensor selection; Pattern analysis for different CRLB types	Significant complexity increase with array size
	[24]	Joint Tx/Rx selection; Virtual array multiplicity; Reduced complexity	Limited to co-located arrays (debatable extension)
Compressive Sensing	[25]	Mathematical foundation; MIMO radar framework	High-dimensional complexity; Real-time processing limitations
	[26]	Entropy-based BCS; Superior detection/resolution; Experimental validation	Complexity scales with array size; SNR reduction

efficiently scales to large arrays and allows flexible optimization. Nevertheless, such machine learning methods typically demand extensive training data, a large number of parameters, and careful hyperparameter tuning to perform effectively under varying conditions. From a practical deployment perspective, adapting these methods to jointly optimize transmitter and receiver configurations remains challenging, limiting their applicability in real-world systems. A comprehensive comparison of machine learning algorithms for sparse array design is presented in Table 1.2.

1.4 Research novelty

Through the extensive research review outlined in the previous section, we found the main research gap for sparse array design: *How to achieve non-co-located joint transmitter-receiver array optimization for distributed radar systems, while maintaining good side-lobe level (SLL) control for practical implementation, especially when using artificial intelligence tools.* In this thesis, we propose a novel Joint Deep Probabilistic Subsampling with CRLB Integration (J-DPSC) approach that addresses this gap. Our method uniquely combines joint transmit and receive antennas optimization with multi-static mode capabilities, while maintaining effective SLL control.

The novelty of our approach lies in the simultaneous optimization of transmitter and receiver arrays in non-co-located configurations for distributed radar systems. We

Table 1.2: Comparison of Machine Learning Algorithms for Sparse Array Design in Literature

Category	Ref.	Advantages	Limitations
Learning-based Approaches	[27]	CNN for cognitive radar antenna selection; Improved DoA estimation over random selection	Requires extensive training data; Limited interpretation; Computational overhead
	[28]	Joint antenna position and DNN estimator optimization; Straightforward approach	High computational costs; Numerous trainable parameters; Limited interpretation; Challenging hyperparameter tuning
	[29]	Learn-to-Select (L2S) framework; Scalable to large arrays; Flexible optimization	Extensive training data requirements; Large parameter space; Careful hyperparameter tuning needed; Challenging joint Tx/Rx optimization

incorporate physical constraints and SLL control that ensure practical implementation, while leveraging machine learning techniques for antenna selection with low computational complexity. Our method features a well-founded cost function that incorporates Cramér-Rao Lower Bound integration for performance optimization within a flexible and scalable framework that generalizes across different radar configurations and scenarios.

Our J-DPSC method builds upon the foundation established by [2] in deep probabilistic subsampling, extending it specifically for the task-adaptive requirements of distributed radar systems. This represents a significant advancement in addressing the limitations of current sparse array design methodologies.

The core contributions of this work have been accepted for oral presentation as a **first-author** paper at the **European Radar Conference (EuRAD) 2025**, to be held in Utrecht, demonstrating the academic recognition and impact of our novel approach to distributed radar array optimization.

1.5 Thesis outline

In this chapter, we have introduced the research background, motivation, problem statement, and provided a comprehensive literature review on radar networks and sparse antenna array design, establishing the foundation for our work. The rest of this thesis is organized as follows: Chapter 2 presents the system model for distributed radar networks, detailing the configuration, field assumptions, and signal models that underpin our approach. Chapter 3 examines the Cramér-Rao Lower Bound for both single and dual targets, providing the theoretical foundation that guides our optimization strategy. Chapter 4 introduces our novel probabilistic sampling approach, developing the Deep Probabilistic Subsampling with CRLB (DPSC) and Joint-DPSC frameworks for individual antenna selection in various operational modes for the distributed radar system. Chapter 5 evaluates the performance of our proposed methods through beampattern comparison and extensive simulations, demonstrating improvements in ULA optimization and transmitter-receiver configurations for multi-sensor networks. Chapter 6 concludes the thesis with a summary of results, highlighting the contributions and suggesting directions for future research. Appendices provide supplementary material including implementation code and one related publication.

1.6 Conclusion

This introductory chapter has established the foundation for our research on sparse antenna array design for automotive radar systems. We identified the critical challenge in modern autonomous driving applications: achieving high angular resolution within strict physical and economic constraints. Our examination of the literature revealed significant developments in radar networks and sparse array configurations, yet highlighted persistent gaps in non-co-located joint transmitter-receiver optimization for distributed radar systems. The proposed Joint Deep Probabilistic Subsampling with CRLB Integration (J-DPSC) approach addresses these limitations by combining machine learning techniques with well-founded estimation theory. This novel methodology enables simultaneous optimization of transmitter and receiver arrays in non-co-located configurations while maintaining effective side-lobe level control for practical implementation. The approach offers reduced computational complexity compared to conventional methods for large antenna selection problems while maintaining performance standards necessary for automotive applications. The remainder of this thesis will develop the theoretical foundation, methodological framework, and empirical validation of our proposed approach, demonstrating its potential to advance automotive radar technology for next-generation autonomous driving systems.

System and Signal Model 2

This chapter establishes the foundational system and signal model for distributed radar networks, presenting a comprehensive framework that bridges theoretical concepts with practical applications. By detailing the geometrical relationships between radar units, signal propagation characteristics, and working modes (mono-static and bi-static), we illuminate the unique capabilities of distributed configurations with different sensor orientations. The mathematical formulation of the signal model, incorporating steering vectors and selection matrices, provides the analytical backbone for subsequent sparse array design. Our careful examination of virtual array formation—particularly the distinct advantages of left-right symmetric sensor configurations—reveals how strategic placement enhances aperture size and detection performance. This system model, with its clear assumptions and defined boundaries, prepares the foundation for our new optimization methods.

2.1 Distributed radar system

This section examines distributed radar system configurations, focusing on two-sensor setups with MIMO capabilities. We first present the fundamental geometrical model and mathematical relationships for DoA estimation, then explore near-field versus far-field operational assumptions. Finally, we analyze how sensor orientation affects virtual array formation in mono-static and bi-static modes, demonstrating the significant aperture advantages of mirror-configured sensors.

2.1.1 System configuration

We present a two-sensor radar system where the sensors are separated by a baseline distance B, serving as the fundamental configuration for this thesis. Within this distributed radar system, each radar sensor comprises N_{Tx} transmitters and N_{Rx} receivers, effectively forming a MIMO radar configuration. Within each compact sensor, the inter-element spacing between receivers is d_{Rx} , and the spacing between transmitters is d_{Tx}. According to MIMO channel theory [9], the virtual array will contain $N_{Tx}N_{Rx}$ virtual channels, which gives a larger aperture than the physical array. Typically, d_{Rx} and d_{Tx} are chosen in such a fashion that the resulting virtual antenna array has at least 2 virtual antenna elements with spacing $\lambda/2$ to ensure unambiguous direction finding and to prevent grating lobes.

The geometrical model of the distributed radar system which contains two radar units is illustrated in Figure 2.1. The two radar units T_1 and T_2 are separated by the baseline distance B, with the center of the distributed radar system considered to be at the origin.

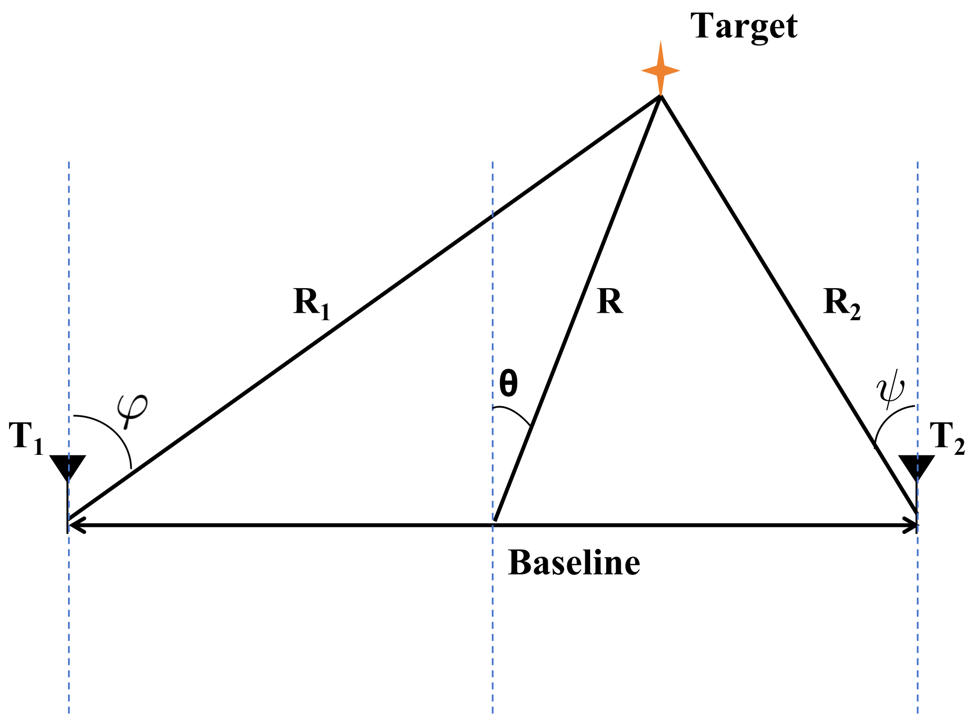

Figure 2.1: Distributed radar system geometry sketch

If a target is present at the range R from center of the system as shown in Figure 2.1, then from the perspective of radar sensor T_1 or T_2, the target is present at range R_1 or R_2. The corresponding DoD/DoA with respect to T_1 and T_2 are φ and ψ.

From the geometry of this system, we can acquire the relationship between the range and DoA of the target:

$$R_1 = \sqrt{R^2 + \frac{B^2}{4} + RB\sin\theta} \tag{2.1}$$

$$R_2 = \sqrt{R^2 + \frac{B^2}{4} - RB\sin\theta} \tag{2.2}$$

$$\sin\varphi = \frac{R\sin\theta + \frac{B}{2}}{R_1} \tag{2.3}$$

$$\sin\psi = \frac{R\sin\theta - \frac{B}{2}}{R_2} \tag{2.4}$$

2.1.2 Near-field and far-field assumption

It can be seen that the existence of baseline B introduces a large aperture for the distributed radar system and therefore it is necessary to check whether the far-field assumption holds. When targets are at moderate distances from a single sensor, it is assumed that the far-field assumption holds such that the reflected wave received from the target can be approximated with a planar wave. This distance is determined by the Fraunhofer distance [30]:

$$R_{FD} \approx \frac{2D^2}{\lambda} \tag{2.5}$$

where D is the aperture of the radar sensor and λ is the wavelength of the signal. If the distance of the target from the radar sensor is greater than the Fraunhofer distance, then the waves received can be approximated as planar waves and the target is said to be in the far field region. If the distance of the target is lesser than the Fraunhofer distance, then the target is said to be in the near field region of the radar, where the reflected wave is a spherical wave.

2.1.3 Specificity of distributed radar system

The distributed radar system allows us to capture both mono-static responses (where the transmitter and receiver are co-located) and bi-static responses (where the transmitter and receiver are separated). The virtual arrays for mono-static and bi-static responses can be generated using:

$$d^{Virtual} = d^{Tx} \oplus d^{Rx} = [d_1^{Tx} + d_1^{Rx}, d_2^{Tx} + d_1^{Rx}, \ldots, d_{N_{Tx}}^{Tx} + d_{N_{Rx}}^{Rx}] \tag{2.6}$$

where d^{Tx} and d^{Rx} represent the transmitter and receiver element positions in the sensor, $d^{Virtual}$ is the virtual array created by this rule. Based on this principle, the two generated bi-static responses create a virtual array at the center of the system. Consequently, the baseline does not affect the relative positions of the virtual antenna elements corresponding to the two bi-static responses. In contrast, for mono-static responses, the baseline cannot be disregarded; thus, it is essential to know the baseline precisely for coherent processing of all responses.

The orientation of the sensors T_1 and T_2-defined here as the relative positioning of each sensor's array elements-indeed influences the formation of bi-static responses. To facilitate understanding, we provide a visualization depicting a configuration with $d_{Rx} = \frac{\lambda}{2}$ and $d_{Tx} = N_{Rx} \cdot d_{Rx}$, where each sensor contains 4 transmitters and 4 receivers.

We first examine the case of translation, where both sensors are deployed with the same orientation. The baseline is set to 10 cm (approximately 26 wavelengths for 79 GHz carrier frequency) to help with clear visualization. The left-to-right (L2R) configuration indicates scenarios where T_1 is transmitting and T_2 is receiving. The same naming principle applies to the right-to-left (R2L) configuration. As shown in Figure 2.2, the bi-static responses from the T_1 and T_2 sensors overlap (the pink circles and dark crosses in the figure fully overlap each other), resulting from the symmetrical arrangement of the transmitting and receiving elements around the origin. This

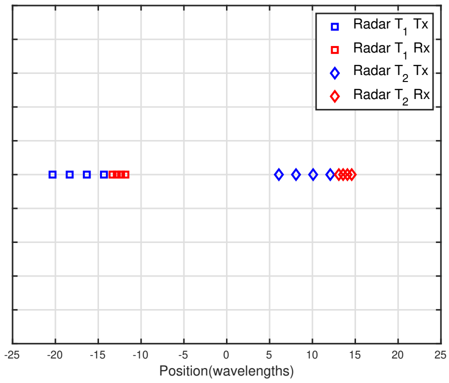

(a) Physical antenna array for distributed radar system

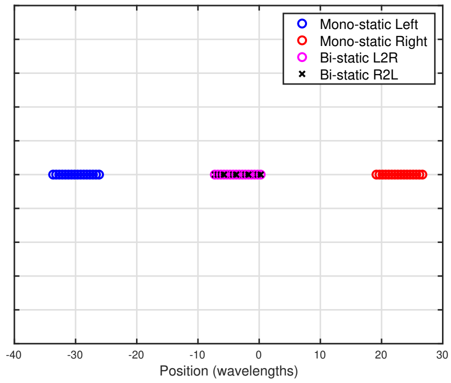

(b) Virtual antenna array for mono-static and bi-static responses

Figure 2.2: Physical and virtual array layout for two 4x4 MIMO radars T_1 and T_2 (identical configuration)

configuration effectively doubles the aperture to $2B$, comprising four smaller virtual apertures.

Next, we consider the mirror configuration, where T_1 and T_2 are identical but oriented differently. As illustrated in Figure 2.3, the two bi-static responses do not overlap at the center and instead form a larger aperture compared to the translation case. By analyzing the bi-static responses, we observe a gap between the two responses, which is determined by the spacing between the Tx and Rx elements within each sensor. Therefore, we can adjust this spacing to achieve a ULA centered around the center.

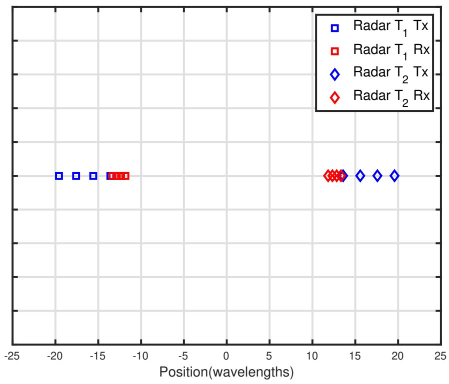

(a) Physical antenna array for distributed radar system

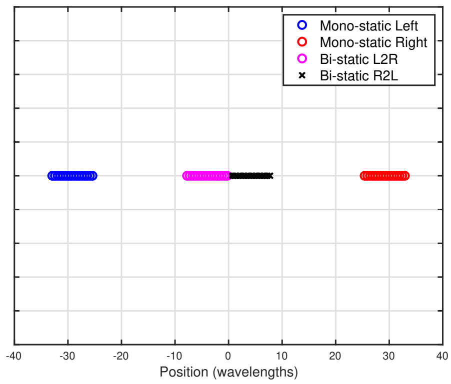

(b) Virtual antenna array for mono-static and bi-static responses

Figure 2.3: Physical and virtual array layout for two 4x4 MIMO radars T_1 and T_2 which have different orientation (mirror configuration)

From this visualization, we can realize the motivation for optimization on bi-static responses formed by differently oriented sensors, as they generate a large effective aperture around the center, providing significant performance advantages.

2.2 Signal model

We start with DoA estimation signal model for mono-static mode. The mono-static mode assumes that the received signals belong to reflected waves that originate from the same sensor. The spacing between the elements introduces differences in path lengths for the incoming waves. Under the far-field assumption, this delay in the arrival of the wavefront translates into a phase shift.

If we denote the received samples after range-Doppler processing from an array of M channels after MIMO decoding as $\boldsymbol{y}$, the signal model for the received samples corresponding to K targets can be expressed as follows:

$$\boldsymbol{y} = \boldsymbol{A}\boldsymbol{s} + \boldsymbol{n} \tag{2.7}$$

where $\boldsymbol{y} \in \mathbb{C}^{M\times 1}; \boldsymbol{s} \in \mathbb{C}^{K\times 1}; \boldsymbol{A} \in \mathbb{C}^{M\times K}; \boldsymbol{n} \in \mathbb{C}^{M\times 1}$. $\boldsymbol{s}$ is the impinging source vector, $\boldsymbol{n}$ is the noise vector, and $\boldsymbol{A}$ represents a collection of steering vectors for multiple targets. The steering vector $\boldsymbol{a}(\theta)$ represents the impinging signal from a target present at an angle θ from the array elements. Here we assume a ULA with d-spaced virtual antenna elements. The expression is given as

$$\boldsymbol{A} = [\boldsymbol{a}(\theta_1)\ \boldsymbol{a}(\theta_2)\ \ldots\ \boldsymbol{a}(\theta_K)] \tag{2.8}$$

$$\boldsymbol{a}(\theta) = [1, e^{\frac{j2\pi d \sin\theta}{\lambda}}, e^{\frac{j4\pi d \sin\theta}{\lambda}}, \ldots, e^{\frac{j(M-1)2\pi d \sin\theta}{\lambda}}]^T \tag{2.9}$$

Then we can expand the signal model to the two sensors system. Based on what we discussed in Section 2.1, under bi-static mode scenario, the Direction of Departure (DoD) and DoA of the wave differ due to the separation of the transmitter and receiver. Assuming T_1 in Figure 2.1 is the transmitting element and T_2 is the receiving element, the DoD is represented by φ, while the DoA is denoted by ψ. The steering matrix $\boldsymbol{A}$ consists of steering vectors that are the Kronecker product of the transmit (DoD) and receive (DoA) steering vectors, as shown in Equations (2.10) and (2.11). Specifically, $\boldsymbol{A}_{L2R}$ represents the steering matrix for the bi-static response when T_1 transmits and T_2 receives, while $\boldsymbol{A}_{R2L}$ represents the steering matrix for the bi-static response when T_2 transmits and T_1 receives.

$$\boldsymbol{A}_{L2R} = [\boldsymbol{a}_{T_1T_2}(\varphi_1 \otimes \psi_1), \boldsymbol{a}_{T_1T_2}(\varphi_2 \otimes \psi_2), \ldots, \boldsymbol{a}_{T_1T_2}(\varphi_K \otimes \psi_K)] \tag{2.10}$$

$$\boldsymbol{A}_{R2L} = [\boldsymbol{a}_{T_2T_1}(\psi_1 \otimes \varphi_1), \boldsymbol{a}_{T_2T_1}(\psi_2 \otimes \varphi_2), \ldots, \boldsymbol{a}_{T_2T_1}(\psi_K \otimes \varphi_K)] \tag{2.11}$$

For each steering vector $\boldsymbol{a}_{T_1T_2}(\varphi \otimes \psi)$ in the steering matrix, it can be calculated as the Kronecker product from the steering vector of transmitters and receivers. Let $Tx1$ and $Rx1$ be the transmitters and receivers in T_1 sensor, $Tx2$ and $Rx2$ be the transmitters and receivers in T_2 sensor. The construction of $\boldsymbol{a}_{T_1T_2}(\varphi \otimes \psi)$ is shown as

$$\boldsymbol{a}_{T_1T_2}(\varphi \otimes \psi) = \boldsymbol{a}_{Tx1}(\varphi) \otimes \boldsymbol{a}_{Rx2}(\psi) \tag{2.12}$$

$$\boldsymbol{a}_{Tx1}(\varphi) = [e^{\frac{j2\pi d_1^{Tx1}\sin\varphi}{\lambda}}, e^{\frac{j2\pi d_2^{Tx1}\sin\varphi}{\lambda}}, \cdots, e^{\frac{j2\pi d_{N_{Tx1}}^{Tx1}\sin\varphi}{\lambda}}]^T \tag{2.13}$$

$$\boldsymbol{a}_{Rx2}(\psi) = [e^{\frac{j2\pi d_1^{Rx2}\sin\psi}{\lambda}}, e^{\frac{j2\pi d_2^{Rx2}\sin\psi}{\lambda}}, \cdots, e^{\frac{j2\pi d_{N_{Rx2}}^{Rx2}\sin\psi}{\lambda}}]^T \tag{2.14}$$

In short, the Equation (2.13) and (2.14) can be expressed as

$$\boldsymbol{a}_{Tx1}(\varphi) = \exp(\frac{j2\pi \boldsymbol{d}^{\boldsymbol{Tx1}}\sin\varphi}{\lambda}) \tag{2.15}$$

$$\boldsymbol{a}_{Rx2}(\psi) = \exp(\frac{j2\pi \boldsymbol{d}^{\boldsymbol{Rx2}}\sin\psi}{\lambda}) \tag{2.16}$$

where $\boldsymbol{d}^{\boldsymbol{Tx1}}$ and $\boldsymbol{d}^{\boldsymbol{Rx2}}$ are the column vectors that contain transmitter element positions for T_1 and receiver element positions for T_2 respectively. Similarly, $\boldsymbol{a}_{T_2T_1}(\psi\otimes\varphi)$ can be constructed using the same procedure, but by exchanging the transmitters and receivers from T_1 and T_2. When the target is located in the far-field region, the DoD (φ) and DoA (ψ) are approximately equal, which enables the calculation of the virtual array as described in Equation 2.6.

Having established the foundational signal model that describes how electromagnetic waves interact with antenna arrays, we now shift our focus to a specialized application: we reformulate the sparse antenna design as an antenna selection problem. This reformulation maintains the core principles of our original model while introducing a sampling matrix where our machine learning strategy later comes into play. In order to pick L array elements from the full candidate set, a selection matrix $\boldsymbol{\Phi_P}$ can be constructed and multiplied with received signal $\boldsymbol{y}$. The structure and property of $\boldsymbol{\Phi_P}$ are as follows:

$$\boldsymbol{\Phi_P} \in \{0,1\}^{L\times M}, \quad \boldsymbol{\Phi_P}^T\boldsymbol{\Phi_P} = \boldsymbol{P} = \mathrm{diag}(\boldsymbol{p}), \quad \boldsymbol{\Phi_P}\boldsymbol{\Phi_P}^T = \boldsymbol{I}$$

and $\boldsymbol{p} = [p_1 \dots p_M]^T \in \{0,1\}^M$ is a binary selection vector where the L ones indicate the corresponding selected array elements, and zeros indicate the elements that are not selected.

In order to jointly learn selection vector for transmitters and receivers in this work, a structured subsampling is applied to the signal model. Data is compressed by specifying active transmitters L_T and receivers L_R from the full candidate transmitters M_T and receivers M_R, which is represented by selection matrices: $\boldsymbol{\Phi_T} \in \mathbb{R}^{L_T\times M_T}$, $\boldsymbol{\Phi_R} \in \mathbb{R}^{L_R\times M_R}$. These matrices follow a row-wise one-hot structure, and the selection matrix $\boldsymbol{\Phi_P}$ can be decomposed into $\boldsymbol{\Phi_P} = \boldsymbol{\Phi_T} \otimes \boldsymbol{\Phi_R}$. The $\otimes$ denotes the Kronecker product and the virtual antenna array in a MIMO is calculated as $L = L_T \times L_R$ and $M = M_T \times M_R$.

By applying this principle, the subsampled received signal $\boldsymbol{z}$ is expressed as:

$$\boldsymbol{z} = \boldsymbol{\Phi_P} * \boldsymbol{y} = (\boldsymbol{\Phi_T} \otimes \boldsymbol{\Phi_R}) * \boldsymbol{y} \tag{2.17}$$

2.3 System assumptions for scope of thesis

To narrow the focus on the core problem of sparse array design in distributed radar configurations, several assumptions are made. The following assumptions are applicable to this thesis:

- The mutual coupling and electromagnetic interaction are not considered for now into sparse array design.
- The targets are modeled as stationary point targets, each representing a single reflective source. This simplified model eliminates the need for specific dynamic DoA generation procedures in subsequent chapters.
- The analysis is restricted to the azimuth plane, focusing exclusively on one-dimensional sparse array design.

2.4 Conclusion

In this chapter, the system and signal model for the distributed radar system is introduced, providing the theoretical framework necessary for our sparse array design approach. We detailed the geometrical relationships between two radar units, examining how baseline distances and sensor orientations affect signal formulation. The critical distinction between near-field and far-field assumptions was addressed, clarifying the conditions under which our model operates. Our analysis of different sensor configurations indicated that mirror-oriented sensors offer advantages in bi-static operations, creating larger effective apertures compared to identically oriented sensors. This insight forms a key foundation for our optimization approach in later chapters. Then we formulated the mathematical signal model for the full array and incorporated selection matrices for the sparse array, which will serve as the foundation for our antenna selection methodology. The system assumptions presented provide clear boundaries for our research scope.

Cramér-Rao Lower Bound 3

This chapter provides a comprehensive analysis of the Cramér-Rao Lower Bound for single and dual targets DoA estimation under far field assumption. The CRLB gives a prediction of the estimation accuracy of the DoA in terms of a standard deviation. It defines the theoretical lower limit of estimation error achievable by any unbiased estimator. We begin by examining the CRLB for a single target, demonstrating that the dependency with SNR across different operational modes of the system, and providing proof for this statement. The CRLB for dual targets is also presented, along with an approximate CRLB. Additionally, we consider the impact of correlated signals, which significantly influences performance, particularly with closely spaced sources. This modeling is crucial for our analysis. With this thorough CRLB examination, we can effectively show the capability of an array without implementing DoA estimation algorithms, which is essential for sparse array design tasks. This will support the definition of a loss function moving forward to the proposed machine learning workflow in subsequent chapters.

3.1 CRLB for single target

To get affinity with CRLB, we derive the CRLB for a linear array [31]. Based on Equation (2.7) and source signal expression $s = \gamma e^{j\phi}$, the noisy version of the snapshot is equal to:

$$y_m = x_m + n_m, \quad \text{for} \quad m = 0, \dots, M-1 \tag{3.1}$$

where $x_m = s \cdot \exp(j2\pi \frac{d_m}{\lambda} \sin\theta)$. d_m for $m = 0, \dots, M-1$ indicates the positions of the M antenna elements and noise samples n_m are zero-mean complex Gaussian variables with variance σ_n^2 at each element. SNR is defined as $SNR = \frac{\gamma^2}{\sigma_n^2}$.

Then we can write the likelihood function of the noisy received signal as in [32]:

$$p(\boldsymbol{y}; \boldsymbol{\Omega}) = \exp[-\frac{1}{\sigma_n^2} \sum_{m=0}^{M-1} |y_m - x_m|^2] \cdot \frac{1}{(\pi\sigma_n^2)^M} \tag{3.2}$$

where the estimation vector $\boldsymbol{\Omega}$ contains signal amplitude γ, signal phase ϕ, and DoA θ. The Ω is explicitly expressed as:

$$\boldsymbol{\Omega} = [\Omega_1, \Omega_2, \Omega_3]^T = [\gamma, \phi, \theta]^T \tag{3.3}$$

The log-likelihood function is:

$$\ln p(\boldsymbol{y}; \boldsymbol{\Omega}) = -\ln(\pi\sigma_n^2)^M - \frac{1}{\sigma_n^2} \sum_{m=0}^{M-1} |y_m - x_m|^2 \tag{3.4}$$

The first derivative of the argument of the summations in the log-likelihood function with respect to Ω_i, produces:

$$\frac{\partial[\ln p(\boldsymbol{y};\boldsymbol{\Omega})]}{\partial\Omega_i} = \frac{\partial}{\partial\Omega_i}[-\frac{1}{\sigma_n^2}\sum_{m=0}^{M-1}|y_m - x_m|^2] \tag{3.5}$$

Using the chain rule for complex derivatives:

$$\begin{aligned}\frac{\partial\,|y_m - x_m|^2}{\partial\Omega_i} &= \frac{\partial[(y_m - x_m)(y_m - x_m)^*]}{\partial\Omega_i} \\ &= (y_m - x_m)^* \cdot \frac{\partial(y_m - x_m)}{\partial\Omega_i} + (y_m - x_m) \cdot \frac{\partial(y_m - x_m)^*}{\partial\Omega_i}\end{aligned} \tag{3.6}$$

where * symbol indicates the complex conjugate operation, and we can get:

$$\frac{\partial[\ln p(\boldsymbol{y};\boldsymbol{\Omega})]}{\partial\Omega_i} = \frac{2}{\sigma_n^2}\sum_{m=0}^{M-1}\mathrm{Re}[(y_m - x_m)^* \cdot \frac{\partial x_m}{\partial\Omega_i}] \tag{3.7}$$

and the second derivative with respect to Ω_j is:

$$\begin{aligned}\frac{\partial^2\,|y_m - x_m|^2}{\partial\Omega_i\partial\Omega_j} &= -\frac{\partial^2 x_m}{\partial\Omega_i\partial\Omega_j} \cdot (y_m - x_m)^* + \frac{\partial x_m}{\partial\Omega_i} \cdot \frac{\partial x_m^*}{\partial\Omega_j} \\ &\quad + \frac{\partial x_m}{\partial\Omega_j} \cdot \frac{\partial x_m^*}{\partial\Omega_i} - (y_m - x_m) \cdot \frac{\partial^2 x_m^*}{\partial\Omega_i\partial\Omega_j}\end{aligned} \tag{3.8}$$

Then we can get:

$$\begin{aligned}\frac{\partial^2 \ln p(\boldsymbol{y};\boldsymbol{\Omega})}{\partial\Omega_i\partial\Omega_j} &= \frac{1}{\sigma_n^2}\sum_{m=0}^{M-1}[\frac{\partial^2 x_m}{\partial\Omega_i\partial\Omega_j} \cdot (y_m - x_m)^* - \frac{\partial x_m}{\partial\Omega_i} \cdot \frac{\partial x_m^*}{\partial\Omega_j} \\ &\quad - \frac{\partial x_m}{\partial\Omega_j} \cdot \frac{\partial x_m^*}{\partial\Omega_i} + (y_m - x_m) \cdot \frac{\partial^2 x_m^*}{\partial\Omega_i\partial\Omega_j}]\end{aligned} \tag{3.9}$$

With the definition of Fisher information matrix $\boldsymbol{I}(\boldsymbol{\Omega})$ is:

$$\begin{aligned}[\boldsymbol{I}(\boldsymbol{\Omega})]_{i,j} &= -E[\frac{\partial^2 \ln p(\boldsymbol{y};\boldsymbol{\Omega})}{\partial\Omega_i\partial\Omega_j}] \\ &= \frac{1}{\sigma_n^2}\sum_{m=0}^{M-1}[\frac{\partial x_m}{\partial\Omega_i} \cdot \frac{\partial x_m^*}{\partial\Omega_j} + \frac{\partial x_m}{\partial\Omega_j} \cdot \frac{\partial x_m^*}{\partial\Omega_i}]\end{aligned} \tag{3.10}$$

After calculation and replacement, the Fisher information matrix can be expressed as:

$$
\begin{aligned}
\boldsymbol{I}(\boldsymbol{\Omega}) &= \frac{2}{\sigma_n^2}\sum_{m=0}^{M-1}\begin{bmatrix} 1 & 0 & 0 \\ 0 & \gamma^2 & \gamma^2\frac{2\pi d_m}{\lambda}\cos\theta \\ 0 & \gamma^2\frac{2\pi d_m}{\lambda}\cos\theta & \gamma^2\left(\frac{2\pi d_m}{\lambda}\right)^2\cos^2\theta \end{bmatrix} \\
&= \frac{2M}{\sigma_n^2}\begin{bmatrix} 1 & 0 & 0 \\ 0 & a & b \\ 0 & b & c \end{bmatrix}.
\end{aligned} \tag{3.11}
$$

where d_m represents the positions of m_{th} antenna element. In practice we will normalize the antenna position by $\lambda/2$ so we define $\tilde{d_m} = d_m/(\lambda/2)$ and

$$
\begin{aligned}
a &= \gamma^2 \\
b &= \frac{\gamma^2}{M}\frac{2\pi}{\lambda}\cos\theta\sum_{m=0}^{M-1} d_m = \pi\gamma^2 M_1\cos\theta \\
c &= \frac{\gamma^2}{M}(\frac{2\pi}{\lambda})^2\cos^2\theta\sum_{m=0}^{M-1} d_m^2 = \pi^2\gamma^2 M_2\cos^2\theta
\end{aligned} \tag{3.12}
$$

where M_1 and M_2 are the first and second moments of the normalized antenna positions:

$$
M_1 = \frac{1}{M}\sum_{m=0}^{M-1}\tilde{d_m} \tag{3.13}
$$

$$
M_2 = \frac{1}{M}\sum_{m=0}^{M-1}\tilde{d_m^2} \tag{3.14}
$$

The CRLB of DoA estimation can be acquired from:

$$
\begin{aligned}
\sigma_{\theta,CRLB}[\text{radian}] &= \sqrt{[\boldsymbol{I}^{-1}(\boldsymbol{\Omega})]_{3,3}} \\
&= \sqrt{\frac{\sigma_n^2}{2M}\frac{a}{ac-b^2}} \\
&= \frac{1}{\pi\cos\theta}\sqrt{\frac{1}{2SNR}\frac{1}{M(M_2-M_1^2)}}
\end{aligned} \tag{3.15}
$$

The unit of CRLB by default is radians here. The angle θ is with respect to the broadside.

The Equation (3.15) is used to compare the benchmark of different configurations. Figure 3.1 indicates that the estimation performance can be improved by jointly using multiple sensors. This improvement stems from two key contributions: first, the SNR scales with the number of antenna elements (resulting in M $\cdot$ SNR in the expression), and second, more elements increase the effective aperture of the array. With more sensors involved in the DoA estimation, the better the CRLB is, i.e. a lower value indicating better accuracy in DoA estimation. This is consistent with the intuition that finer angular resolution can be obtained with a large aperture. However, the single target-based CRLB only quantifies estimation accuracy, neglecting sidelobe levels, which means a lower CRLB does not necessarily guarantee improved DoA estimation performance in multi-target scenarios where both accuracy and sidelobe levels are important factors.

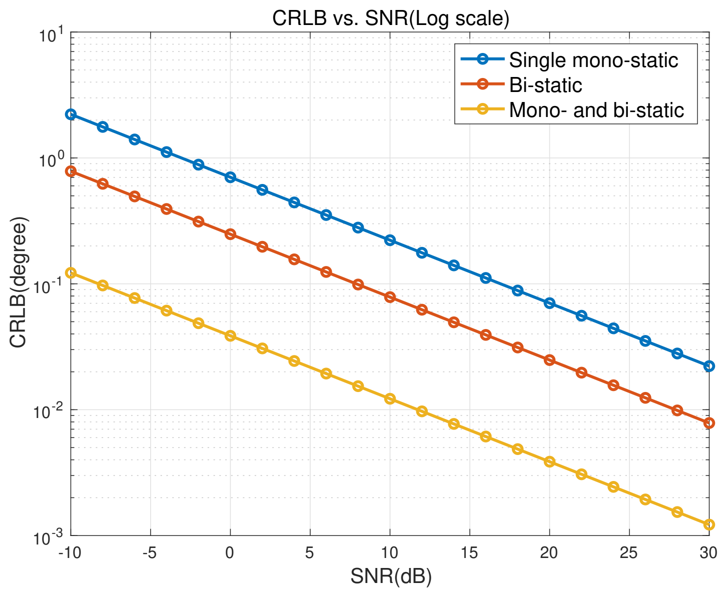

Figure 3.1: CRLB of DoA versus SNR of a single sensor together with bi-static and mono-static configuration of the radar system

Besides, we find the linear slope relationship for different configurations. The x-axis is SNR in dB scale and the y-axis is the logarithmic scale. This can be proved from Equation (3.15). The proof is shown like

$$\begin{aligned} \ln(\sigma_{\theta,CRLB}) &= -\frac{1}{2}\ln(2SNR) - \ln(\pi\cos\theta) - \frac{1}{2}\ln(M(M_2 - M_1^2)) \\ \ln(SNR) &= \frac{SNR_{dB}}{10\ln(10)} \\ \ln(\sigma_{\theta,CRLB}) &= -\frac{1}{20\ln(10)}\cdot SNR_{dB} - \frac{1}{2}\ln(2) - \ln(\pi\cos\theta) - \frac{1}{2}\ln(M(M_2 - M_1^2)) \end{aligned} \tag{3.16}$$

This can help us to predict the trend of curves for different responses.

3.2 CRLB for dual targets

In this section, we will discuss and analyze the expression of CRLB for uncorrelated signals and correlated signals. A ULA-32 is used to help evaluate dual-target CRLB.

3.2.1 Uncorrelated signals

The compact expression for the CRLB for uncorrelated source signals C_{CR} is given by [33]:

$$C_{CR}(\varphi)[\text{radian}^2] = \frac{\sigma_n^2}{2T}(\text{Re}\{[\boldsymbol{S}_f[(\boldsymbol{I} + \boldsymbol{A}^H\boldsymbol{A}\frac{\boldsymbol{S}_f}{\sigma_n^2})^{-1}(\boldsymbol{A}^H\boldsymbol{A}\frac{\boldsymbol{S}_f}{\sigma_n^2})]] \odot \boldsymbol{H}^T\})^{-1} \tag{3.17}$$

where $\varphi = \pi \sin\theta$ (θ is the angle with respect to the broadside), σ_n^2 is the noise power, T is the number of snapshots, $\boldsymbol{S}_f$ is the signal spectral matrix. Under the uncorrelated signals assumption, the signal spectral matrix is $\boldsymbol{S}_f = \text{diag}(\sigma_{s1}^2, \sigma_{s2}^2)$, where $\sigma_{s1}^2, \sigma_{s2}^2$ are the signal powers, respectively.

The matrix $\boldsymbol{H}$ in Equation (3.17) is given as:

$$\boldsymbol{H} = \boldsymbol{D}^H\boldsymbol{D} - \boldsymbol{D}^H\boldsymbol{A}(\boldsymbol{A}^H\boldsymbol{A})^{-1}(\boldsymbol{D}^H\boldsymbol{A})^H \tag{3.18}$$

where

$$\boldsymbol{D} = \left[\left.\frac{\partial \boldsymbol{a}(\varphi)}{\partial\varphi}\right|_{\varphi=\varphi_1} \quad \left.\frac{\partial \boldsymbol{a}(\varphi)}{\partial\varphi}\right|_{\varphi=\varphi_2}\right] \tag{3.19}$$

$$\boldsymbol{A} = [\boldsymbol{a}(\varphi_1) \quad \boldsymbol{a}(\varphi_2)] \tag{3.20}$$

and $\boldsymbol{a}(\varphi) = [e^{j\tilde{d_1}\varphi}, e^{j\tilde{d_2}\varphi}, \ldots, e^{j\tilde{d_M}\varphi}]^T$ with normalized antenna position.

One thing to note is that the φ transformation is used here to construct the steering vector and corresponding $\boldsymbol{H}$ matrix. Thus the CRLB as formulated in Equation 3.17 is based on the φ space. To facilitate comparison with the more familiar Root Mean Square Error on the θ space, we need to apply the transformation on CRLB again. The transformation is shown in the following equation as presented also in [33]

$$C_{CR}(\theta)[\text{radian}^2] = \boldsymbol{G_\theta}^{-1}C_{CR}(\varphi)\boldsymbol{G_\theta}^{-1} \tag{3.21}$$

Basically, the transformation matrix $\boldsymbol{G_\theta}$ is derived from the Jacobian matrix $\boldsymbol{J}$, which is defined by:

$$J_{ij} = \frac{d\varphi_i}{d\theta_j} = \pi\delta_{ij}\cos\theta_i \tag{3.22}$$

Then we know the relationship

$$\boldsymbol{G_\theta}^{-1} = \boldsymbol{J}^{-1} \tag{3.23}$$

and

$$\boldsymbol{G_\theta}^{-1} = \text{diag}\{\frac{1}{\pi\cos\theta_1}, \ldots, \frac{1}{\pi\cos\theta_K}\} \tag{3.24}$$

For a large value of $\boldsymbol{A}^H\boldsymbol{A}\frac{\boldsymbol{S}_f}{\sigma_n^2}$, the term in Equation (3.17) in the innermost square bracket approaches the identity matrix. This relationship can be proved by expanding this term in terms of its eigenvalues and eigenvectors [33]. Then, the expression for the approximated CRLB for uncorrelated sources C_{ACR} can be shown as follows:

$$C_{ACR}(\varphi)[\text{radian}^2] = \frac{\sigma_n^2}{2T}(\text{Re}\{\boldsymbol{H} \odot \boldsymbol{S}_f\})^{-1} \tag{3.25}$$

There are several conditions that need to be met to achieve this approximation.

- $\boldsymbol{S}_f$ is not close to singular.
- The targets are not too closely spaced.
- SNR is large

The next simulation proves the validity of the approximation. The first target is placed at 1° and the angular position of the second target is changing to simulate different source separation conditions. The Figure 3.2a and 3.2b illustrate the CRLB and its approximated version as a function of source separation. Notably, there is a small gap between the two calculations at close source separations when SNR is low. However, as the source separation and SNR increase, the gap gradually decreases. When SNR is high, two curves converge. This observation aligns with our initial assumptions. In scenarios characterized by high SNR or well-separated sources, the approximate CRLB can effectively substitute the original CRLB, thereby reducing computational complexity. This simplification is particularly valuable in practical applications. Besides, looking at Equation (3.25), the diagonal property of the signal spectral matrix indicates we can analyze the dynamic range by looking at both CRLBs in case signal power is different. This can be a powerful tool for dealing with complex situations such as two targets with different RCS.

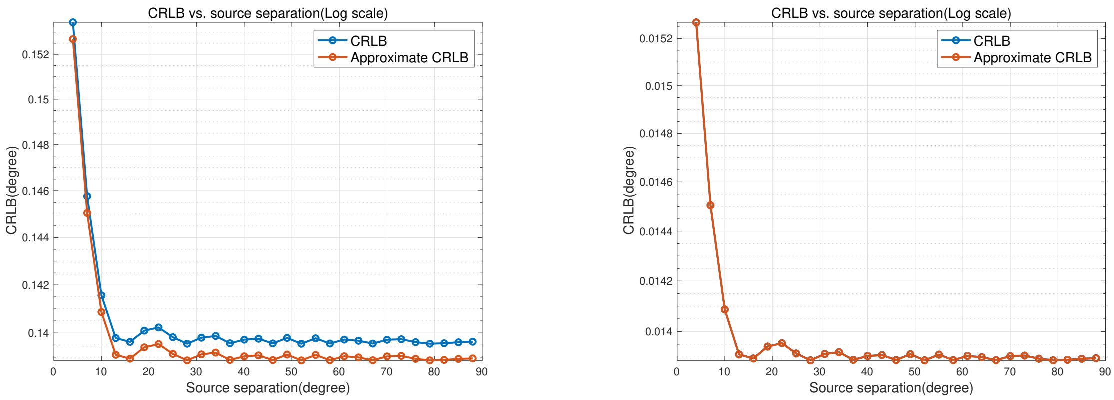

(a) (b)

Figure 3.2: CRLB of DoA and approximation CRLB with respect to source separation: (a) SNR = 5 dB (b) SNR = 25 dB

3.2.2 Correlated signals

The scenario becomes more complex when the signals are correlated. Fortunately, insightful contributions from [33] and [34] offer promising solutions to navigate these complexities.

First let us have a look at the fully correlated signals. For two signals, [33] obtained an analytic expression for the phase angle of the worst-case CRLB, where the expression "worst-case" is to be intended as having source signals that are fully correlated. Indeed, the intermediate mathematical manipulations encounter difficulties due to rank deficiency in the Fisher Information Matrix, necessitating a numerical approach. They show that the worst-case asymptotic conditional CRLB is given by fully correlated signals with

$$S_{12} = \sqrt{S_{11}S_{22}}\exp[j[\arg(\boldsymbol{H}_{12})]] \tag{3.26}$$

where $\boldsymbol{H}$ is defined in Equation (3.18) and S_{ij} indicates the element in the signal spectral matrix $\boldsymbol{S}_f$. For two correlated signals we actually introduce the phase relationship in the off-diagonal element, which helps consider the interaction between the two signals.

In addition to fully correlated (worst case) and fully uncorrelated (best case) signals, sometimes we would like to model the trends in between. The formula in [34] gives another view on the CRLB for more general cases as follows:

$$CRB(\varphi)[\text{radian}^2] = \frac{\sigma_n^2}{2T}\{\text{Re}[\boldsymbol{X}^H(t)\boldsymbol{D}^H[\boldsymbol{I} - \boldsymbol{A}(\boldsymbol{A}^H\boldsymbol{A})^{-1}\boldsymbol{A}^H]\boldsymbol{D}\boldsymbol{X}(t)]\}^{-1} \tag{3.27}$$

where $\boldsymbol{X}(t) = \text{diag}(x_1(t), x_2(t))$, and $x_1(t), x_2(t)$ are the signal expressions in the time domain. The matrices $\boldsymbol{D}$ and $\boldsymbol{A}$ are defined as in Equation (3.19) and (3.20). Specifically, in our case, in DoA estimation we only consider one snapshot thus the signal expression here is the one we get after range-Doppler processing. In that case, the signal matrix can contain the phase information of the signal, so we can model the phase relationship between two signals. When only a single snapshot is available, discussing *correlation* between two signals is not technically accurate. In this single-snapshot scenario, what we are actually observing is just the specific phase relationship between the two signals at that limited moment of time. Therefore, rather than using general terms like correlated or uncorrelated, it is more precise to refer to the "worst-case" and "best-case" to represent all types of scenarios. The "worst-case" occurs when the signals have a particular phase alignment that minimizes performance, while the "best-case" occurs when their phases are orthogonal to each other that maximizes performance.

The Figure 3.3 is to simulate different types of CRLB. Only one snapshot is considered here. The source separation is set to $4°$ and source locations $(7°, 3°)$, as the resolution limits of the array are taken into account. The Figure 3.3a, 3.3b, 3.3c and 3.3d indicate that at higher SNR, the two CRLB expressions match each other and correctly represent the DoA estimation performance of correlated and uncorrelated signals. The worst case exists at $0°$ and $180°$, the best case exists at $90°$ and $270°$ which means they are orthogonal to each other. With this tool we can find the limitation of a specific array for DoA estimation. This also holds for larger source separation.

A closer examination of the CRLB can provide valuable insights for DoA estimation. For instance, in Figure 3.3b, the worst-case CRLB is approximately $0.09°$. If we consider two Gaussian pulses located at the positions of the two targets, the 3σ rule indicates that most of the points will fall within that region. To prevent the overlap of the Gaussian pulses, the 3σ value should be less than the source separation of $4°$. Clearly, the calculation satisfies this criterion, implying that the array is able to distinguish between two fully coherent signals under these conditions.

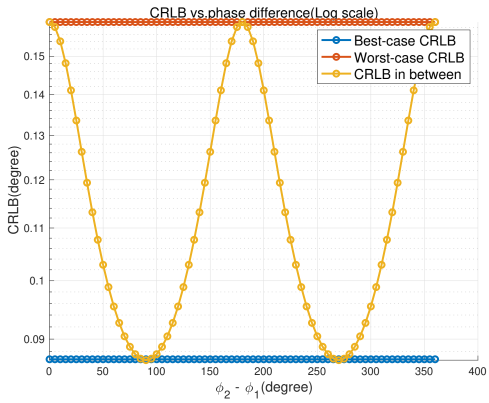

(a)

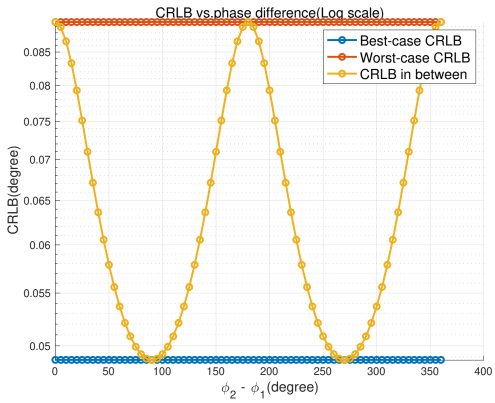

(b)

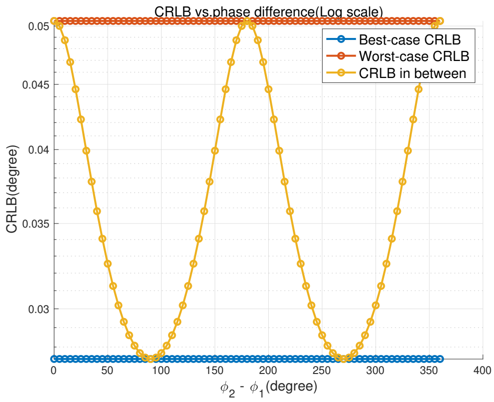

(c)

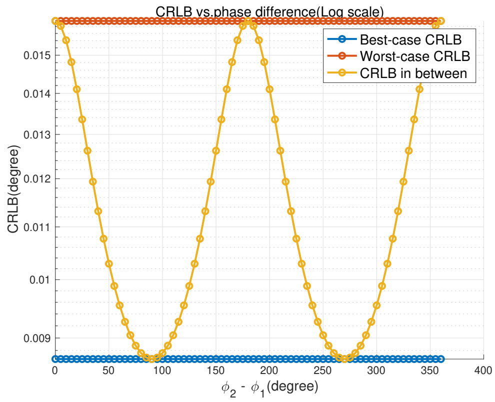

(d)

Figure 3.3: CRLB of DoA with respect to phase difference of two signals: (a) SNR = 10 dB, (b) SNR = 15 dB, (c) SNR = 20 dB, (d) SNR = 30 dB. The blue curve represents the CRLB of two signals with orthogonal phase relationship; the red curve represents the CRLB of two signals with the same phase; the yellow curve represents the results at any correlation condition.

3.3 Conclusion

This chapter provided a comprehensive theoretical analysis for the Cramér-Rao Lower Bound in both single and dual target scenarios. The CRLB derivation provides critical insights that directly inform our sparse array design methodology, as it will be regarded as the loss function in the machine learning workflow. By demonstrating the linear relationship between single CRLB and SNR on a logarithmic scale, we can accurately predict theoretical performance trends across different array configurations without extensive simulations. Our analysis of dual-target scenarios, particularly the validation of the approximate CRLB under high SNR conditions, offers significant computational advantages for practical implementation.

The examination of correlated signals through worst-case and best-case modeling provides a robust framework for evaluating array performance under different conditions. Specifically, by utilizing the formulation for correlated signals, we can predict performance across the entire phase difference between two targets. This capability enables precise assessment of array layout limitations under specific operational scenarios. The practical value of this CRLB derivation lies in its ability to serve as an objective optimization metric for sparse array design. Unlike traditional beampattern analysis, the CRLB directly quantifies estimation accuracy and targets interaction through deterministic calculation. This allows us to mathematically predict the resolution capabilities of different array configurations before DoA estimation and hardware implementation, enabling more efficient design iterations. As we progress to the probabilistic sampling approach in the next chapter, this CRLB framework will provide a robust theoretical basis for our machine learning optimization.

Furthermore, the dual-target CRLB analysis provides crucial insights into two fundamental radar performance indicators: angular separability and dynamic range in the angular domain. The CRLB formulation captures the best performance we can achieve for a specific source separation, directly quantifying performance limits as a function of array geometry and signal conditions. Similarly, the framework reveals dynamic range capabilities by characterizing how estimation accuracy changes when targets of varying strengths are present simultaneously. These insights are particularly valuable for radar system design, as both separability and dynamic range represent critical operational requirements.

Probabilistic Sampling Strategy 4

This chapter presents a comprehensive framework for optimizing radar systems through innovative selection strategies. By employing Deep Probabilistic Subsampling (DPS) with Cramér-Rao Lower Bound optimization, we aim to advance beyond traditional approaches to sparse array design. Specifically, the developed Joint-DPSC (J-DPSC) methodology addresses the challenges of joint transmitter-receiver optimization across mono-static and bi-static configurations, demonstrating how probabilistic selection can be effectively used into distributed radar systems. Our approach uniquely integrates antenna selection with practical implementation constraints through the Neighborhood Masking Mechanism, ensuring that theoretical optimizations remain physically realizable.

4.1 Deep probabilistic subsampling

As demonstrated in Chapter 2, sparse array design can be conceptualized as a selection problem where a subset of elements is chosen from a candidate pool of antenna array elements based on a given cost function. The Deep Probabilistic Subsampling strategy, originally developed in the ultrasound imaging domain, is introduced here to help with the antenna selection problem [2]. The DPS method effectively integrates subsampling in an end-to-end deep learning model, but learns a static pattern for all data points.

The selection matrix is formulated by considering each row as a sample drawn from a categorical distribution. Since neural networks struggle with discrete variables, a common solution is the Gumbel-Softmax reparameterization [35]. In this approach, an unnormalized log-probability vector $\boldsymbol{p}$ (logits) is transformed into a one-hot row vector $\boldsymbol{\phi}$, where each p_i represents the probability that ϕ_i is set to 1.

The Gumbel-max trick generates a mask matrix $\boldsymbol{A}$ by perturbing unnormalized logits $\phi_{l,m}$ with i.i.d. Gumbel noise $e_{l,m} \sim \text{Gumbel}(0,1)$. Row l of the mask matrix is given as:

$$A_{l,:} = \text{one-hot}_M \left(\arg\max_m \{w_{l-1,m} + \phi_{l,m} + e_{l,m}\} \right) \tag{4.1}$$

where $w_{l-1,m} \in \{-\infty, 0\}$ ensures sampling without replacement, by masking previously selected indices.

For backpropagation, the sampling process is relaxed using the Gumbel-softmax trick as:

$$\nabla_{\phi_l} A_{l,:} = \nabla_{\phi_l} \mathbb{E}_{e_l} \left[\text{softmax}_\tau \{w_{l-1,m} + \phi_{l,m} + e_{l,m}\} \right] \tag{4.2}$$

where $\tau > 0$ is a temperature parameter controlling the smoothness of the sampling distribution. As $\tau \to 0$, the Softmax converges to the one-hot argmax. Although this introduces biased gradients, in practice it has been shown to work effectively [2] when τ is kept fixed during training.

A high-level flowchart of the DPS layer is illustrated in Figure 4.1 to enhance understanding. The figure depicts the sampling-without-replacement process through repeated application of the perturbed logits vector across L rows, followed by the incorporation of a masking matrix with the same dimension. The Softmax function drives the sampling process and approximates the selection matrix we want.

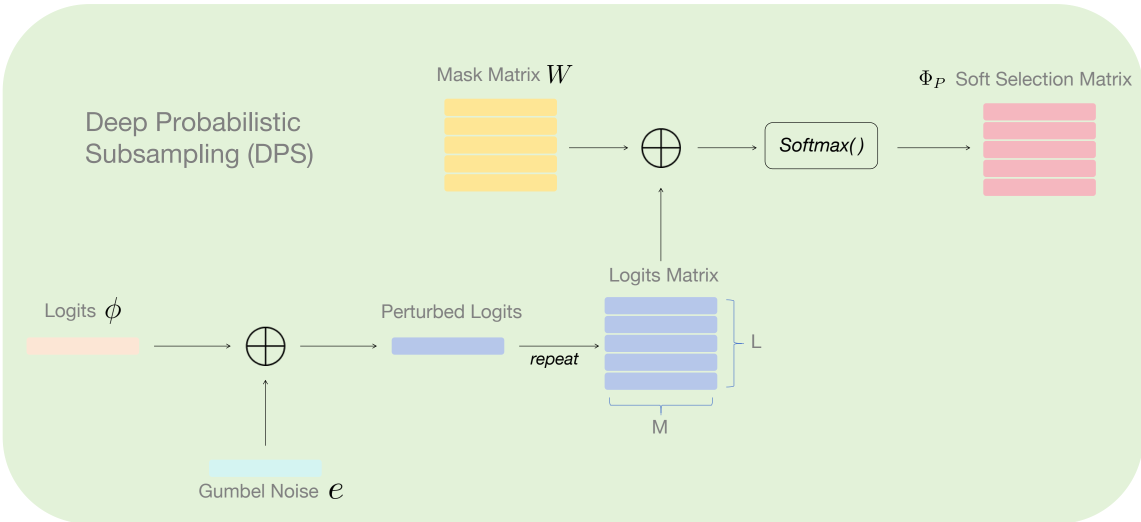

Figure 4.1: Flowchart of DPS algorithm

This final trainable subsampling pattern of DPS will approximate the selection matrix $\boldsymbol{\Phi_P}$ for Equation (2.17). In the original work [2], they subsequently aim to decode the subsampled data $\boldsymbol{z}$ into $\boldsymbol{f}$, some function of the original signal vector $\boldsymbol{y}$ in which they are interested. To this end, a differentiable function approximator $g_\theta(\cdot)$ is used to get the approximation of $\boldsymbol{f}$:

$$\hat{\boldsymbol{f}} = g_\theta(\boldsymbol{z}) \tag{4.3}$$

In DPS technique the subsampling and the downstream task model $g_\theta(\cdot)$ are jointly learned. The function $g_\theta(\cdot)$ is most likely a neural network in this case. The proposed DPS enables joint learning of an adequate subsampling pattern for $\boldsymbol{y}$ and recovery of $\boldsymbol{f}$ through $g_\theta(\cdot)$ by backpropagation.

Returning to the radar signal processing domain, the subsampling component effectively addresses sparse array design challenges, while downstream tasks can involve either signal reconstruction or DoA estimation—both fundamental in radar applications. While joint optimization of sparse array configuration and DoA estimation is certainly feasible, this thesis narrows its scope to focus exclusively on sparse array design. To further reduce computational complexity, we replace the complete task model with a theoretically rigorous loss function based on the CRLB. A comprehensive analysis of this loss function and its implications will be presented in the following section.

In order to facilitate the antenna element selection and fit in the following defined loss function, a 1-D logits is generated from DPS layer. That is to say, the soft subsampling will be used for the following computations.

4.2 Loss function

This section develops our loss function choice for sparse array optimization based on machine learning. We first analyze CRLB variants, demonstrating through beampattern comparisons that worst-case dual-target CRLB provides optimal balance between angular resolution and sidelobe control. We then present a mathematical relaxation of the CRLB that maintains theoretical integrity while enabling gradient-based optimization. Finally, we incorporate an entropy-based penalty term that promotes one-hot distributions, resulting in a comprehensive loss function that effectively guides our probabilistic sampling framework.

4.2.1 CRLB's sensitivity

Selecting an appropriate loss function is vital for achieving the core objectives of sparse array design. When developing such arrays for practical radar applications, choosing the most suitable variant of the CRLB becomes crucial, as different formulations provide distinct insights into system performance characteristics. This section examines why the worst-case CRLB emerges as the optimal choice among all available formulations for our sparse array design problem, offering a balanced consideration of both angular resolution capabilities and sidelobe level performance.

Based on the CRLB analysis presented in Chapter 3, we have examined both single-target CRLB and dual-target CRLB (in both best-case and worst-case scenarios). It becomes evident that the single-target formulation serves as an inadequate indicator when simultaneous consideration of angular resolution and SLL is required, as its derivation contains no provisions for SLL assessment or interactions with secondary targets.

The dual-target CRLB formulation inherently accounts for signal correlation, where varying the mutual phase difference between target complex amplitudes for the single snapshot realization allows the bound to range from worst-case to best-case outcomes, as reflected in the corresponding changes to the signal spectral matrix structure. The best-case formulation features a diagonal matrix, while the worst-case incorporates additional terms in the off-diagonal positions. According to the theoretical significance of these off-diagonal components, the worst-case CRLB emerges as a particularly powerful indicator for our design objectives. The beampattern analysis that follows will provide intuitive evidence supporting this theoretical advantage, demonstrating how the worst-case CRLB effectively captures both angular resolution capabilities and sidelobe performance.

To ensure clarity in our comparative analysis, we first establish the simulation setup. All beampattern results are generated using a virtual MIMO array configuration formed by current implementation antenna layouts from NXP current practices: Tx - [0, 3, 6, 9] and Rx - [0, 4, 8, 12] (with antenna positions normalized by $\lambda/2$). For visualization clarity, we limit our analysis to a single snapshot when generating the beampattern, employing the matched filter method and noise-free condition for plot generation.

The phase relationship between targets is defined as follows: *worst-case* refers to signals with identical phases, while *best-case* denotes signals with orthogonal phase relationships. In Figures 4.2a and 4.2b, targets are positioned at angles ($-1.5°$, $1.5°$), representing closely spaced targets. Under worst-case phase relations and this close source separation setting, the lobes merge completely, making it impossible to distinguish between the two targets. Conversely, with best-case phase relations, although the targets remain distinguishable, their estimated positions exhibit significant deviation from ground truth due to lobe interactions. These results indicate that worst-case CRLB effectively accounts for the interaction between main lobes and sidelobes, providing an opportunity to suppress SLL during array design.

For Figures 4.2c and 4.2d, targets are placed at ($-5°$, $5°$) to investigate how phase relationships affect performance with wider angular separation between targets. In both scenarios, targets are successfully distinguished. However, closer examination reveals subtle but important differences: the estimated angles for best-case phase relation are ($-5.162°$, $5.162°$), while for worst-case phase relation they are ($-5.264°$, $5.264°$). This provides another perspective on worst-case CRLB—it consistently reveals side effects from signal correlation (phase relation for a single snapshot), further supporting our decision to adopt it for sparse array design.

4.2.2 CRLB relaxation

As established in Section 4.1, ensuring differentiability in the downstream task model is essential for enabling backpropagation throughout our framework using machine learning tools. This section introduces a mathematical relaxation of the CRLB that preserves its theoretical strengths while achieving the necessary differentiability.

By integrating the selection matrix $\mathbf{\Phi}_{\boldsymbol{P}}$ in Equation (2.7) and worst-case CRLB formula (3.17), (3.26), the worst-case dual-targets CRLB is given as:

$$C_{CR}(\boldsymbol{\varphi}, \boldsymbol{p}) = \frac{\sigma_n^2}{2T}(\mathrm{Re}\{\boldsymbol{H}(\boldsymbol{p}) \odot \boldsymbol{S}_f\})^{-1} \tag{4.4}$$

$$\boldsymbol{H}(\boldsymbol{p}) = \boldsymbol{D}^H\boldsymbol{P}\boldsymbol{D} - \boldsymbol{D}^H\boldsymbol{P}\boldsymbol{A}(\boldsymbol{A}^H\boldsymbol{P}\boldsymbol{A})^{-1}(\boldsymbol{D}^H\boldsymbol{P}\boldsymbol{A})^H \tag{4.5}$$

Evidently, the final formula contains no trace of matrix $\mathbf{\Phi}_{\boldsymbol{P}}$, but instead features the diagonal matrix $\boldsymbol{P}$. This transformation elegantly demonstrates our approach of utilizing selection vector logits from the DPS layer to advance the workflow.

To obtain a scalar objective for the loss function, we propose to use the worst-performing target as:

$$\mathcal{L}_{CRB} = \max_{\boldsymbol{\varphi}} \ \mathrm{trace}(C_{CR}(\boldsymbol{\varphi}, \boldsymbol{p})) \tag{4.6}$$

Moreover, to reduce complexity and satisfy the assumptions of the single snapshot signal model, T in Equation (4.4) is set to 1 in practical simulations.

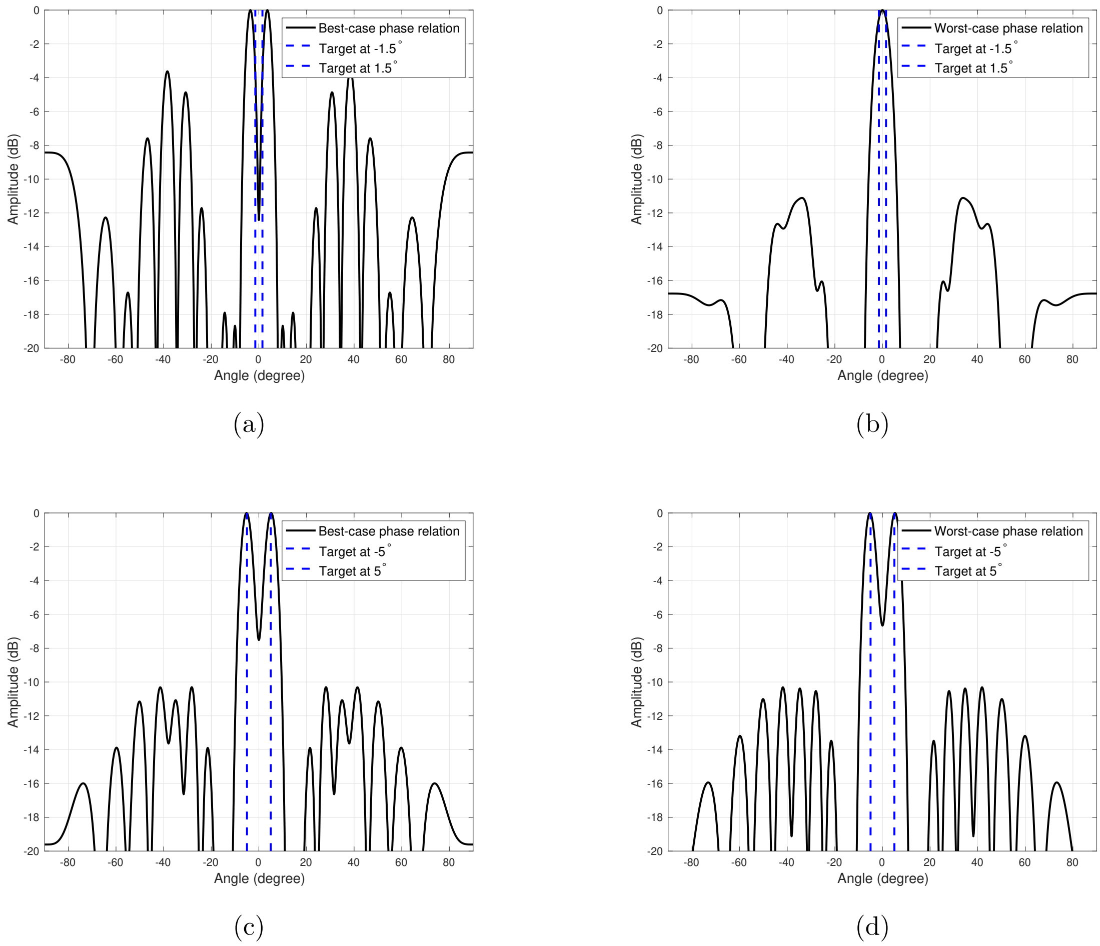

Figure 4.2: Beampattern comparison under different phase relationships and target separations: (a) Best-case phase relation (orthogonal phases) with targets at $(-1.5°, 1.5°)$; (b) Worst-case phase relation (identical phases) with targets at $(-1.5°, 1.5°)$; (c) Best-case phase relation with targets at $(-5°, 5°)$; (d) Worst-case phase relation with targets at $(-5°, 5°)$. The figures demonstrate how phase relationships affect target distinguishability and position estimation accuracy

4.2.3 Entropy-based penalty term

Another part of the total loss function is called the entropy-based penalty term $\mathcal{L}_s$. This term encourages training towards one-hot distributions [2]. Here, $\mathcal{L}_s$ is defined as:

$$\mathcal{L}_s = -\sum_{l=1}^{L}\sum_{m=1}^{M} \pi_{l,m} \log \pi_{l,m} \tag{4.7}$$

where $\pi_{l,m}$ represents the probability of sampling the m_{th} entry in $\boldsymbol{y}$ at the l_{th} measurement $\boldsymbol{z}_l$. $\pi_{l,m}$ is defined as the normalized logits from $\phi_{l,m}$:

$$\pi_{l,m} = \frac{\exp \phi_{l,m}}{\sum_{i=1}^{M} \exp \phi_{l,i}} \tag{4.8}$$

To conclude, the combined loss function is formulated as:

$$\mathcal{L} = \mu\mathcal{L}_s + \lambda'\mathcal{L}_{CRB} \tag{4.9}$$

where λ' and μ are penalty multipliers that control the relative importance of the CRLB loss and the entropy penalty term.

4.3 Neighborhood masking mechanism

In order to address physical implementation constraints in antenna design, we introduce the Neighborhood Masking Mechanism (NMM) to the DPS layer. This mechanism can account for practical considerations such as antenna size, mutual coupling effects, and feed line layout requirements. The NMM employs a neighbor radius parameter r that enables precise control over the minimum spacing between antenna elements. By implementing this approach, we ensure that the theoretical optimization results can be effectively translated into physically realizable antenna arrays while maintaining performance objectives.

This additional neighbor exclusion mask $N_{l,m}$ is defined as:

$$N_{l,m} = \begin{cases} -\infty, & \text{if } |m - m'| \leq r \text{ for previously selected } m' \\ 0, & \text{otherwise} \end{cases} \tag{4.10}$$

The formula (4.1) of the DPS can be reformulated as follows to include the NMM:

$$A_{l,:} = \text{one-hot}_M \left(\arg\max_m \{N_{l,m} + \phi_{l,m} + e_{l,m}\} \right) \tag{4.11}$$

The key modification in Equation (4.11) compared to the original DPS formulation (4.1) is the replacement of the penalty term $w_{l-1,m}$ with the neighborhood masking term $N_{l,m}$. This substitution fundamentally changes the selection mechanism by incorporating spatial constraints directly into the sampling process. In the original DPS approach, the penalty $w_{l-1,m} \in \{-\infty, 0\}$ simply prevents reselection of previously chosen indices. However, our neighborhood masking mechanism $N_{l,m}$ extends this concept by also preventing the selection of any antenna elements that fall within the specified radius r of previously selected elements. This ensures that the minimum spacing constraint is enforced throughout the optimization process, making the theoretical results directly applicable to practical antenna array implementations where physical spacing requirements must be satisfied.

4.4 Deep probabilistic subsampling with CRLB (DPSC)

After introducing the subsampling methodology and defining our algorithm's loss function, we are now prepared to present the complete framework. Deep probabilistic subsampling with CRLB (DPSC) efficiently optimizes virtual MIMO arrays based on the established loss function, providing a novel approach to sparse array design.

The framework illustrated in Figure 4.3 presents a comprehensive approach for linear sparse array design. In this optimization process, the initial logits for the full candidate set are represented by $\boldsymbol{\phi_{ULA}}$. Then, after going through the DPS layer shown in Figure 4.1, the trained logits $\tilde{\boldsymbol{\phi}}_{\boldsymbol{ULA}}$ are fed into the loss function calculation with the necessary dataset made of couples of DoAs and SNR values $(DoAs, SNRs)$. The entire system operates through forward passes (blue arrows) for evaluation, and backpropagation (green dashed arrows) for gradient-based optimization. This unified framework efficiently proceeds with ULA sparse array design (no distinction between transmitters and receivers). The output of this procedure is an optimized selection vector that indicates which antenna elements from the full ULA should be selected to achieve the desired sparse array configuration.

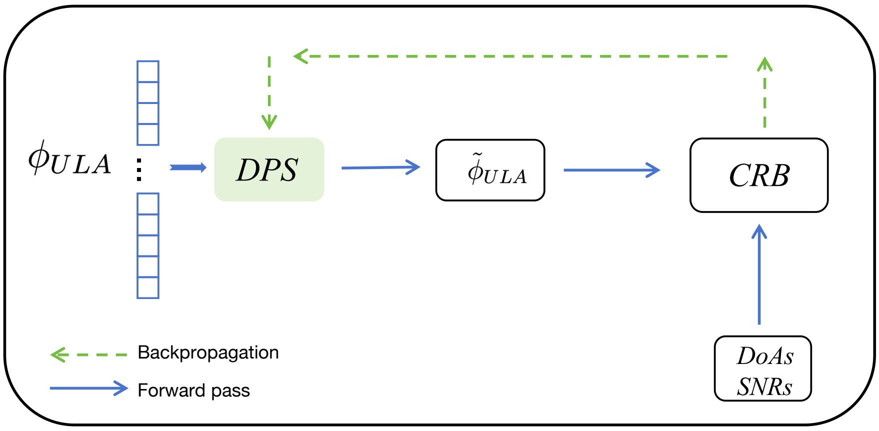

Figure 4.3: Framework of proposed DPSC on ULA sparse array design

4.5 Joint deep probabilistic subsampling with CRLB (J-DPSC)

Building upon the DPSC framework presented in the previous section, we now extend our approach to develop Joint Deep Probabilistic Subsampling with CRLB (J-DPSC) for joint transmitters and receivers optimization, which is crucial for distributed radar systems where multiple working modes are available. By integrating the strengths of our probabilistic subsampling technique with CRLB analysis in a joint optimization framework, J-DPSC enables the design of sparse array structures capable of efficient performance in varying working modes. The following subsections explore the application of J-DPSC to mono-static mode, bi-static mode, and their joint optimization.

4.5.1 J-DPSC for mono-static mode

The operational procedure of proposed J-DPSC for mono-static mode is illustrated in Algorithm 1.

Two parallel networks are trained simultaneously to jointly optimize transmitter and receiver arrays. The logits vectors are initialized following a normal distribution with a variance of $\frac{1}{CR_T \times CR_R}$, where CR_T and CR_R (compression ratio) represent the ratio of selected transmitter and receiver elements to the full array elements, respectively. As training progresses, the output of each DPS layer—normalized logits—gradually approximates the binary selection vector. Once the unified soft selection vector is obtained, it is paired with the corresponding data and used to compute the loss.

Algorithm 1 Proposed J-DPSC

Input: Training dataset: $(DoAs, SNRs)$; parameters of selection candidates and subsampling: M_T, M_R, L_T, L_R; number of iterations: N_{iter}
Initialization:
- Logits vectors: $\boldsymbol{\phi_T}, \boldsymbol{\phi_R} \sim \mathcal{N}(0, \frac{1}{CR_T \times CR_R})$
- Temperature: $\tau = 0.2$
- Learning rate: $lr = 5e-2$

for $i = 1$ to N_{iter} **do**
    Draw a random subset of training dataset
    In parallel compute soft selection vectors:
    - $\tilde{\boldsymbol{\phi}}_{\boldsymbol{T}} = \text{softmax}(\boldsymbol{\phi_T}, w, e, \tau)$
    - $\tilde{\boldsymbol{\phi}}_{\boldsymbol{R}} = \text{softmax}(\boldsymbol{\phi_R}, w, e, \tau)$
    Unified soft selection vector: $\tilde{\boldsymbol{\phi}}_{\boldsymbol{P}} = \tilde{\boldsymbol{\phi}}_{\boldsymbol{T}} \otimes \tilde{\boldsymbol{\phi}}_{\boldsymbol{R}}$
    Compute the loss: $\mathcal{L} = \mu \mathcal{L}_s + \lambda' \mathcal{L}_{CRB}$
    Update learning rate: $lr_{new} = 0.96 * lr$
    Use Adam optimizer [36] to update logits by minimizing $\mathcal{L}$
end for
Output: Trained soft selection vectors $\tilde{\boldsymbol{\phi}}_{\boldsymbol{T}}, \tilde{\boldsymbol{\phi}}_{\boldsymbol{R}}$.

Figure 4.4 illustrates the J-DPSC framework for joint transmitter and receiver optimization in mono-static mode. Unlike the previous ULA sparse array design shown in Figure 4.3, this framework introduces separate optimization paths for transmitters and receivers. The initial logits for transmitters ($\boldsymbol{\phi_{Tx}}$) and receivers ($\boldsymbol{\phi_{Rx}}$) are processed through independent DPS layers, resulting in trained logits. These trained logits are then combined through a Kronecker product to form the virtual array pattern ($\tilde{\boldsymbol{\phi}}_{\boldsymbol{P}}$), which will be used for CRLB calculation. After the training process, the final output of the procedure consists of the optimized selection vectors for transmitters and receivers, respectively.

4.5.2 J-DPSC for bi-static mode

Distributed radar networks can sense their environment using mono-static from different perspective. When the radar sensors are synchronized, they can also profit from multi-static responses, i.e. responses from which the received reflections are originating from radar waveforms that are sent by another radar sensor, as indicated in Section 2.1. This feature enables the network to capture bi-static responses, where the transmitter and receiver belong to different sensors, provided that the synchronization requirements are met.

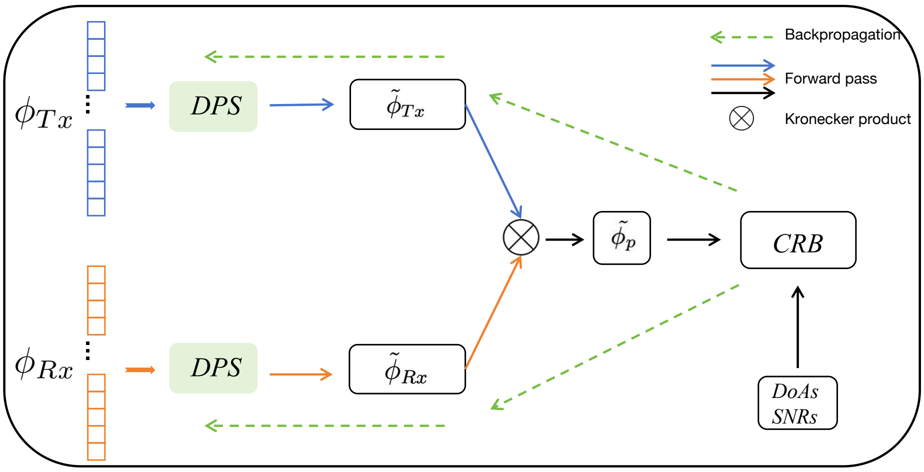

Figure 4.4: Framework of proposed J-DPSC on joint transmitters and receivers optimization in mono-static mode

In the setup, we choose to have two sensors that have mirror symmetry with reference to their antenna arrays since two bi-static responses will result in a larger virtual array around the center, as indicated in Section 2.1.3. As a result, only two parallel DPS layers are required to enable bi-static mode selection. The trained soft selection vector (shown in the dotted frame in Figure 4.5) indicates that a single trained logits vector can represent selections for transmitters or receivers at different locations. After applying the Kronecker product, the unified soft selection vector is concatenated with its flipped version to represent soft selection across all bi-static responses (note that the two bi-static virtual arrays are flipped versions of each other due to the symmetrical placement of the sensors). The subsequent forward pass and backpropagation proceed as outlined in Algorithm 1, ensuring optimal sensor selection through end-to-end differentiable learning. The final output of the procedure consists of the optimized selection vectors for transmitters and receivers, respectively, completing the optimization process for both sensor.

The flip operation is needed by our initial configuration of candidate transmitters and receivers, which are indexed with the same starting point rather than by their physical locations. Since we are focusing on only two bi-static responses while aiming to reduce computational complexity, the flip operation becomes essential for proper pairing. This approach allows us to efficiently map corresponding transmitter-receiver pairs without requiring explicit baseline information, thereby maintaining algorithmic efficiency while preserving the integrity of our bi-static processing model.

4.5.3 J-DPSC for joint mono-static and bi-static mode

Having established the optimization frameworks for both mono-static and bi-static modes individually, their joint optimization emerges as a natural and straightforward extension. The J-DPSC approach unifies these modes within a single framework, capitalizing on their complementary strengths while maintaining mathematical

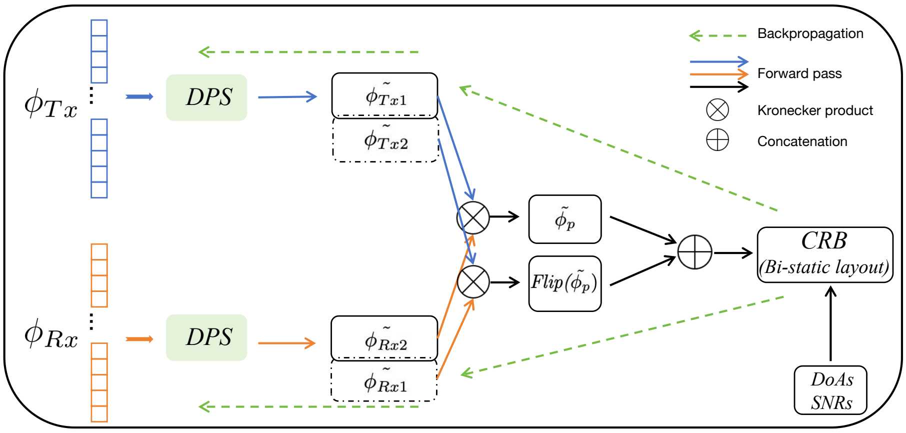

Figure 4.5: Framework of proposed J-DPSC on joint transmitters and receivers optimization in bi-static mode

simplicity.

For joint mono-static and bi-static mode optimization, baseline information plays a crucial role in our framework. The initialization of candidate transmitters and receivers leverages their physical locations rather than simplified indexing. Each transmitter-receiver pair generates a specific selection vector corresponding to its unique response pattern. These selection vectors are then concatenated and forwarded to the loss function, completing the optimization workflow as illustrated in Figure 4.6.

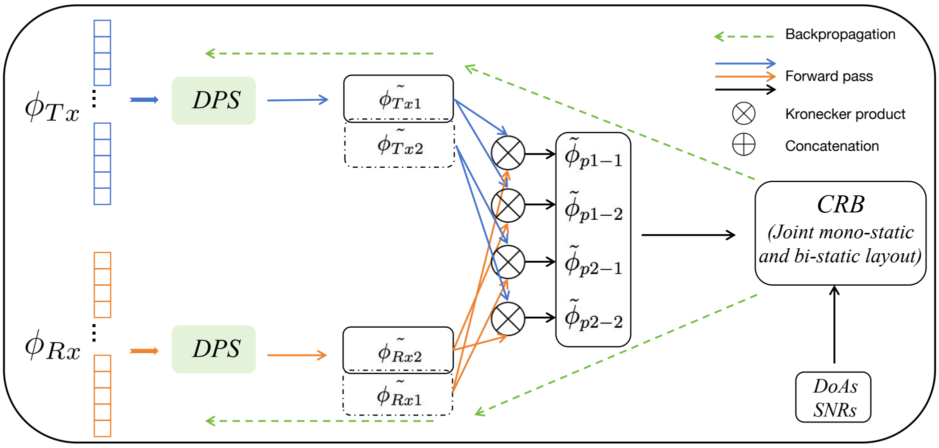

Figure 4.6: Framework of proposed J-DPSC on joint transmitters and receivers optimization in joint mono-static and bi-static mode

It should be stressed that bi-static operation inherently requires phase coherency and synchronization for the distributed radar system to be met. The joint mono-static and bi-static mode operation introduces additional requirements for accurate mounting and positioning of the sensors on top of these existing synchronization requirements. Thus, achieving such requirements is not the focal point of this thesis. It is also important to emphasize that the baseline configuration significantly impacts system performance, as it determines the relative sparseness of the total virtual array. A thoughtfully chosen baseline helps to reduce SLL and enhances overall detection capabilities (angular resolution). While the baseline size is typically predetermined by vehicle design and automotive integration constraints, our approach can effectively adapt to the specified baseline configuration and propose suitable array designs accordingly. This extension work provides insights to readers who may have an interest in the joint optimization of mono-static and bi-static mode with a suitable baseline as prior knowledge.

4.6 Conclusion

In this chapter, the probabilistic sampling strategy for sparse array design in distributed radar systems is described in detail. Our approach transforms antenna selection into a trainable, differentiable optimization task through Deep Probabilistic Subsampling with CRLB integration. Analysis of CRLB formulations shows that the worst-case dual-target CRLB provides a degree of balance between angular resolution and sidelobe performance. The Joint-DPSC methodology addresses unique challenges in transmitter-receiver optimization across operational modes. For mono-static configurations, we optimize transmitter and receiver arrays independently while capturing virtual array interactions. Due to the flexibility and generalization of J-DPSC, we can easily extend it to non-co-located array optimization and even joint mono-static and bi-static mode optimization. Beyond that, the Neighborhood Masking Mechanism ensures physical realization by enforcing practical spacing constraints. Summarizing, this framework advances beyond conventional sparse array design with lower computational complexity, better generalization, and integrated implementation constraints. Its end-to-end differentiable nature enables efficient optimization through standard gradient techniques, making it applicable to real-world radar system design challenges.

5 Evaluation Results

This chapter presents comprehensive validation of our proposed DPSC and J-DPSC methodologies through extensive simulation analysis. We demonstrate the effectiveness of Deep Probabilistic Subsampling with Cramér-Rao Lower Bound optimization for virtual sparse antenna array design, showcasing remarkable symmetry and regularity in sparse array configurations that maximize aperture rather than sampling density. The Joint-DPSC framework extends to distributed radar networks, achieving superior performance in both bi-static and mono-static modes. Through rigorous comparison with established convex optimization techniques and comprehensive Monte Carlo simulations, we validate that our probabilistic selection strategies consistently outperform random selection and achieve performance comparable to fully populated arrays using significantly fewer elements. The evaluation encompasses single-target and dual-target scenarios, explores scalability from two-sensor to three-sensor networks, and critically examines near-field operational limits. Our findings reveal fundamental trade-offs between angular resolution and sidelobe suppression, demonstrate the capability of FFT processing over matched filter in near-field conditions, and establish the remarkable super-resolution capabilities of deterministic maximum likelihood algorithms when applied to our optimized sparse array configurations.

5.1 DPSC on virtual ULA optimization

This section demonstrates the capabilities of our DPSC approach for optimizing sparse array configurations from virtual ULA geometries. Through comparison with established CRLB-based convex optimization techniques [23], we validate the effectiveness and correctness of our method while showcasing its advantages. For fair and successive comparisons, the scenario setup is picking 16 elements out of 64 candidates ($\lambda/2$ spacing) to achieve sparse array design for the following subsections. The selection of 16 elements corresponds directly to our optimization configuration of 4 transmitters and 4 receivers, which yields 16 virtual array elements according to MIMO radar principles. The full candidate set of 64 elements is chosen to guarantee sufficient freedom of selection and provide potential spacing gaps between selected elements, which enables us to better observe and analyze the SLL differences when using different types of CRLB formulations.

5.1.1 Single-target CRLB-based optimization

In this subsection, we focus on single-target CRLB-based optimization, which serves as a starting point to evaluate the capability of DPSC.

As mentioned in Section 4.2.2, the differentiability in the downstream task model needs to be ensured. In fact, it is reasonable to incorporate the selection vector into the first and second moment in Equation (3.15) since they effectively capture the spread of active antennas in the sparse array. Position values weighted by soft probabilities can provide a meaningful approximation. They are replaced by their soft counterparts as:

$$M_1^{\text{soft}} = \frac{\sum_{m=0}^{M-1} p_m * \tilde{d_m}}{\sum_{m=0}^{M-1} p_m} \tag{5.1}$$

$$M_2^{\text{soft}} = \frac{\sum_{m=0}^{M-1} p_m * \tilde{d_m^2}}{\sum_{m=0}^{M-1} p_m} \tag{5.2}$$

We trained the model using 12,800 samples across 100 epochs, with each epoch comprising 256 simulated data samples. Each sample consists of a coupled data pair containing one DoA angle and its corresponding SNR (e.g., $[DoA, SNR]$). Since the single-target CRLB neglects SLL optimization, we applied no constraints on data generation. For each sample, a single target at 20 dB SNR was randomly positioned within a Field of View ranging from -80° to 80°. For stochastic optimization, we employed the Adam optimizer with hyperparameters $\beta_1 = 0.9$, $\beta_2 = 0.999$, and $\epsilon = 1e-7$. The learning rate was set to $5e-2$.

The selection result is shown in Figure 5.1. The resulting array exhibits remarkable symmetry and regularity. All selected array elements are positioned on either side of the candidate array, demonstrating an intuitive principle: when optimizing antenna selection for single-target CRLB, it is preferable to maximize the aperture rather than getting uniform sampling density within the existing aperture. The selection result based on DPSC has been validated through CRLB-based convex optimization [23], confirming the effectiveness of the DPSC approach.

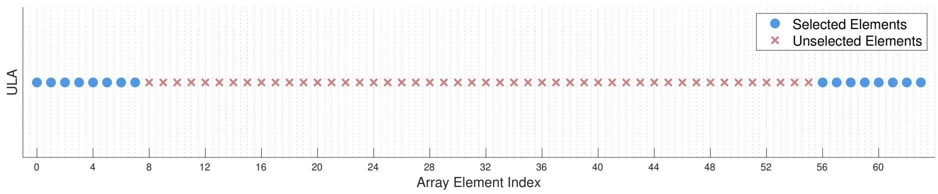

Figure 5.1: Sparse array design result for single-target CRLB-based DPSC optimization. Selected element positions: [0, 1, 2, 3, 4, 5, 6, 7, 56, 57, 58, 59, 60, 61, 62, 63].

5.1.2 Dual-target CRLB-based optimization

To indirectly have SLL control, the dual-target CRLB is used for DPSC. The approximated version of the dual target CRLB from Section 4.2.2 is well prepared for the need for differentiability.

We begin with the best-case CRLB, utilizing the approximation version from Equation (3.25) to reduce computational complexity. Each sample consists of a data vector containing the DoAs and corresponding SNRs for two targets, where each target's DoA is paired with its respective SNR value (e.g., $[DoA_1, SNR_1, DoA_2, SNR_2]$). In each sample, two targets with the same signal power were generated within a Field of View ranging from -80° to 80°. The results displayed in Figure 5.2 demonstrate continued symmetry and regularity. The selected antennas are organized into three distinct clusters: two positioned at the edges and one in the center. This configuration suggests that the SLL will be lower than in the single-target CRLB optimization due to the reduced gaps within the aperture. The validity of this result is further confirmed through comparison with the findings presented in [23].

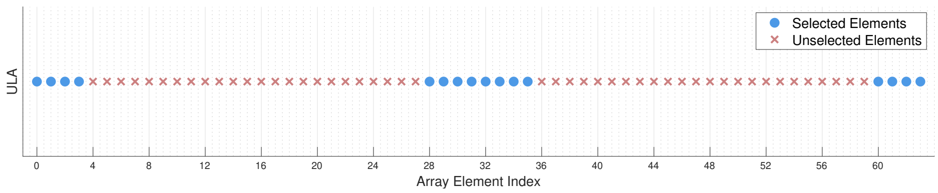

Figure 5.2: Sparse array design result for best-case CRLB-based DPSC optimization. Selected element positions: [0, 1, 2, 3, 28, 29, 30, 31, 32, 33, 34, 35, 60, 61, 62, 63].

To move further, the worst-case CRLB and specific constraints applied during data generation are used to suppress the SLL for sparse array design. The first DoA angle is always placed at 0° (broadside), while the second DoA angle is varied within a source separation range of 3° to 20°, resulting in a total angular range of [-20°, 20°]. This approach helps to suppress SLL around the broadside while ensuring a low CRLB, leading to more robust and practical sparse antenna array design. The Figure 5.3 indicates a more spread antenna selection result than above, which will give us better SLL control.

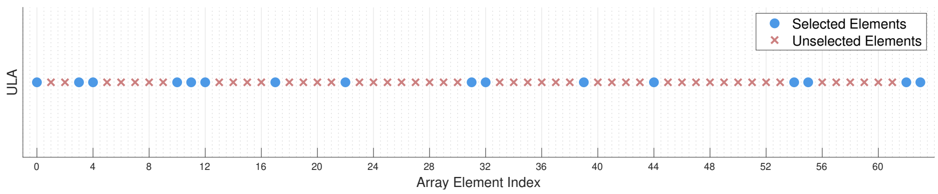

Figure 5.3: Sparse array design result for worst-case CRLB-based DPSC optimization. Selected element positions: [0, 3, 4, 10, 11, 12, 17, 22, 31, 32, 39, 44, 54, 55, 62, 63]

Table 5.1 provides a quantitative comparison between different loss function-based designs. Results demonstrate that the dual-target CRLB indirectly controls SLL when performing the task. Among these methods, the worst-case CRLB delivers the best performance on SLL control, albeit with some sacrifice in resolution compared to single-target CRLB. As expected, the worst-case CRLB demonstrates greater capability when working with larger candidate sets, since the patterns of single-target and best-case CRLB designs indicate that unselected gaps increase correspondingly, resulting in higher SLL. Figure 5.4 presents a visualization of the beampattern based on matched filtering for a target at exact broadside for reference.

Table 5.1: Performance Comparison of Different Loss Function-Based Designs

Method	**PSL (dB)**	**MLW (deg)**
Single-target CRLB design - Eq. (3.15)	-0.29	1.02
Best-case CRLB design - Eq. (3.17)	-0.62	1.37
Worst-case CRLB design - Eq. (3.17), (3.26)	-5.81	1.37

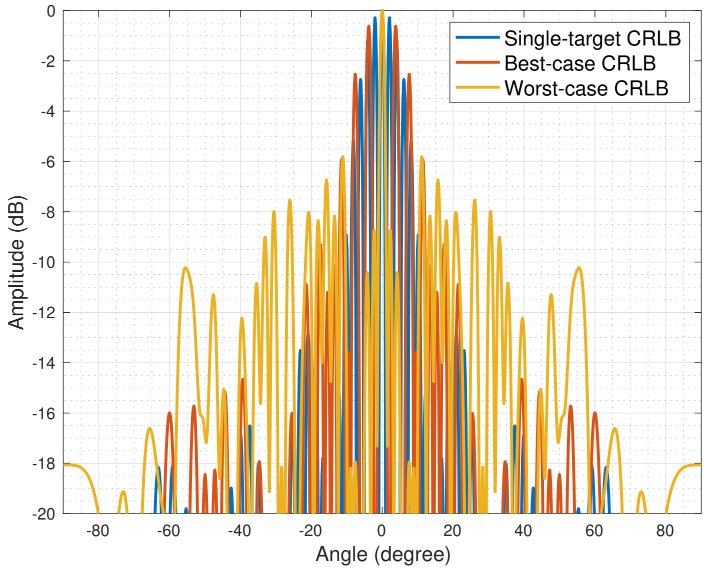

Figure 5.4: Beampattern comparison between different loss function-based designs

5.2 J-DPSC on Tx-Rx optimization for two-sensor radar network

This section explores J-DPSC as an effective approach for optimizing transmitters and receivers simultaneously in a two-sensor distributed radar system. As shown in Section 2.1.3, mirror configuration for two sensors is adopted as it provides a large aperture for bi-static responses. The workflow of J-DPSC for bi-static mode optimization is illustrated in Section 4.5.2.

For training setup, we train the model using 51,200 samples over 120 epochs, with each epoch consisting of 512 simulated data samples. Each sample consists of a data vector containing the DoAs and corresponding SNRs for two targets, where each target's DoA is paired with its respective SNR value (e.g., $[DoA_1, SNR_1, DoA_2, SNR_2]$). To account for SLL considerations, specific constraints are applied during data generation. The first DoA angle is always placed at 0° (broadside), while the second DoA angle is varied within a source separation range of 1.5° to 15°, resulting in a total angular range of [-15°, 15°]. Additionally, we introduce two different SNR values [20 dB, 10 dB] to enhance the CRLB sensitivity to SLL. This approach helps suppress SLL around the broadside while ensuring a low CRLB, leading to more robust and practical sparse antenna array design.

The Adam optimizer is employed for stochastic optimization, with hyperparameters $\beta_1 = 0.9$, $\beta_2 = 0.999$, and $\epsilon = 1e-7$. The initial learning rate is set to $5e-2$ and follows an exponential decay strategy with a decay parameter of 0.96, helping to prevent convergence to local minima.

Given the physical size of the envisaged radar chip (6 cm, around 16 wavelengths for a carrier frequency of 79 GHz), the candidate positions for transmitters and receivers are defined as [0:1:15] and [-16:1:0], respectively, with positions normalized by $\lambda/2$. The overlapped zero-index candidate is strategically positioned to fill the natural gap between two bi-static response candidates. From these candidate positions, four elements are selected for both transmitters and receivers. The proposed J-DPSC framework achieves a compression ratio CR of 6%.

It should be emphasized that SLL consideration is indirectly addressed in worst-case CRLB, though not as the dominant objective, creating a fundamental trade-off between angular resolution and SLL. When mapped to neural network optimization, this parallels the challenge of approaching—but not precisely reaching—global minima. Consequently, minor hyperparameter adjustments yield different outputs, necessitating comparative analysis of multiple sparse array designs to evaluate their beampattern performance.

Furthermore, to achieve superior SLL suppression, a full search algorithm with PSL as the cost function is applied to the DPS output. Rather than selecting only the Top4 candidates for antenna configuration, an expanded pool of Top8 candidates can be utilized. Analysis of the logits values reveals that while the Top3 candidates approach values of 1, the fourth candidate shows notably lower values, highlighting the inherent competition between key performance indicators. This pattern occurs simultaneously for both transmitters and receivers. The implemented strategy involves running a full search algorithm to identify the optimal final element that minimizes SLL for a chosen optimization range. While this approach necessarily compromises some resolution, the trade-off is acceptable since most sample points remain fixed, allowing us to achieve significantly improved SLL performance.

The Figure 5.5 and 5.6 compare transmitter and receiver selection patterns across multiple array configurations. An antenna array that is implemented in a prototype radar sensor of NXP is denoted as 'NXP baseline'. Proposed-1 is one of the generated results from J-DPSC without NMM and postprocessing. Proposed-2 demonstrates NMM effectiveness with λ minimum spacing knowledge, while Proposed 3-5 show how full search algorithms with different optimization ranges produce varied selection patterns. Blue dots represent selected elements; red x marks show unselected ones. These variations illustrate how different parameters impact array design for specific applications. To improve readability for readers, the antenna position is also marked on the selected elements.

After visualizing the selection patterns for transmitter and receiver, we show the bi-static responses for the distributed radar system containing two identical sensors positioned as mirrors to each other. A demonstration based on the MIMO principle is shown in Figure 5.7 as follows.

A quantitative comparison between array layouts is given in Table 5.2 and 5.3

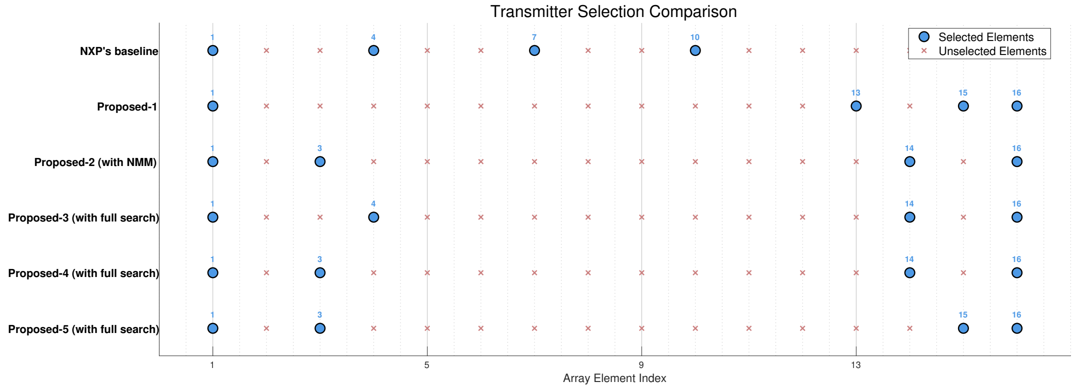

Figure 5.5: Transmitter selection comparison between current implementation ('NXP baseline') and our proposed arrays (The maximum aperture is fixed while the distribution of sampling points within the aperture is varied to adjust SLL performance)

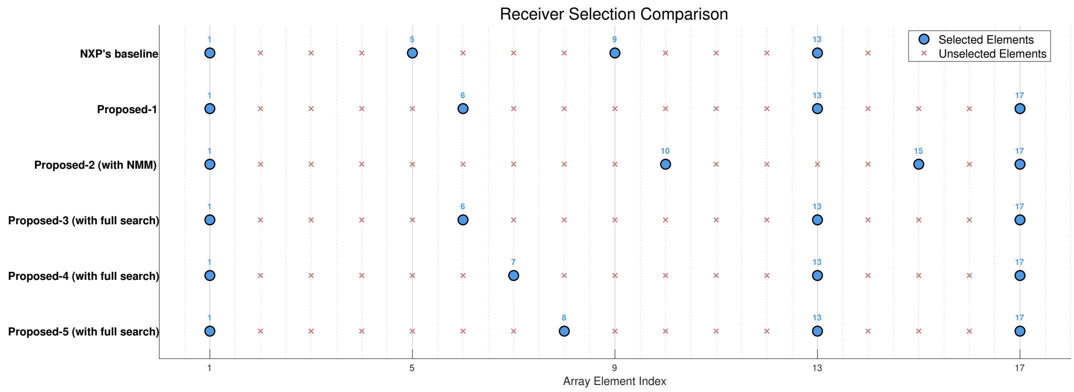

Figure 5.6: Receiver selection comparison between current implementation ('NXP baseline') and our proposed arrays (The maximum aperture is fixed while the distribution of sampling points within the aperture is varied to adjust SLL performance)

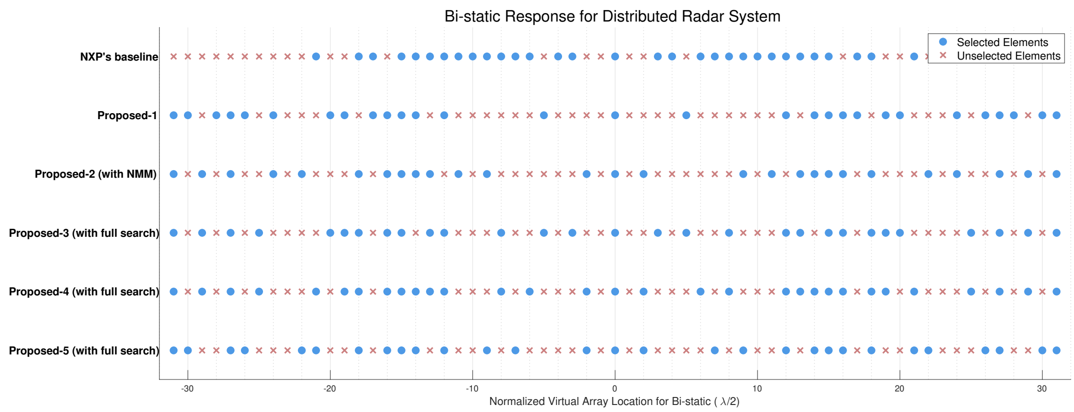

Figure 5.7: Formed bi-static response through optimized transmitter and receiver selections

to provide a straightforward comparison. Table 5.2 shows the comparison between main lobe width (MLW), PSL and PSL location for bi-static response formed by the distributed radar system. While the NXP's baseline array exhibits notably larger MLW due to its smaller aperture, making direct comparison challenging, it remains a valuable reference point. Since this current implementation configuration utilizes the same radar chip without occupying the entire available length, including it here demonstrates the performance improvements achievable when maximizing spatial utilization of the platform. The resolution consideration is the dominant factor in CRLB computation, making the Proposed-1 sparse array superior in resolution among all proposed arrays while maintaining acceptable PSL. The Proposed-2 sparse array validates our NMM approach with physical constraints included. Although its PSL is elevated, it occurs near the end-fire angle, preserving effectiveness for narrow Field-of-View (FoV) detection applications. When integrated with the full search algorithm, the PSL can be further reduced to -10 dB with only a minor sacrifice of approximately 0.1° in resolution—a performance level well-suited for industrial applications. Similarly, Proposed-4 exhibits higher SLL, but as these are concentrated around the end-fire angle, they remain acceptable. The remaining SLL remains below -10 dB, meeting design specifications. A more intuitive visualization of the beampattern will be presented in subsequent figures.

It is notable that we also include the array layout derived from convex optimization [23] for comparison. Specifically, there are 63 candidate positions available, and to match the virtual elements of our proposed array, 32 elements are selected following the pattern illustrated in Figure 5.2. While this comparison is not entirely fair since the convex optimization directly targets the virtual array, it nonetheless provides meaningful insight into the SLL suppression capability of our proposed approach.

Table 5.2: Performance Comparison of Different Array Layouts for Bi-static Response

	MLW (deg)	**PSL (dB)**	**PSL Location (deg)**
NXP's baseline	2.46	-9.97	34.67
Fully populated ULA-63	1.60	-13.25	2.59
Convex optimization [23]	1.49	-3.02	4.05
Proposed-1	1.42	-7.48	2.45
Proposed-2 (with NMM)	1.49	-4.06	63.91
Proposed-3 (with full search)	1.60	-9.99	7.69
Proposed-4 (with full search)	1.59	-5.93	74.83
Proposed-5 (with full search)	1.59	-9.13	58.92

Before analyzing beampattern performance, it is essential to examine mono-static mode performance concurrently. While coherent bi-static response processing enhances resolution and provides processing gain, it is crucial to note that utilizing this bi-static response necessitates targets being simultaneously visible to both radar units as a fundamental prerequisite. Evaluating mono-static response performance remains valuable, as targets may occasionally be detectable by only one radar unit. The proposed J-DPSC approach inherently optimizes mono-static performance alongside bi-static optimization due to the underlying system architecture. Since the bi-static configuration employs the mirror principle, where the bi-static array is essentially composed of two mono-static arrays, the sparsity pattern that optimizes the bi-static response naturally translates to effective mono-static performance. The DPS layer's construction, designed to optimize bi-static arrays under the mirror condition, ensures that each constituent mono-static array maintains optimal characteristics as well. Table 5.3 demonstrates that the proposed arrays can approximate fully populated arrays in terms of resolution while maintaining acceptable SLL. This indicates that J-DPSC delivers effective sparse array results for both bi-static and mono-static responses in a single training session, rather than requiring separate training processes—making it more versatile and broadly applicable.

Table 5.3: Performance Comparison of Different Array Layouts for Mono-static Response

	MLW (deg)	**PSL (dB)**	**PSL Location (deg)**
NXP's baseline	5.32	-9.88	34.45
Fully populated ULA-32	3.17	-13.25	5.14
Convex optimization [23]	2.93	-2.85	7.99
Proposed-1	3.46	-7.81	31.79
Proposed-2 (with NMM)	3.28	-4.05	63.77
Proposed-3 (with full search)	3.33	-8.49	56.09
Proposed-4 (with full search)	3.30	-5.52	73.42
Proposed-5 (with full search)	3.27	-8.54	57.47

A visualization of the bi-static and mono-static response beampatterns is presented in Figures 5.8a and 5.8b, with selected array layouts shown to enhance readability. The proposed sparse arrays demonstrate superior performance compared to NXP's baseline and achieve angular resolution comparable to fully populated arrays. When examining different proposed array configurations identified through our J-DPSC with concatenated full search algorithm, we observe that PSL can be further suppressed within defined search ranges. For instance, Proposed-4 exhibits elevated SLL at end-fire angles, while maintaining all other lobes below -10 dB. Notably, the mono-static mode beampatterns across all configurations demonstrate similar performance characteristics, which strengthen the effectiveness of the J-DPSC approach. A zoomed-in examination for resolution for Figure 5.8 is shown in Figure 5.9.

The reader may note the absence of state-of-the-art sparse array design approaches comparable to our proposed method, except for the convex optimization described in [23]. This is because to the best of our knowledge, no effective method currently exists for non-co-located sparse array design in the open radar literature. Existing methodologies primarily focus on extending joint transmitter-receiver selection rather than addressing distributed radar systems, making direct array layout comparisons unfair. Nevertheless, on an application level, the potential and flexibility of J-DPSC are already evident. The significant reduction in training parameters combined with our specialized loss function design substantially decreases both training time and complexity compared to other learning-based methods. Our J-DPSC approach

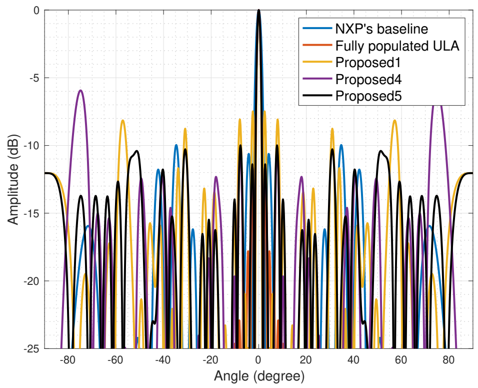

(a) Bi-static mode beampattern comparison

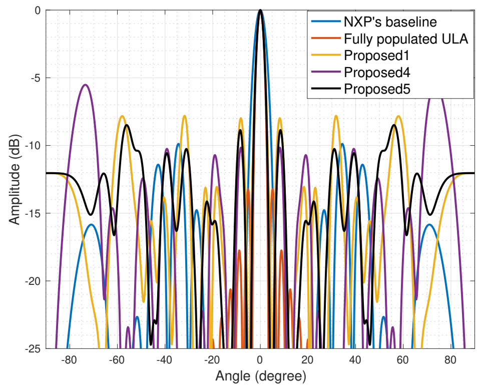

(b) Mono-static mode beampattern comparison

Figure 5.8: Beampattern visualization comparison for bi-static mode and mono-static mode when target located at exact broadside

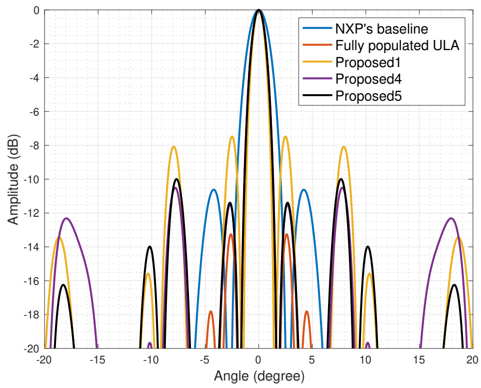

(a) Bi-static mode beampattern comparison

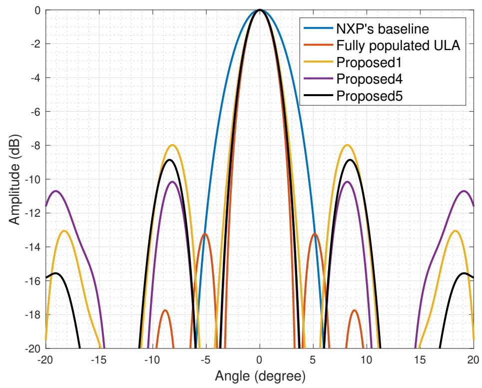

(b) Mono-static mode beampattern comparison

Figure 5.9: Zoomed-in examination of beampattern visualization comparison for bi-static mode and mono-static mode when target located at exact broadside

transforms the traditionally exponential sensor selection problem into a polynomial-time solution with training complexity $\mathcal{O}(E \cdot B \cdot N^2)$, where E represents the number of training epochs, B represents the batch size and N represents the virtual array size. This efficiency gain becomes particularly evident when compared to existing neural optimization approaches. In [28], their work requires joint optimization of both antenna positions and DNN parameters with complexity $\mathcal{O}(K \cdot B \cdot (L \cdot H^2 + M \cdot N))$, where K represents training iterations that can reach millions, B represents batch size, L represents the number of layers, H represents the maximum neurons per layer, M represents the number of sources, and N represents the number of antennas. Furthermore, the two-target Cramér-Rao bound sensor selection approach by [23] exhibits complexity $\mathcal{O}(|D|^3 \cdot N^3 \cdot \log(1/\varepsilon))$ due to semidefinite programming constraints, where $|D|$ represents the grid size for worst-case optimization and ε represents the convergence tolerance. The cubic dependency on both grid size and array dimension in traditional convex optimization methods clearly demands significantly more computational resources than our quadratic scaling approach, while our method maintains superior performance through the learned probabilistic sampling strategy and specialized bi-static loss formulation.

5.3 J-DPSC on Tx-Rx optimization for three-sensor radar network

As established in Chapter 1, high generalization capability is a critical factor in our proposed approach. A significant advantage of our J-DPSC method is its straightforward extensibility to three-sensor network Tx-Rx optimization with minimal technical modifications, enhancing its value for multi-sensor network applications.

In this configuration, we introduce a third radar unit at the center position in addition to the two mirror-configured sensors positioned on either side. Since our current implementation permits antenna placement within the same physical column location on the radar unit, we can relax the restrictions on transmitters and receivers selection ranges, thereby enabling a larger effective aperture. Specifically, our optimization target encompasses six bi-static responses inherently generated by this three-sensor network, demonstrating the scalability of our approach to multi-sensor distributed radar configurations.

A detailed illustration of the system is presented in Figure 5.10. The configuration incorporates T_1 and T_2, each containing 4 transmitters and 4 receivers, while introducing a centrally positioned sensor T_3 with a distinct array layout to provide a larger aperture than the two-sensor radar network alone. The complementary schematics for transmitters and receivers are clearly labeled in the diagrams. For T_1 and T_2, the two-column format represents different selection ranges for transmitters and receivers, whereas for T_3, it indicates that the full selection range for both transmitters and receivers is simultaneously available. The dotted lines represent electromagnetic wave propagation paths showing different DoA and DoD across the array aperture. However, the optimization scheme and resulting array configurations are analyzed using the standard virtual antenna array concept, which assumes far-field behavior for all propagation paths. The validity of this approach is examined in Section 5.4.

A comprehensive visualization of the full bi-static response generated by three sensors is presented in Figure 5.11. For clearer and easier visualization, we selected a baseline of 40 cm. The response comprises six distinct groups formed by various transmitter-receiver combinations. These groups can be categorized into three clusters—one positioned centrally and two on the sides with overlapping locations. It is evident that the baseline selection determines the spacing between clusters, which consequently influences the proximity of the nearest SLL.

The fundamental principle for bi-static optimization is illustrated in Figure 4.5. Due to the inclusion of the center sensor T_3, two parallel DPS are implemented to manage the selection of transmitters and receivers for T_3. The selection logits for each bi-static response are concatenated and subsequently fed into the loss function calculation to complete the forward pass. The back-propagation procedure then updates all logits, thereby concluding the training process.

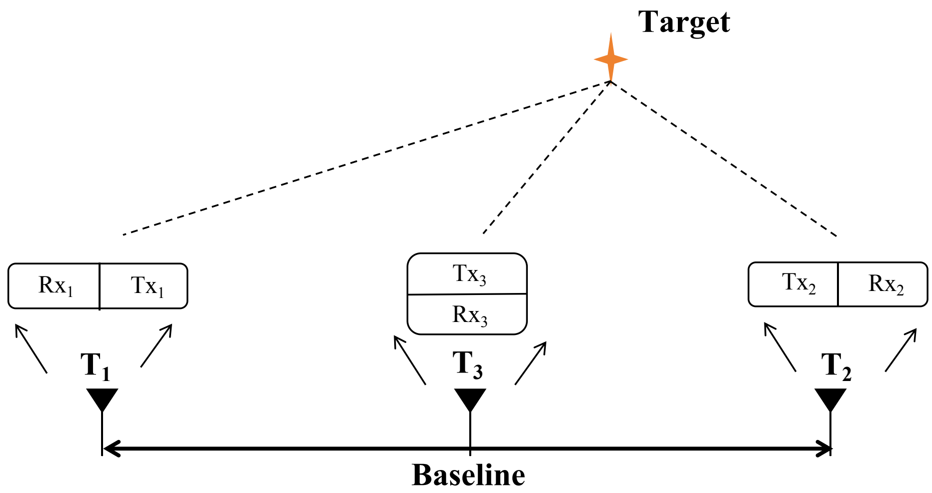

Figure 5.10: Three-sensor distributed radar network

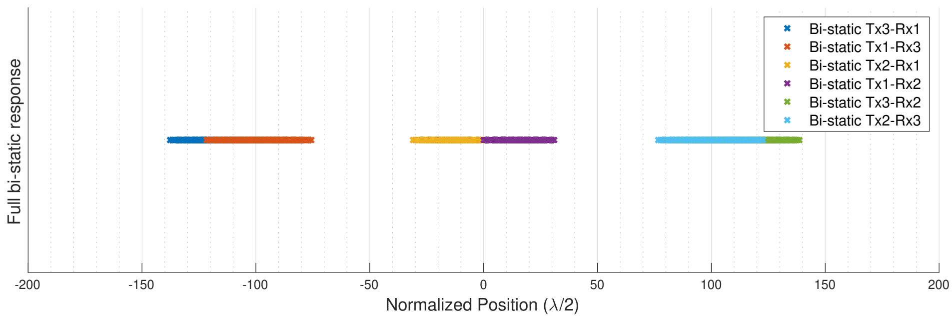

Figure 5.11: Bi-static response using full array from three sensors

We present optimization results for baselines of 40 cm and 20 cm. As these results directly relate to distributed radar system design setup, we focus on key insights rather than specific selection details. A high level visualization of selection results of bi-static response is given in Figure 5.12. Notably, larger baselines inevitably create gaps in coverage. However, an important observation is that the clusters on each side comprise different transmitter-receiver pairs with distinct characteristics. This asymmetry allows for strategic positioning of the center sensor through left-right adjustments, which can alter the distribution of sampling points and consequently reduce PSL. This finding highlights the importance of considering not just element spacing but also the specific transmitter-receiver pairings between sensors in distributed array optimization.

The beampattern results from the optimized array layout are now examined. For the 40 cm baseline configuration, the center sensor was shifted by -6 cm to modify the spatial sampling distribution of the total bi-static response. A short-range optimization scan from -10 cm to 10 cm was performed to determine the optimal shift position.

As demonstrated in Figure 5.13, the optimization results reveal distinct performance

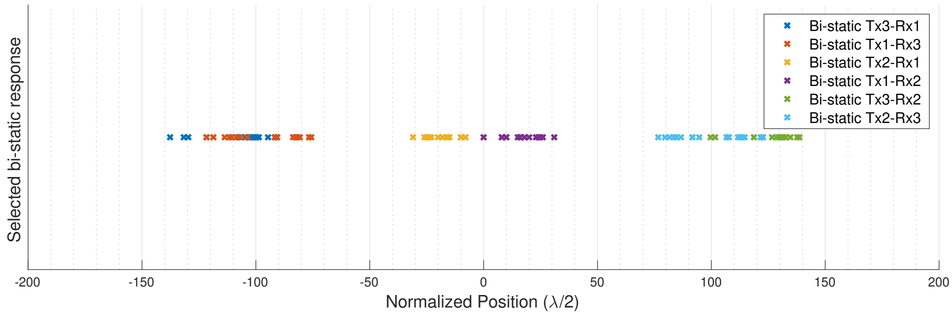

Figure 5.12: Bi-static response using optimized sparse array from three sensors

characteristics for different baseline configurations. For the 20 cm baseline, all SLL can be successfully suppressed below -10 dB. However, for the 40 cm baseline, even with the implemented shifting strategy, the minimum PSL remains around -7 dB. This observation reinforces the fundamental principle that baseline selection primarily determines the achievable PSL performance.

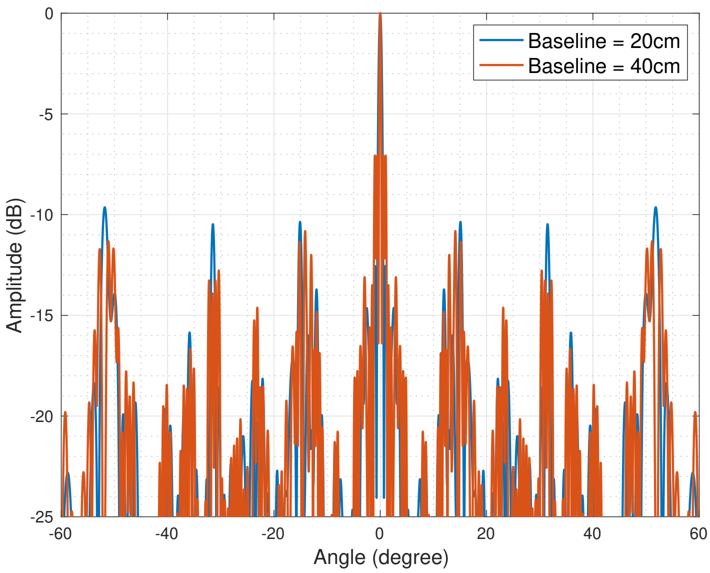

Figure 5.13: Beampattern for six bi-static responses formed by three sensors

This analysis provides valuable insights for multi-sensor radar network optimization and demonstrates the flexibility of the proposed method. The framework can be readily adapted by researchers for specific applications and requirements.

5.4 Near-field DoA estimation performance examination

This section investigates the behavior and capabilities of the proposed array configurations when operating in near-field conditions. The previous analysis relied on virtual array concepts that are fundamentally based on far-field assumptions, where wavefronts are treated as planar across the array aperture. However, when targets are located in the near-field relative to the entire distributed system, wavefronts exhibit significant curvature that challenges the applicability of these conventional virtual array methods. This section examines whether our sparse array optimization approach, developed under far-field assumptions, maintains its effectiveness when applied to near-field scenarios where the theoretical framework may no longer be strictly valid. The following analysis evaluates how effectively our sparse array designs maintain their performance advantages when targets are positioned within the near-field region, with particular attention to resolution preservation, SLL management, and detection performance.

Based on the geometry illustrated in Section 2.1, we can simulate the response of each transmitter-receiver pair with corresponding range information. By systematically varying the parameter R, we can directly compare the DoA estimation performance under both near-field and far-field conditions. The baseline between two sensors is set at 0.5 m, resulting in a calculated Fraunhofer Distance of approximately 165 m. Figures 5.14a and 5.14b display the beampattern when targeting an object at 20° and a range of 200 m, comparing the matched filter method with FFT processing. Since the target is in the far-field region, these two methods should theoretically yield identical results. The demonstration confirms this expectation and clearly illustrates the 6 dB coherent gain achieved by utilizing both bi-static responses. Path 1 and Path 2 represent the individual bi-static responses, respectively.

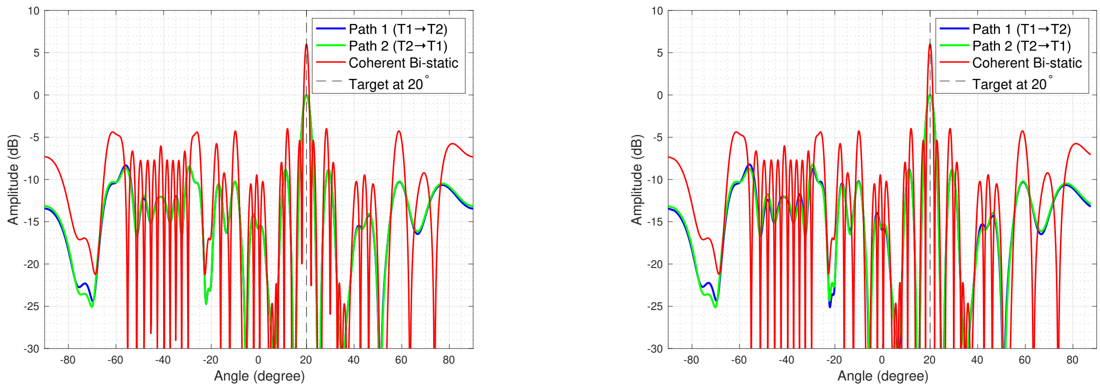

(a) (b)

Figure 5.14: Beampattern comparison between two beamforming algorithms when target at 20° and range 200 m: (a) Matched filter, (b) FFT

As we gradually move the target into the near-field region, we can observe potential performance degradation. Figure 5.15 illustrates that as the target approaches the distributed radar system, the side lobes progressively increases. This directly impacts individual bi-static usage, while the coherent bi-static approach demonstrates greater robustness compared to individual utilization.

When the range is 20 m, the results in Figure 5.15a and Figure 5.15b indicate the coherent bi-static beamforming performance is still similar to the far-field behavior.

When comparing matched filter with FFT processing methods, we observe that the matched filter continues to perform effectively even when the target is in close proximity. However, with FFT processing, a target that is sufficiently close presents a risk where side lobes may surpass the main lobe, potentially causing deteriorated performance. Nevertheless, it remains possible to identify appropriate distance in spatial domain and angular domain where FFT processing performance remains acceptable.

Then it is meaningful to explore the joint effect of target location and distance for near-field DoA estimation. Still, only one target is available for target detection. This analysis is done via heat maps shown in Figure 5.16, presenting a comprehensive analysis of coherent bi-static response performance across varying ranges and angles for FFT processing. The leftmost sub-figure displays angle detection error, showing minimal errors (dark blue) across most of the operational range-angle space, with slightly increased errors (red) only at extremely short ranges below 5 m. This actually arises when the side lobes surpass the main lobe. What is interesting is that even at short ranges, when the target is moved to the off-broadside angle, the detection becomes successful again. The center sub-figure illustrates peak sidelobe levels, demonstrating excellent sidelobe suppression (dark blue) throughout most of the detection space, with marginally higher sidelobe levels (lighter blue) appearing only at the closest ranges, where false alarms are produced by high side lobes. The rightmost sub-figure depicts the 3 dB beamwidth, revealing a gradual widening of the main beam (transition from blue to red) as the detection angle increases, which is consistent with typical radar beampattern behavior due to the change of effective aperture. Together, these visualizations confirm that our proposed sparse array for distributed radar systems maintains robust performance in near-field conditions when using FFT-based processing, with expected degradation occurring only at the nearest ranges and broadside angles. It should be noted that this degradation is primarily attributed to the FFT processing methodology rather than inherent limitations of the sparse array configuration itself. When employing matched filter processing, the array performance would remain consistent across all ranges, as matched filtering does not suffer from the same near-field approximation errors. Therefore, these results demonstrate the effectiveness of our sparse array design while highlighting the importance of processing technique selection for optimal performance in near-field scenarios.

A detailed examination of Figure 5.16 at the shorter ranges reveals the conditions under which false detections occur for close-range targets at broadside angles because of large pointing errors. Figure 5.17 provides a closer view, showing that performance degradation begins at approximately 5.25 m, which is quite a close range. As the target range decreases, the angular threshold at which localization accuracy deteriorates progressively increases. This analysis provides valuable insight into the operational limits of FFT-based processing for near-field target detection.

Figure 5.18 takes DoD from T_1 and DoA at T_2 as an example, providing critical insight into the performance anomaly observed at close ranges. At a range of 5 m, a significant discrepancy emerges between the DoD and DoA, most pronounced at broadside angles. This angular difference causes tolerance for conventional FFT processing, resulting in detection failures. However, as the target transitions to off-broadside angles, the difference between DoD and DoA progressively reduces, restoring

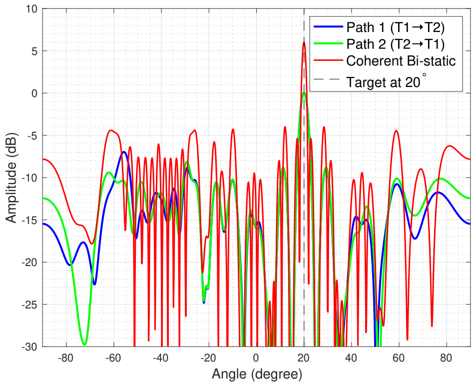

(a) Matched filter for range 20m

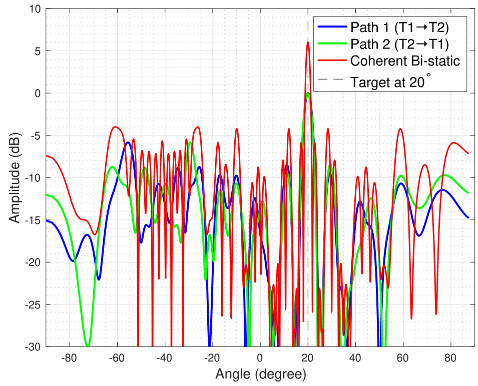

(b) FFT for range 20m

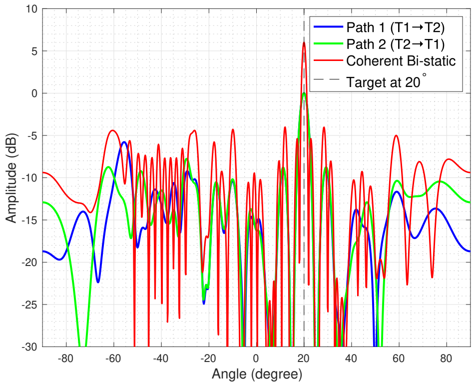

(c) Matched filter for range 10m

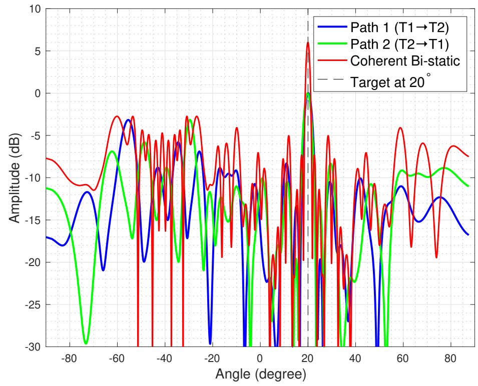

(d) FFT for range 10m

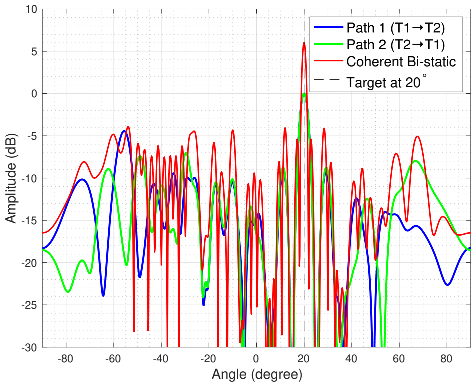

(e) Matched filter for range 5m

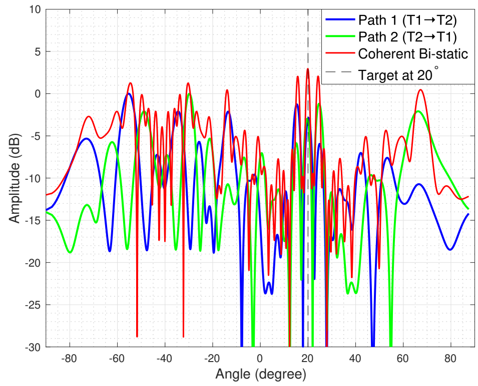

(f) FFT for range 5m

Figure 5.15: Beampattern comparisons between two beamforming algorithms under three different target range values

successful detection capability. This phenomenon explains the observed performance discontinuity in the near-field region and highlights the fundamental limitation of standard far-field processing techniques like FFT processing when applied to targets within the near-field boundary, particularly at broadside orientations. Meanwhile, for

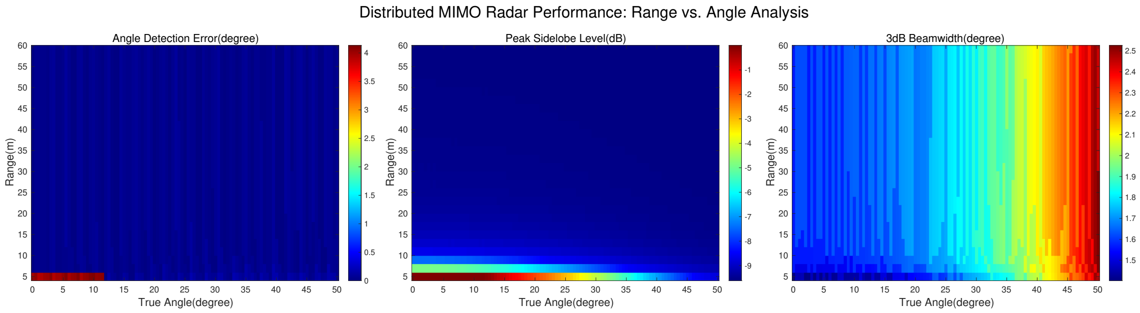

Figure 5.16: Comprehensive analysis of joint range and angle effects on FFT processing for near-field target detection. Left: Angle detection error (in degrees) showing the deviation between estimated and true target angles across different range-angle combinations. Center: Peak sidelobe level (in dB) indicating the maximum sidelobe magnitude relative to the main lobe for various target positions. Right: 3dB beamwidth (in degrees) demonstrating the angular resolution capability as a function of target range and angle

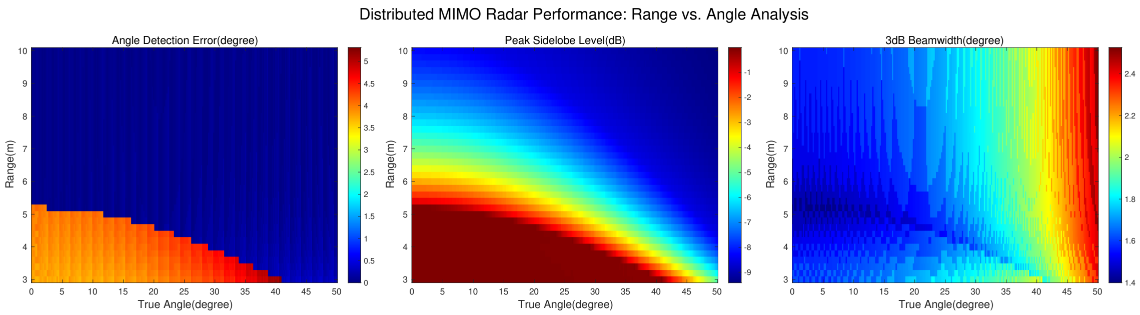

Figure 5.17: Short range examination of joint range and angle effects on FFT processing for near-field target detection. Left: Angle detection error (in degrees) showing the deviation between estimated and true target angles across different range-angle combinations. Center: Peak sidelobe level (in dB) indicating the maximum sidelobe magnitude relative to the main lobe for various target positions. Right: 3dB beamwidth (in degrees) demonstrating the angular resolution capability as a function of target range and angle

the far-field region, the difference between DoD and DoA for distributed radar systems is not a problem anymore. This analysis demonstrates how angular relationships in distributed MIMO systems transform across the near-field to far-field transition.

Based on the comprehensive analysis presented in Figure 5.18 and the detailed examination in Figure 5.17, the critical phase difference threshold that triggers deteriorated performance can be precisely quantified. Table 5.4 presents the maximum allowable phase differences at various target ranges before detection failure occurs. The dots in Table 5.4 indicate a predictable pattern in the data: as range decreases, the critical angle increases, and correspondingly, the maximum phase difference also increases. However, examining too close range scenarios and their corresponding values provides limited practical insight, so these data are not presented here.

A conservative detection threshold emerges from this analysis: maintaining phase differences below 5° ensures reliable target detection across the operational range.

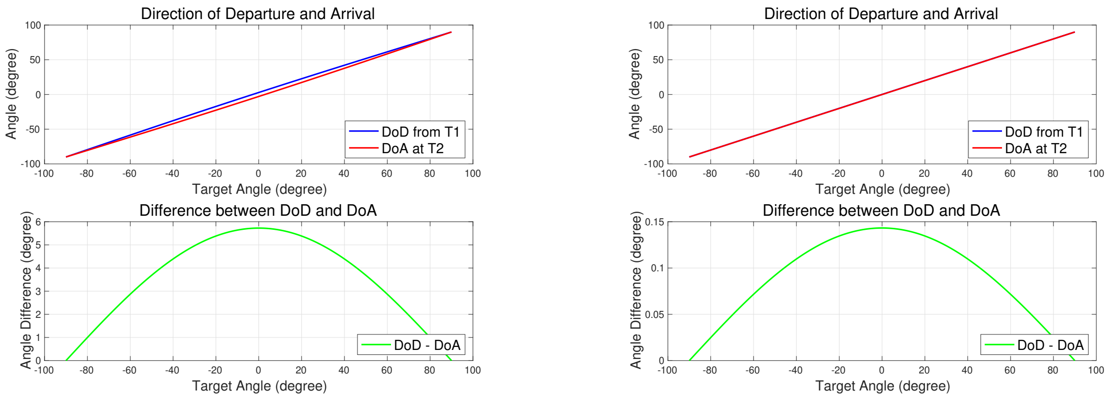

(a) (b)

Figure 5.18: DoD vs DoA for close range and far range with (a) R = 5 m, (b) R = 200 m

However, it is crucial to note that while closer ranges permit larger phase differences before complete detection failure, they simultaneously exhibit elevated PSL, which can degrade overall detection quality even when the primary target remains detectable.

Table 5.4: Critical phase difference thresholds for reliable target detection at various ranges

Range (m)	**Critical Angle (deg)**	**Maximum Phase Difference (deg)**
5.2	2.4	5.48
5.0	11.6	5.61
4.8	16.2	5.72
4.6	20.0	5.85
4.4	23.2	5.98
...	...	...

This section has demonstrated that while J-DPSC is fundamentally based on far-field assumptions, the predicted DoA performance remains valid when dedicated matched filter processing is applied under near-field conditions. Remarkably, even conventional beamforming using FFT processing provides robust results at target ranges significantly smaller than the Fraunhofer distance of the distributed radar system. These findings validate the practical applicability of our virtual array-based optimization approach beyond its theoretical far-field limitations. The results obtained from both FFT processing and matched filter methods establish confidence in the method's robustness and provide a solid foundation for future research, where more advanced DoA estimation algorithms and complex near-field scenarios can be explored and studied in greater depth.

5.5 Performance analysis of DoA estimation

This section presents a comprehensive analysis of DoA estimation performance for the dual-target case using our proposed sparse array layout. We specifically examine the capabilities of distributed radar systems operating in bi-static mode. We begin by detailing the simulation parameters and experimental setup, followed by a systematic evaluation of the sparse array's robustness across varying SNR. Finally, we assess the sparse array detection capability by examining its performance under different source separation scenarios. Through these analyses, we aim to provide quantitative insights into the practical efficacy of our proposed array under diverse operational conditions.

5.5.1 Simulation setup

To assess the DoA estimation performance of the algorithms, Monte Carlo simulations are conducted, focusing on parameters Root Mean Square Error (RMSE). The algorithms produce outputs indicating potential target positions. A thresholding operation is applied, whereby only targets detected with a power exceeding a specified threshold are regarded as valid detections. The detection tolerance window (DTW) is defined as [-3°, +3°] around the ground truth, which is based on comparisons with relevant literature such as [37]. This choice corresponds to approximately twice the MLW, accounting for the phase interaction effects between two closely spaced targets that can influence detection accuracy and angular resolution performance. The tolerance size provides a reasonable margin around the angular resolution limit, accounting for both measurement uncertainties and beam width characteristics of the optimized sparse array. If the estimated value from the algorithm's output falls within the detection threshold window, the target is considered detected, with the closest declaration among these being recognized as the detected target.

RMSE is calculated for each run, which includes N_{mc} Monte Carlo experiments. A description of RMSE performance metrics is provided below.

- Root mean square error: The RMSE quantifies the error in the DoA estimation of the target. It is calculated by taking the square root of the average of the squared differences between the ground truth position of the target and the estimated position determined by the algorithm. The expression is expressed as follows: here, x_i represents the ground truth of the target, and $\tilde{x_i}$ denotes the estimated position found within the DTW for each run. The equation below is applicable to a Monte Carlo run containing N_{mc} experiments in each trial, where N_d indicates the number of times the target is detected within the DTW for a given run. If the target is not detected within the DTW, the RMSE is not computed for that particular experiment. The reason for using RMSE instead of MSE in this context is that RMSE provides a more straightforward comparison with the benchmark CRLB expressed in degrees.

$$\text{RMSE} = \sqrt{\frac{1}{N_d}\sum_{i=1}^{N_d}(x_i - \tilde{x_i})^2} \tag{5.3}$$

Monte Carlo runs are executed for different SNR values and different source separations. The coherent bi-static response is used to show the DoA simulation results. The performance metrics and CRLB discussed above are presented and compared. The signal model is constructed under the far-field assumption. There are several DoA estimation algorithms considered here, with the number of sources provided as prior information to each algorithm. We assume the presence of a reliable source enumeration block that accurately determines the number of targets and provides this information as input to the DoA estimation algorithms. Their detailed explanation is given as follows.

- Fast Fourier transform (FFT): The FFT DoA estimation algorithm is a method used to determine the angles of incoming signals based on their spatial frequency components. It operates by transforming spatial-domain signal data into the angular domain using the FFT, which efficiently computes the discrete Fourier transform. In the context of DoA estimation, the algorithm analyzes the spatial spectrum of the received signals from an array of sensors. By applying the FFT to the signal data collected at different sensor elements, it identifies peaks in the spectrum that correspond to the directions of the incoming signals. It is important to note that the search space for the angle θ is not uniform due to the projection. Thus it is not exactly the same as digital beamforming method with uniform angular grid definition.

- Orthogonal Matching Pursuit (OMP) [38]: The OMP DoA estimation algorithm is a sparse signal processing technique used to determine the DoA of signals at an antenna array. OMP works by representing the received signal as a linear combination of a few steering vectors (each corresponding to a possible direction). It iteratively selects the steering vector that best matches the residual part of the signal. At each step, it:

  1. Matches the residual signal with all possible steering vectors. 2. Selects the steering vector (direction) that best fits the residual. 3. Updates the residual by removing the contribution of the selected direction. 4. Repeats the process until a stopping criterion is met (e.g., prior knowledge of source number found or residual is sufficiently small).

- Deterministic Maximum Likelihood (DML): DML treats the incoming signals as deterministic (non-random) and seeks the set of directions that best fit the observed data. It builds a likelihood function that quantifies how well the modeled signals match the actual received signals for different directions. DML searches for the directions that maximize this likelihood function. The likelihood function used to help with direction finding is expressed as [39]:

  $$\theta_{DML} = \text{argmax}_\theta \{ \frac{1}{M(1-|\alpha_{k,n}|^2)} (|F_k|^2) - 2Re\{\alpha_{k,n} F_k F_n^*\} + |F_n|^2 \} \tag{5.4}$$

  where $\alpha_{k,n}$ is the correlation between two steering vector a_k and a_n, $F_k = a_k^H Y$ is the correlation of the snapshot Y with the beamsteering vector corresponding to DoA angle θ_k.

5.5.2 Evaluation across varying SNRs

In this section, we present evaluation results for dual targets with 4° source separation, comparing random antenna selection, a fully populated array, and our proposed sparse array configuration in bi-static mode. The Proposed-3 array layout is selected from Section 5.2 as the sparse array configuration due to its superior SLL performance, as demonstrated through both quantitative analysis and beampattern evaluation. The detailed antenna positions of the Proposed-3 array are $d_{Tx} = [0, 3, 13, 15]$ and $d_{Rx} = [0, 5, 12, 16]$, defined in $\lambda/2$ (wavelength) units for sensor 1. For sensor 2, these positions are mirrored to achieve the configuration described in Chapter 2. This arrangement produces a bi-static virtual array with positions spanning $d_{virtual}$ =[-31,-29,-27,-25,-20,-19,-18,-16,-15,-15,-13,-12,-8,-5,-3,0,0,3,5,8,12,13,15,15,16,18,19,20,25,27,29,31]. For comparison purposes, we also implement a random antenna selection baseline, where transmitter and receiver positions are randomly selected from the available uniform linear array elements (Tx from [0:15] and Rx from [0:16]) while maintaining the same number of active elements as our optimized configuration.

A total of 500 Monte Carlo experiments are conducted to evaluate the performance, with targets randomly placed in the field of view from -80° to 80°, ensuring the desired 4° separation between two targets is achieved. Each Monte Carlo run consists of multiple experiments where each experiment has different realizations of noise and target phases. For the random antenna selection baseline, each experiment also involves a new random selection of antenna locations from the available uniform linear array elements. Hence, RMSE values are calculated for each run which consists of N_{mc} experiments.

For calculating RMSE, we apply the following methodology: when two targets are detected within the detection tolerance window, RMSE is calculated using equation 5.3. When only one target is detected, we calculate RMSE using the closest ground truth and assign a 3° value to the missing detection. When no targets are detected, we directly assign 6° as the RMSE value. This approach ensures consistent evaluation across all detection scenarios. This configuration can produce significant RMSE variations in random selection when it generates arrays with small apertures. Consequently, we have omitted the confidence intervals for random selection that would typically be included in standard demonstrations. In order to have a fair comparison, the sampling points of FFT will be 1024 across 180 degrees. The grid size of DML will be 1024 in this work. The DoA search grid of OMP is divided into 1801 points over the FoV -90° to +90°, providing 0.1° grid size.

Since the fully populated ULA contains a larger number of sampling points than either the sparse array or random selection configurations, direct comparison would be unreasonable under the SNR per element definition. To ensure a consistent and fair comparison based on SNR per element, array gain has been considered and appropriately compensated for in the analysis, enabling equitable evaluation across all array configurations.

In Figure 5.19, our proposed sparse array clearly outperforms random selection across all evaluated conditions. For both the FFT and OMP methods, when compared to the fully populated array, we observe that at low SNR levels, the full array demonstrates better performance due to its superior SLL characteristics, which provide enhanced resilience to noise. However, at higher SNR levels, the sparse array exhibits better performance than full array. This improvement stems from the sparse array's ability to achieve comparable angular resolution using fewer sampling points, effectively concentrating the available energy more efficiently and reducing the impact of pointing error for off-broadside angles that when sufficient SNR is available.

It is important to emphasize that DML performance is primarily determined by grid size, which explains the similar saturation levels observed across configurations in the high SNR region of Figure 5.19c. Nevertheless, our proposed array demonstrates clear performance improvements over random selection throughout the evaluated range. At -20 dB, the three algorithms exhibit different starting performance levels due to their distinct approaches to handling low SNR conditions, where noise can cause detections to jump to sidelobes rather than true target directions.

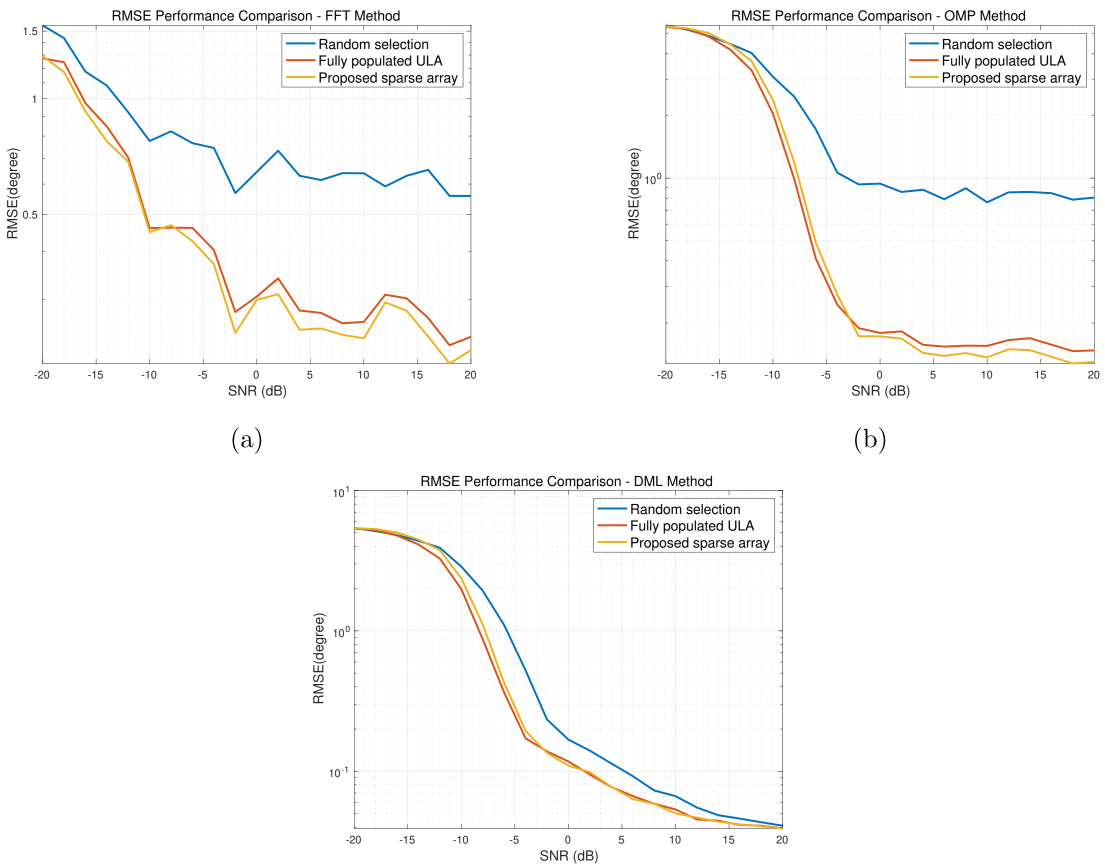

(a) (b) (c)

Figure 5.19: RMSE performance comparison between random selection, fully populated ULA, and proposed sparse array across varying SNRs: (a) FFT (b) OMP (c) DML

Since source separation remained fixed in our previous simulations, we present a more detailed examination with varying source separations to demonstrate additional performance variability. Due to the inherent limitations of FFT and OMP approaches, we focus exclusively on results from the super-resolution DML algorithm. We reduced the DML grid size to 256 to decrease computational complexity to a more feasible load, and examine its impact on the saturation level.

As evident in the Figure 5.20, the proposed sparse array achieves performance comparable to a fully populated array across varying SNRs. Notably, with larger source separations, convergence occurs earlier. The sparse array consistently outperforms random selection across all test conditions. When comparing these results with Figure 5.19c, we observe an increased saturation level resulting from the reduced grid size, confirming that saturation levels are determined primarily by grid size rather than array configuration.

Figure 5.21 presents the RMSE comparison for our proposed sparse array across different estimation methods, with the CRLB included as a performance benchmark. Since the CRLB is an approximation valid only for high SNR values, comparing performance in low SNR regions would be not so relevant. Therefore, we restrict our SNR comparison range from 0 dB to 20 dB. When configured with sufficiently fine grid resolution, the DML method can approach the CRLB at high SNR levels. In our results, we can see the saturation level limited by the setting grid size. But before that, the convergence trend is clearly demonstrated in our results.

5.5.3 Evaluation across varying source separations

In this section, we examine the DoA estimation performance across varying source separations while maintaining a fixed SNR condition. Still, the bi-static mode of the distributed radar system will be considered here. At close source separation, the resulting aperture by random selection may not be sufficient to distinguish the targets, while the targets' phase information also fluctuates substantially. These factors produce considerable variability in detection results, widening the confidence interval beyond useful representation. Therefore, confidence intervals again have been omitted from the analysis to maintain clarity and focus on the primary performance trends.

Monte Carlo simulation is performed consisting of 500 experiments, where snapshots generated with varying noise realizations for SNR of 20 dB are simulated. As mentioned in Section 5.5.2, the array gain has been compensated for random selection and sparse array to ensure the consistent SNR definition. Two targets are simulated in each experiment with varying DoA separation, changing from $1°$ up to $10°$, in steps of $0.2°$ (i.e., targets are randomly placed in the FoV [$-60°$, $60°$], ensuring the desired separation between 2 targets is achieved). Hence, RMSE values are calculated for each run which consists of 500 experiments. The sampling point of FFT processing and search grid of DML are both 1024. The DoA search grid of OMP is divided into 1801 points over the FoV $-90°$ to $+90°$.

Figure 5.22 presents a comprehensive comparison of RMSE performance across random selection, fully populated ULA, and our proposed sparse array configurations. The results demonstrate that the proposed sparse array consistently outperforms random selection across all evaluation algorithms while achieving performance comparable to the fully populated array—despite utilizing significantly fewer elements. Upon closer examination of the FFT and OMP results, we observe a performance variation between the sparse array and fully populated ULA at approximately $9°$ source separations. This phenomenon can be attributed to the more complex SLL structure of the sparse array compared to the uniform distribution found in the ULA. Unlike the ULA's well-distributed sidelobe pattern, the sparse array's irregular element spacing creates a more intricate sidelobe structure. At specific angular separations, the interaction and overlapping of these sidelobes will affect the main

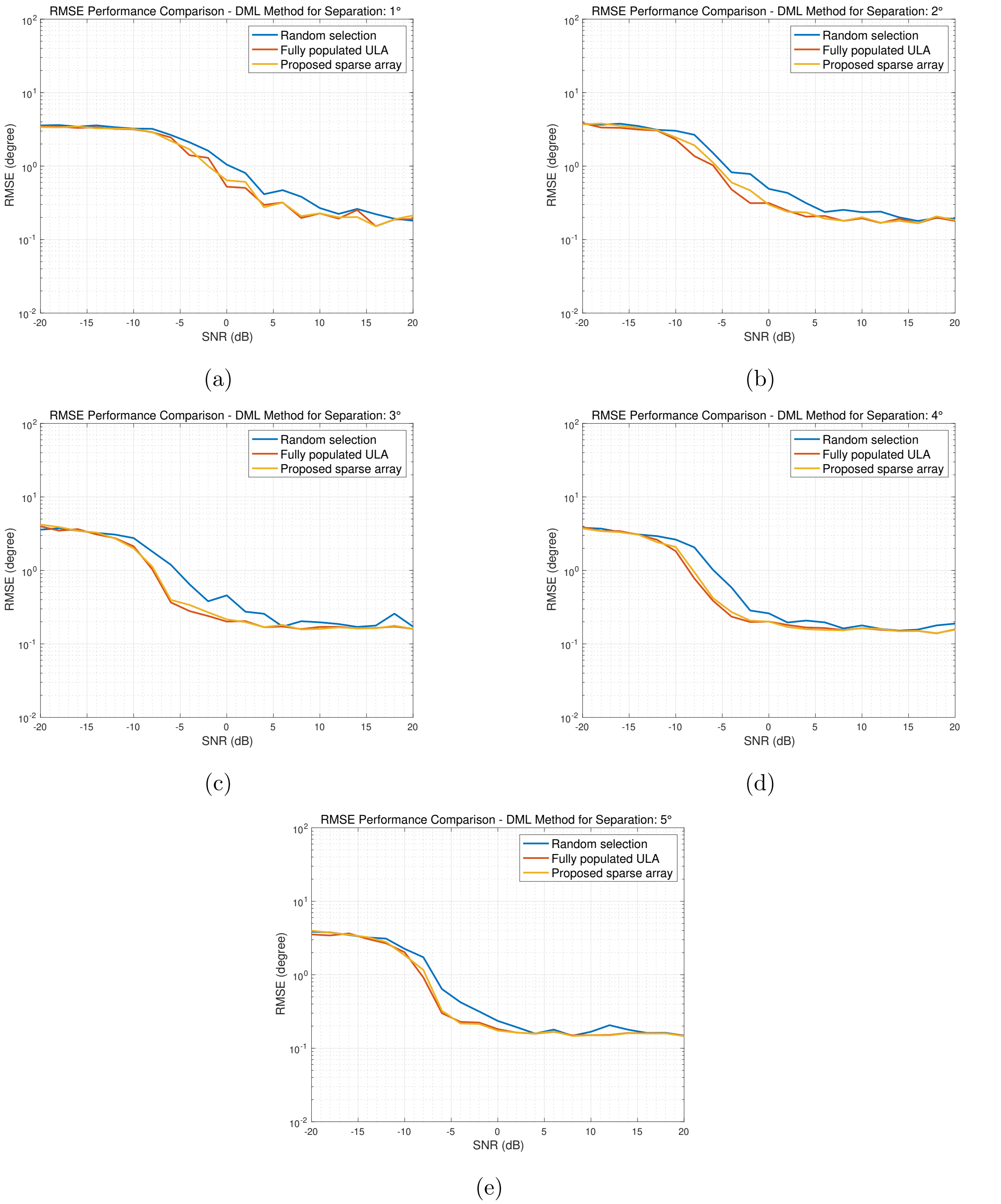

Figure 5.20: RMSE performance comparison between random selection, fully populated ULA, and proposed sparse array across varying SNRs with different source separations: (a) 1°, (b) 2°, (c) 3°, (d) 4°, (e) 5°

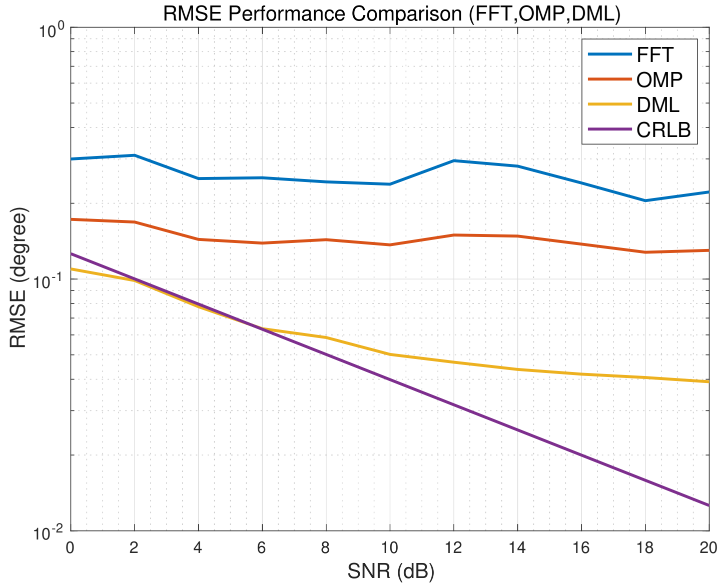

Figure 5.21: RMSE performance comparison between FFT, OMP, DML and reference CRLB for proposed sparse array

lobe positioning, resulting in different detection performance with fully populated array. This observation highlights the importance of considering sidelobe behavior when designing sparse array configurations for specific angular resolution requirements.

The results also highlight the very good capability of the DML algorithm for resolving closely spaced sources. Examining the RMSE values at minimal angular separation reveals a critical distinction in performance. While FFT and OMP algorithms fail to reliably distinguish between two targets at separations below the array's theoretical resolution limit (angular resolution limit $1.22 \cdot \frac{\lambda}{D}$ based on the virtual array aperture D of the bi-static response), the DML algorithm demonstrates remarkable super-resolution capabilities, successfully detecting and accurately localizing both targets even under these challenging conditions. The direct performance comparison across all three algorithms when applied to our proposed sparse array provides compelling evidence of DML's superior resolution characteristics, as shown in Figure 5.23. This finding emphasizes the significant advantage of employing advanced super-resolution techniques like DML in applications where detecting closely spaced targets is essential.

5.6 Conclusion

This chapter has validated our proposed approach through extensive simulations and tests, revealing significant achievements across multiple performance dimensions. The key findings from our evaluation include:

- Non-co-located array optimization: Our J-DPSC framework successfully optimized transmitter-receiver configurations in distributed radar networks,

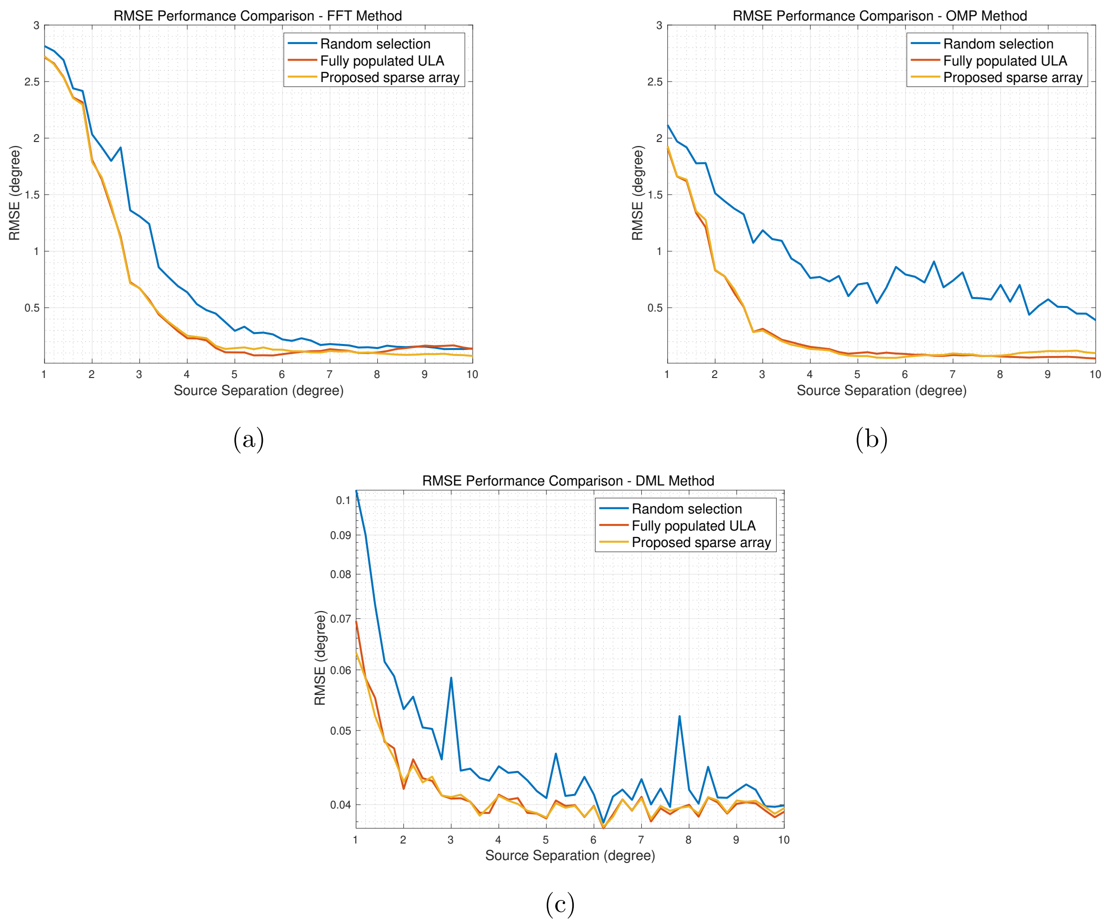

Figure 5.22: RMSE performance comparison between random selection, fully populated ULA, and proposed sparse array across varying source separations: (a) FFT (b) OMP (c) DML

achieving performance comparable to fully populated arrays while using significantly fewer elements

- Superior SLL control: Beampattern analysis confirmed that our sparse arrays provide good SLL control as an indirect benefit of the optimization process, while maintaining comparable resolution with fully populated arrays. However, since SLL control is not explicitly incorporated into the cost function, the ultimate performance when SLL becomes a direct optimization constraint remains to be investigated

- Extension to multi-sensor optimization: When extended to three-sensor networks, our approach maintained its effectiveness, though baseline selection proved critical for controlling SLL

- Near-field applicability: Performance examination revealed that the sparse array performs well in near-field regions, validating that J-DPSC design based on far-field assumptions remains highly effective

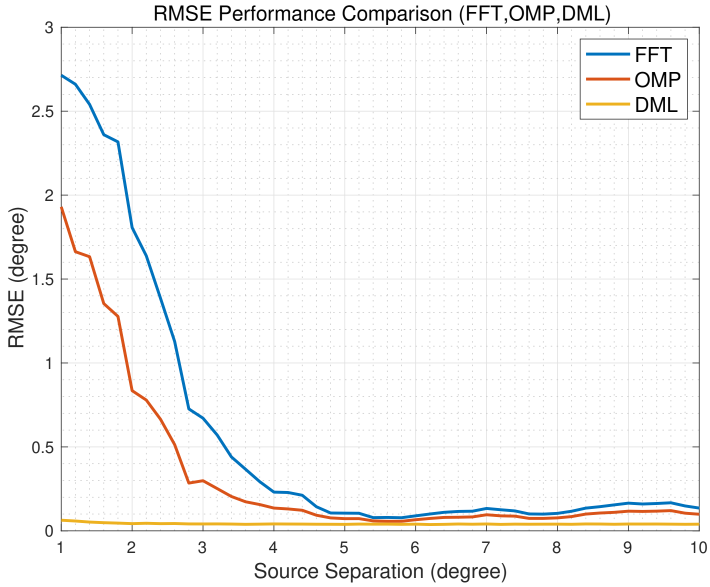

Figure 5.23: RMSE performance comparison between FFT, OMP, DML for proposed sparse array

- Consistent performance advantage: Monte Carlo simulations across varying SNRs confirmed that our proposed sparse arrays consistently outperform random selection and match fully populated arrays' performance at high SNR levels (after compensating for the lower array gain resulting from fewer active elements)
- Super-resolution capabilities: Source separation analysis demonstrated excellent resolution performance, with DML achieving super-resolution even below conventional resolution limits across different algorithms (FFT, OMP, DML)

While our optimization strategy lacks global minimum guarantees, this limitation is effectively mitigated by our ability to generate and manually evaluate multiple near-optimal solutions based on their angular resolution and sidelobe performance characteristics.

Our evaluation highlights fundamental trade-offs between resolution and sidelobe suppression in sparse array design. The results conclusively prove that properly optimized sparse arrays can achieve performance similar to fully populated arrays while maintaining significantly lower hardware complexity, validating the effectiveness of our probabilistic sampling approach for practical radar applications requiring high angular resolution with limited hardware resources.

Conclusion and Future work 6

6.1 Conclusion

This thesis has presented a novel approach to sparse antenna array design for distributed radar systems through the development of Joint Deep Probabilistic Subsampling with Cramér-Rao Bound Integration (J-DPSC). Our research addressed a gap in radar array optimization: the challenge of non-co-located joint transmitter-receiver array optimization for distributed radar configurations, while maintaining effective sidelobe level control. Throughout this work, we established a theoretical foundation through systematic CRLB analysis of both single-target and dual-target formulations. Our investigation revealed that the worst-case dual-target CRLB provides suitable performance metrics by simultaneously capturing angular resolution and sidelobe behavior. The detailed examination of phase relationships between targets offered critical insights into detection performance boundaries that guided our optimization approach.

The development of the J-DPSC methodology represents the core contribution of this thesis. By extending Deep Probabilistic Subsampling with CRLB integration, we created a flexible framework capable of optimizing sparse arrays across mono-static, bi-static, and joint operational modes. The Neighborhood Masking Mechanism we introduced ensures that theoretical optimizations remain physically realizable, bridging the gap between mathematical optimization and practical implementation.

Extensive simulations validated the performance of our proposed sparse array, demonstrating that J-DPSC sparse arrays achieve comparable or superior performance to fully populated arrays while using substantially fewer elements. Notably, our proposed configurations delivered measurable improvements in peak sidelobe levels (up to -10 dB) with minimal sacrifice in resolution (approximately 0.1° reduction). This favorable trade-off highlights the effectiveness of our optimization strategy in balancing competing performance metrics.

We successfully extended J-DPSC to three-sensor distributed radar networks, confirming the approach's adaptability to more complex configurations. This extension demonstrated how strategic positioning of center sensors can enhance detection capabilities and reduce sidelobe levels, illustrating the scalability of our method to larger network topologies. Our examination of the sparse arrays under near-field conditions validated their resilience across varying ranges and angles, with performance degradation occurring only at extremely close ranges and corresponding broadside angles. This robustness in challenging operational scenarios further supports for practical implementation of our designs. Comprehensive DoA estimation validation through Monte Carlo simulations with multiple estimation algorithms (FFT, OMP, DML) confirmed that our proposed sparse arrays consistently outperform random selection across varying SNR levels and source separations.

In summary, the J-DPSC approach developed in this thesis represents an advancement in sparse array design for automotive radar applications. By addressing the complex challenges of distributed radar configurations through a machine learning-driven approach, we have created a methodology that bridges theoretical optimization with practical implementation constraints, enabling more capable and efficient sensing systems with reduced hardware complexity.

6.2 Recommended future work

Building upon the findings in this thesis, several promising research directions are identified that could enhance and extend the capabilities of J-DPSC for optimization.

- The J-DPSC algorithm demonstrates excellent performance for one-dimensional array optimization in both mono-static and bi-static modes for distributed radar systems. However, this approach can be extended beyond the azimuth plane to also consider the elevation plane, leading to two-dimensional array optimization. The primary challenge in this extension lies in adapting the CRLB formula to incorporate two-dimensional considerations. Obviously, this adaptation would necessarily begin with revising the signal model to include additional parameters for the elevation plane. Regarding elevation detection capabilities, [40] offers an alternative perspective for three-sensor distributed radar networks. They propose that the center sensor can be shifted in the elevation plane, creating elevation shifts for different virtual array responses. Although J-DPSC requires a pre-allocated candidate set as input, the position shift for the center sensor could be mapped into a selection grid, demonstrating the potential application of J-DPSC for this innovative approach as well.

- Currently the J-DPSC method is used on its own for array optimization. However, as shown in Chapter 4, we can connect this with DoA estimation to create a joint array optimization and DoA estimation approach. For this to work well, we need a DoA estimation algorithm that is differentiable. [41] offers an efficient learning-based DoA estimation method that works well with multiple targets. Readers might want to explore algorithms designed for specific scenarios like multiple targets or limited ranges to achieve joint optimization, though this will likely increase complexity.

- In real-world radar chip implementations, we are limited by a fixed maximum candidate set. However, J-DPSC offers advantages for large antenna selection problem. The method's running time will not increase exponentially even when larger candidate sets are needed, since the trainable parameters in the DPS layer match the number of candidates. Therefore, J-DPSC has an advantage over convex optimization and other methods when dealing with large antenna selection problems. Further research could explore the limits of compression ratio and examine how effectively SLL can be suppressed in large antenna selection scenarios.

- In this thesis, we used a uniform grid spacing of $\lambda/2$ for our candidate set. Future work could explore finer grids, such as $\lambda/4$, to increase spatial sampling points which might enhance SLL suppression capabilities [9].
- An adaptive version of DPS called A-DPS was developed by [42] that includes a context vector with each selection, containing meta information from the beampattern or prior knowledge. This approach might be better suited for scenarios requiring additional constraints. The performance of A-DPS-based optimization can be studied and compared with J-DPSC.

Bibliography

[1] Sujeet Milind Patole, Murat Torlak, Dan Wang, and Murtaza Ali. Automotive Radars: A review of signal processing techniques. *IEEE Signal Processing Magazine*, 34(2):22–35, 2017.

[2] Iris Huijben, Bastiaan S Veeling, and Ruud JG van Sloun. Deep probabilistic subsampling for task-adaptive compressed sensing. In *8th International Conference on Learning Representations, ICLR 2020*, 2020.

[3] Michael Gottinger, Marcel Hoffmann, Mark Christmann, Martin Schütz, Fabian Kirsch, Peter Gulden, and Martin Vossiek. Coherent automotive radar networks: The next generation of radar-based imaging and mapping. *IEEE Journal of Microwaves*, 1(1):149–163, 2021.

[4] Pier Francesco Sammartino, Christopher J Baker, and Hugh D Griffiths. Frequency diverse MIMO techniques for radar. *IEEE Transactions on Aerospace and Electronic Systems*, 49(1):201–222, 2013.

[5] Florian Folster, Hermann Rohling, and Urs Lubbert. An automotive radar network based on 77 GHz FMCW sensors. In *IEEE International Radar Conference, 2005.*, pages 871–876. IEEE, 2005.

[6] Eric Widdison and David G Long. A review of linear multilateration techniques and applications. *IEEE Access*, 12:26251–26266, 2024.

[7] Michael Klotz and Hermann Rohling. A 24 GHz short range radar network for automotive applications. In *2001 CIE International Conference on Radar Proceedings (Cat No. 01TH8559)*, pages 115–119. IEEE, 2001.

[8] Maximilian Steiner, Karim S Osman, and Christian Waldschmidt. Cooperative target detection in a network of single-channel radar sensors. In *2019 12th German Microwave Conference (GeMiC)*, pages 91–94. IEEE, 2019.

[9] Eran Fishler, Alex Haimovich, Rick Blum, Dmitry Chizhik, Len Cimini, and Reinaldo Valenzuela. MIMO radar: An idea whose time has come. In *Proceedings of the 2004 IEEE Radar Conference (IEEE Cat. No. 04CH37509)*, pages 71–78. IEEE, 2004.

[10] Andreas Frischen, Jürgen Hasch, and Christian Waldschmidt. A cooperative MIMO radar network using highly integrated FMCW radar sensors. *IEEE Transactions on Microwave Theory and Techniques*, 65(4):1355–1366, 2017.

[11] R Feger, C Pfeffer, CM Schmid, MJ Lang, Z Tong, and A Stelzer. A 77-GHz FMCW MIMO radar based on loosely coupled stations. In *2012 The 7th German Microwave Conference*, pages 1–4. IEEE, 2012.

[12] Constantine A Balanis. *Antenna theory: analysis and design*. John wiley & sons, 2016.

[13] Alan Moffet. Minimum-redundancy linear arrays. *IEEE Transactions on antennas and propagation*, 16(2):172–175, 1968.

[14] Chun-Yang Chen and Palghat P Vaidyanathan. Minimum redundancy MIMO radars. In *2008 IEEE International Symposium on Circuits and Systems (ISCAS)*, pages 45–48. IEEE, 2008.

[15] Palghat P Vaidyanathan and Piya Pal. Sparse sensing with co-prime samplers and arrays. *IEEE Transactions on Signal Processing*, 59(2):573–586, 2010.

[16] Piya Pal and Palghat P Vaidyanathan. Nested arrays: A novel approach to array processing with enhanced degrees of freedom. *IEEE Transactions on Signal Processing*, 58(8):4167–4181, 2010.

[17] Ralph Schmidt. Multiple emitter location and signal parameter estimation. *IEEE transactions on antennas and propagation*, 34(3):276–280, 1986.

[18] Hongning Ruan, Siegfred Balon, Jian Wu, Qingping Liu, Jinghu Sun, and Xiaojun Wu. A joint design of sparse array layout and DoA algorithm for mmWave FMCW radar. In *2024 IEEE Radar Conference (RadarConf24)*, pages 1–6. IEEE, 2024.

[19] David Mateos-Núñez, María A González-Huici, Renato Simoni, Farhan Bin Khalid, Maximilian Eschbaumer, and Andre Roger. Sparse array design for automotive MIMO radar. In *2019 16th European Radar Conference (EuRAD)*, pages 249–252. IEEE, 2019.

[20] Nanbo Jin and Yahya Rahmat-Samii. Advances in particle swarm optimization for antenna designs: Real-number, binary, single-objective and multiobjective implementations. *IEEE transactions on antennas and propagation*, 55(3):556–567, 2007.

[21] Carlo Bencivenni, MV Ivashina, Rob Maaskant, and Johan Wettergren. Design of maximally sparse antenna arrays in the presence of mutual coupling. *IEEE Antennas and Wireless Propagation Letters*, 14:159–162, 2014.

[22] Yanki Aslan, Jan Puskely, Antoine Roederer, and Alexander Yarovoy. Multiple beam synthesis of passively cooled 5G planar arrays using convex optimization. *IEEE Transactions on antennas and propagation*, 68(5):3557–3566, 2019.

[23] Costas A Kokke, Mario Coutino, Laura Anitori, Richard Heusdens, and Geert Leus. Sensor selection for angle of arrival estimation based on the two-target Cramér-Rao bound. In *ICASSP 2023-2023 IEEE International Conference on Acoustics, Speech and Signal Processing (ICASSP)*, pages 1–5. IEEE, 2023.

[24] Ids Van Der Werf, Costas A Kokke, Richard Heusdens, Richard C Hendriks, Geert Leus, and Mario Coutino. Transmit and receive sensor selection using the multiplicity in the virtual array. In *2024 32nd European Signal Processing Conference (EUSIPCO)*, pages 2272–2276. IEEE, 2024.

[25] Marco Rossi, Alexander M Haimovich, and Yonina C Eldar. Spatial compressive sensing for MIMO radar. *IEEE Transactions on Signal Processing*, 62(2):419–430, 2013.

[26] Lucas L Lamberti, Ignacio Roldan, Alexander Yarovoy, and Francesco Fioranelli. Sparse Array Placement for Bayesian Compressive Sensing Based Direction of Arrival Estimation. In *2024 IEEE Radar Conference (RadarConf24)*, pages 1–6. IEEE, 2024.

[27] Ahmet M Elbir, Kumar Vijay Mishra, and Yonina C Eldar. Cognitive radar antenna selection via deep learning. *IET Radar, Sonar & Navigation*, 13(6):871–880, 2019.

[28] Oded Bialer and Noa Garnett. Optimization of antenna array configuration with a neural network. In *2021 29th European Signal Processing Conference (EUSIPCO)*, pages 1566–1570. IEEE, 2021.

[29] Konstantinos Diamantaras, Zhaoyi Xu, and Athina Petropulu. Sparse antenna array design for MIMO radar using softmax selection. *arXiv preprint arXiv:2102.05092*, 2021.

[30] Krishnasamy T Selvan and Ramakrishna Janaswamy. Fraunhofer and Fresnel distances: Unified derivation for aperture antennas. *IEEE antennas and propagation magazine*, 59(4):12–15, 2017.

[31] Jiadi Zhang. Super-resolution algorithms for target localization using multiple FMCW MIMOs. Master's thesis, Delft University of Technology, Delft, the Netherlands, 2019.

[32] Steven M Kay. *Fundamentals of statistical signal processing: estimation theory.* Prentice-Hall, Inc., 1993.

[33] L Harry and Van Trees. Optimum array processing: part IV of detection, estimation, and modulation theory. *New York: John Wiley & Sons*, 2002.

[34] Petre Stoica and Arye Nehorai. MUSIC, maximum likelihood, and Cramer-Rao bound. *IEEE Transactions on Acoustics, speech, and signal processing*, 37(5):720–741, 2002.

[35] Eric Jang, Shixiang Gu, and Ben Poole. Categorical reparameterization with gumbel-softmax. *arXiv preprint arXiv:1611.01144*, 2016.

[36] Diederik P Kingma. Adam: A method for stochastic optimization. *arXiv preprint arXiv:1412.6980*, 2014.

[37] David Mateos-Núñez, Renato Simoni, María A González-Huici, and Aitor Correas-Serrano. Design of mutually incoherent arrays for DoA estimation via group-sparse reconstruction. In *2019 IEEE Radar Conference (RadarConf)*, pages 1–6. IEEE, 2019.

[38] Zai Yang, Jian Li, Petre Stoica, and Lihua Xie. Sparse methods for direction-of-arrival estimation. In *Academic Press Library in Signal Processing, Volume 7*, pages 509–581. Elsevier, 2018.

[39] Philipp Heidenreich. Antenna array processing: Autocalibration and fast high-resolution methods for automotive radar. 2012.

[40] Daniel Schindler, Tobias Schmid, and Cornelius Kaiser. On system design of coherent cooperative automotive radar sensor networks. In *2024 21st European Radar Conference (EuRAD)*, pages 296–299. IEEE, 2024.

[41] Jihwan Youn, Satish Ravindran, Ryan Wu, Jun Li, and Ruud van Sloun. Circular convolutional learned ISTA for automotive radar DOA estimation. In *2022 19th European Radar Conference (EuRAD)*, pages 273–276. IEEE, 2022.

[42] Hans Van Gorp, Iris Huijben, Bastiaan S Veeling, Nicola Pezzotti, and Ruud JG Van Sloun. Active deep probabilistic subsampling. In *International Conference on Machine Learning*, pages 10509–10518. PMLR, 2021.

Appendix A

A.1 The code of DPS with NMM

This appendix provides the implementation details of the DPS layer with NMM for sparse array design. The code below extends the foundational work presented by Huijben et al. (2020) in their Deep Probabilistic Subsampling framework [2].

```
# %% import dependencies
import torch
import torch.nn as nn
import torch.nn.functional as F
import numpy as np

class DPS(nn.Module):
        def __init__(self, parameters):
                super(DPS, self).__init__()

                self.mux_in = parameters['mux in']
                self.mux_out = parameters['mux out']
                self.temperature = parameters['temperature']
                self.device = parameters['device']
                self.compression = parameters['compression']
                self.neighbor_radius = 1

                self.gumbel = torch.distributions.gumbel.Gumbel(0, 1)

                #Forcing the index 0 has the largest probs at the beginning
                logits_initialization = torch.randn(self.mux_in) / self.
                    compression
                max_index = torch.argmax(logits_initialization)
                logits_initialization[0], logits_initialization[max_index]
                    = (
                        logits_initialization[max_index].clone(),
                        logits_initialization[0].clone()
                )

                self.logits = nn.Parameter(logits_initialization)

        def apply_neighborhood_mask(self, mask, selected_indices, k):
                """Apply masking to the selected indices and their
                    neighbors for channel k"""
                # Create batch indices for vectorized operations
                batch_size = selected_indices.size(0)
                batch_indices = torch.arange(batch_size, device=self.device
                    )
```

```python
        # Initialize temporary mask for this iteration
        temp_mask = torch.zeros_like(mask)

        # Set -inf at the selected indices for future channels
        for j in range(k + 1, self.mux_out):
            temp_mask[batch_indices, selected_indices, j] = -np.inf

            # Mask the neighborhood using bounds checking
            for offset in range(1, self.neighbor_radius + 1):
                # Mask neighbors to the right
                right_indices = selected_indices + offset
                valid_right = right_indices < self.mux_in
                if valid_right.any():
                    temp_mask[batch_indices[valid_right], right_indices[valid_right], j] = -np.inf

                # Mask neighbors to the left
                left_indices = selected_indices - offset
                valid_left = left_indices >= 0
                if valid_left.any():
                    temp_mask[batch_indices[valid_left], left_indices[valid_left], j] = -np.inf

        # Combine with existing mask
        return mask + temp_mask


    def forward(self, x):
        # find the batch size
        batch_size = x.size(0)

        # create perturbed logits with the same dimensions as original
        noise = self.gumbel.sample((batch_size, self.mux_in, 1)).repeat(1, 1, self.mux_out).to(self.device)  # [batch_size, mux_in, mux_out]
        perturbed_logits = torch.transpose(self.logits.repeat(batch_size, self.mux_out, 1), 1, 2) + noise  # [batch_size, mux_in, mux_out]

        # Initialize mask tensor to track available positions
        masking_matrix = torch.zeros(batch_size, self.mux_in, self.mux_out).to(self.device)

        # Track selected indices for debugging/visualization
        selected_indices = torch.zeros(batch_size, self.mux_out, dtype=torch.long).to(self.device)

        # Perform sequential Top-1 sampling
```

```python
        for k in range(self.mux_out):
            # Apply current mask to perturbed logits (focus on first channel for selection)
            masked_perturbed_logits = perturbed_logits[:, :, k] + masking_matrix[:, :, k]

            # Select the top-1 element for each batch
            _, top_indices = torch.max(masked_perturbed_logits, dim=1)

            selected_indices[:, k] = top_indices

            # Apply neighborhood masking in a vectorized way
            masking_matrix = self.apply_neighborhood_mask(masking_matrix, top_indices, k)


        # Create masked_logits by applying the final mask to perturbed_logits
        masked_logits = perturbed_logits + masking_matrix

        # Calculate soft sample matrix (probabilities) using softmax
        soft_sample_matrix = F.softmax(masked_logits / self.temperature, dim=1)

        # Collapse soft sample matrix by summing across the third dimension
        soft_sample_matrix_collapsed = torch.sum(soft_sample_matrix, dim=2)

        # Return the soft matrices
        return soft_sample_matrix, soft_sample_matrix_collapsed
```

A.2 Accepted paper for EuRAD 2025, September 24-26, Utrecht, NL

Design of Sparse MIMO Radar Antenna Arrays Using DPS with Integrated CRB Evaluation

Jiaqi Li[#, $1], Arie G.C. Koppelaar[#2], Anusha Ravish Suvarna[#3], Francesco Fioranelli[$4]

[#]NXP Semiconductors, The Netherlands

[$]Microwave Sensing Signals & Systems (MS3) Group, Delft University of Technology, The Netherlands

{[1]jiaqi.li, [2]arie.koppelaar, [3]anusha.ravishsuvarna}, [4]F.Fioranelli

***Abstract*— This paper presents a Joint Deep Probabilistic Subsampling framework with Cramér-Rao Bound (CRB) Integration (J-DPSC), which optimizes both transmit and receive antenna selection independently, enabling robust DoA estimation in mono-static and bi-static radar modes. Our method incorporates a differentiable worst-case CRB computation for end-to-end optimization. Additionally, sidelobe level (SLL) suppression is naturally integrated into the training process through data constraints, without requiring explicit penalty terms. Compared to prior methods, J-DPSC significantly reduces model complexity and the number of trainable parameters while maintaining high DoA estimation accuracy. Beampattern results demonstrate the effectiveness of our approach in improving performance with an acceptable SLL, making it well-suited for practical sparse array design in automotive radar applications.**

***Keywords*— Probabilistic subsampling, CRB, sparse antenna array, monostatic, bistatic, deep learning, distributed radar network**

I. Introduction

Automotive radar plays a crucial role in accurate target detection and localization, where Direction of Arrival (DoA) estimation is a key component. Achieving high angular resolution requires a larger aperture, which drives the demand for sparse array design—an approach that selects a subset of sensors to maximize resolution while minimizing hardware cost. The challenge lies in efficiently selecting a small number of elements while maintaining acceptable SLL to avoid performance degradation.

Various methods have been explored for sensor selection decision-making. CRB-based convex optimization is a widely used approach [1], but it is typically designed for single domain selection and requires complex convex relaxation. Recently, learning-based approaches such as Learn-to-Select [2] and Jointly Learning [3] framework have emerged, enabling data-driven antenna selection. However, existing solutions are often still restricted to single domain selection or involve complex models like Complex Learned FISTA (CL-FISTA) network, which introduces unnecessary redundancy in learning the compression matrix.

To address these limitations, we propose a Joint Deep Probabilistic Subsampling framework with CRB integration (J-DPSC) that independently optimizes transmitter and receiver selection, allowing for both mono-static and bi-static mode optimization. Our method integrates a differentiable worst-case CRB computation as a task model, ensuring low complexity training. Additionally, by incorporating data constraints during training, our approach inherently regulates SLL suppression without requiring explicit penalty terms. The proposed technique is evaluated through beampattern analysis, demonstrating its ability to generate a well-optimized sparse array while maintaining acceptable SLL.

The rest of this paper is structured as follows: Section II presents the proposed methodology. Section III details the CRB relaxation and J-DPSC framework. Section IV discusses the training setup and evaluation results. Finally, Section V concludes the paper with key findings.

II. Methodology

A. Signal model

We start from a candidate set of antenna array elements, from which a subset of elements is selected that performs better than any other subset of the same size according to the chosen cost function. If we denote the single-snapshot received samples after Range-Doppler processing from an array of M channels after MIMO decoding as $\boldsymbol{y}$, the signal model corresponding to K targets can be expressed as follows:

$$\boldsymbol{y} = \boldsymbol{A}\boldsymbol{s} + \boldsymbol{n} \tag{1}$$

where $\boldsymbol{y} \in \mathbb{C}^{M\times 1}; \boldsymbol{s} \in \mathbb{C}^{K\times 1}; \boldsymbol{A} \in \mathbb{C}^{M\times K}; \boldsymbol{n} \in \mathbb{C}^{M\times 1}$. $\boldsymbol{s}$ is the impinging source vector, $\boldsymbol{n}$ is the noise vector, and $\boldsymbol{A}$ represents a collection of steering vectors for multiple targets. The steering vector $\boldsymbol{a}(\theta)$ represents the impinging signal from a target present at an angle θ from the array elements. The expression is given as

$$\boldsymbol{A} = [\boldsymbol{a}(\theta_1)\ \boldsymbol{a}(\theta_2)\ \dots\ \boldsymbol{a}(\theta_K)] \tag{2}$$

$$\boldsymbol{a}(\theta) = [1, e^{\frac{j2\pi d \sin\theta}{\lambda}}, e^{\frac{j4\pi d \sin\theta}{\lambda}}, \dots, e^{\frac{j(M-1)2\pi d \sin\theta}{\lambda}}]^T \tag{3}$$

L array elements can be selected from the full candidate set by multiplying a selection matrix $\boldsymbol{\Phi_P}$ with received signal $\boldsymbol{y}$. The structure and property of $\boldsymbol{\Phi_P}$ are as follows:

$$\boldsymbol{\Phi_P} \in \{0,1\}^{L\times M}, \quad \boldsymbol{\Phi_P}^T\boldsymbol{\Phi_P} = \boldsymbol{P} = \mathrm{diag}(\boldsymbol{p}), \quad \boldsymbol{\Phi_P}\boldsymbol{\Phi_P}^T = \boldsymbol{I}$$

and $\boldsymbol{p} = [p_1 \dots p_M]^T \in \{0,1\}^M$ is a binary selection vector where the L ones indicate the corresponding selected array elements, and zeros indicate the elements that are not selected.

In order to jointly learn selection vector for transmitters and receivers in this work, a structured subsampling is applied to the signal model. Data is compressed by specifying active transmitters L_T and receivers L_R from the full candidate transmitters M_T and receivers M_R, which is represented by selection matrices: $\boldsymbol{\Phi_T} \in \mathbb{R}^{L_T \times M_T}$, $\boldsymbol{\Phi_R} \in \mathbb{R}^{L_R \times M_R}$. These matrices follow a row-wise one-hot structure, and the selection matrix $\boldsymbol{\Phi_P}$ can be decomposed into $\boldsymbol{\Phi_P} = \boldsymbol{\Phi_T} \otimes \boldsymbol{\Phi_R}$. The $\otimes$ denotes the Kronecker product and the virtual antenna array in a MIMO is calculated as $L = L_T \times L_R$ and $M = M_T \times M_R$.

By applying this principle, the subsampled received signal $\boldsymbol{Z}$ is expressed as:

$$\boldsymbol{z} = \boldsymbol{\Phi_P} * \boldsymbol{y} = (\boldsymbol{\Phi_T} \otimes \boldsymbol{\Phi_R}) * \boldsymbol{y} \tag{4}$$

B. DPS: Deep Probabilistic Subsampling

The subsampling part of the proposed algorithm is based on Deep Probabilistic Subsampling (DPS) method [4]. The DPS method effectively integrates subsampling in an end-to-end deep learning model, but learns a static pattern for all data points. The formulation of the sparse array design as an antenna selection problem allows us to use DPS as a method to optimize the design.

The selection matrix is formulated by considering each row as a sample drawn from a categorical distribution. Since neural networks struggle with discrete variables, a common solution is the Gumbel-Softmax reparameterization [5]. In this approach, an unnormalized log-probability vector $\boldsymbol{p}$ (logits) is transformed into a one-hot row vector $\boldsymbol{\phi}$, where each p_i represents the probability that ϕ_i is set to 1.

The Gumbel-max trick generates a mask matrix A by perturbing unnormalized logits $\phi_{l,m}$ with i.i.d. Gumbel noise $e_{l,m} \sim \text{Gumbel}(0,1)$. Row l of the mask matrix is given as:

$$A_{l,:} = \text{one-hot}_M \left(\arg\max_m \{w_{l-1,m} + \phi_{l,m} + e_{l,m}\} \right) \tag{5}$$

where $w_{l-1,m} \in \{-\infty, 0\}$ ensures sampling without replacement by masking previously selected indices.

For backpropagation, the sampling process is relaxed using the Gumbel-Softmax trick:

$$\nabla_{\phi_l} A_{l,:} = \nabla_{\phi_l} \mathbb{E}_{e_l} \left[\text{softmax}_\tau \{w_{l-1,m} + \phi_{l,m} + e_{l,m}\} \right] \tag{6}$$

where $\tau > 0$ is a temperature parameter controlling the smoothness of the sampling distribution. As $\tau \to 0$, the softmax converges to the one-hot argmax. Although this introduces biased gradients, in practice it has been shown to work effectively [4]. τ is kept fixed during training.

In order to facilitate the antenna element selection and fit in the following defined loss function, the 1-D logits are generated from this layer. That is to say, the soft subsampling will be used for the following computation.

III. Joint Deep Probabilistic Subsampling with CRB

A. CRB Relaxation

CRB defines the theoretical lower limit of estimation error achievable by any unbiased estimator [6]. It provides a benchmark for DoA estimation performance through deterministic calculations. From this perspective, it is a logical metric for sparse antenna array design. To integrate it with the DPS structure, the CRB formula is relaxed to make it differentiable and ensure back-propagation.

The worst-case dual-target CRB is used here because of its sensitivity [7]. Using it as a loss function for the proposed algorithm can provide a resulting array with acceptable SLL while maintaining a low value of CRB.

By integrating the selection matrix $\boldsymbol{\Phi_P}$ in (1) and CRB formula [1], [7], the worst-case dual-targets CRB is given as :

$$CRB(\boldsymbol{\varphi}, \boldsymbol{p}) = \frac{\sigma^2}{2T} (\text{Re}\{\boldsymbol{H}(\boldsymbol{p}) \odot \boldsymbol{R}\})^{-1} \tag{7}$$

$$\boldsymbol{H}(\boldsymbol{p}) = \boldsymbol{D}^H \boldsymbol{P} \boldsymbol{D} - \boldsymbol{D}^H \boldsymbol{P} \boldsymbol{A} (\boldsymbol{A}^H \boldsymbol{P} \boldsymbol{A})^{-1} (\boldsymbol{D}^H \boldsymbol{P} \boldsymbol{A})^H \tag{8}$$

$$\boldsymbol{D} = \left[\left. \frac{\partial \boldsymbol{a}(\varphi)}{\partial \varphi} \right|_{\varphi=\varphi_1} \quad \left. \frac{\partial \boldsymbol{a}(\varphi)}{\partial \varphi} \right|_{\varphi=\varphi_2} \right], \quad \boldsymbol{R} = \frac{\boldsymbol{s}\boldsymbol{s}^T}{T} \tag{9}$$

The noise power σ^2 is standardized to 1, ensuring that the signal power in the diagonal elements of the signal spectral matrix $\boldsymbol{R}$ is regulated by the Signal-to-Noise Ratio (SNR).

An additional phase relationship term is introduced to the off-diagonal element of the signal spectral matrix $\boldsymbol{R}$ to consider for worst-case CRB [7], which is shown as:

$$R_{12} = \sqrt{R_{11} R_{22}} \exp\left[j[\arg(H_{12}] \right] \tag{10}$$

To obtain a scalar objective for the loss function, we propose to use the worst-performing target:

$$\mathcal{L}_{CRB} = \max_{\boldsymbol{\varphi}} \; trace(CRB(\boldsymbol{\varphi}, \boldsymbol{p})) \tag{11}$$

To reduce complexity and satisfy the assumptions of the single snapshot signal model, T in Eq. (9) is set to 1 in practical simulations. The total loss function consists of two components: the CRB loss $\mathcal{L}_{CRB}$ and an entropy-based penalty term $\mathcal{L}_s$, which encourages training towards one-hot distributions [4]. The combined loss function is formulated as:

$$\mathcal{L} = \mu \mathcal{L}_s + \lambda \mathcal{L}_{CRB} \tag{12}$$

where λ and μ are penalty multipliers that control the relative importance of the CRB loss and the entropy regularization term. Here, $\mathcal{L}_s$ is defined as:

$$\mathcal{L}_s = - \sum_{l=1}^{L} \sum_{m=1}^{M} \pi_{l,m} \log \pi_{l,m} \tag{13}$$

where $\pi_{l,m}$ is the normalized logits from $\phi_{l,m}$.

B. J-DPSC Framework for Mono-static Mode

Using the DPS structure and CRB relaxation explained in section II, a method is proposed to achieve joint optimization for transmitters and receivers. The operational procedure of proposed J-DPSC is illustrated in Algorithm 1.

Two parallel networks are trained simultaneously to independently optimize transmitter and receiver arrays. The logits vectors are initialized following a normal distribution

Algorithm 1 Proposed J-DPSC

Input: Training dataset: $(DoAs, SNRs)$, parameters of selection candidates and subsampling: M_T, M_R, L_T, L_R, number of iterations: N_{iter}
Initialization:
  - Logits vectors: $\boldsymbol{\phi_T}, \boldsymbol{\phi_R} \sim \mathcal{N}(0, \frac{1}{CR_T \times CR_R})$
  - Temperature: $\tau = 0.2$
  - Learning rate: $lr = 5e-2$
for $i = 1$ to N_{iter} **do**
  Draw a random subset of training dataset
  In parallel compute soft selection vectors:
    - $\tilde{\boldsymbol{\phi_T}} = \text{softmax}(\boldsymbol{\phi_T}, w, e, \tau)$
    - $\tilde{\boldsymbol{\phi_R}} = \text{softmax}(\boldsymbol{\phi_R}, w, e, \tau)$
  Unified soft selection vector: $\tilde{\boldsymbol{\phi_P}} = \tilde{\boldsymbol{\phi_T}} \otimes \tilde{\boldsymbol{\phi_R}}$
  Compute the loss: $\mathcal{L} = \mu\mathcal{L}_s + \lambda\mathcal{L}_{CRB}$
  Update learning rate: $lr_{new} = 0.96 * lr$
  Use Adam optimizer to update logits by minimizing $\mathcal{L}$
end for
Output: Trained soft selection vectors $\tilde{\boldsymbol{\phi_T}}, \tilde{\boldsymbol{\phi_R}}$.

with a variance of $\frac{1}{CR_T \times CR_R}$, where CR (compression ratio) represents the ratio of selected elements to the full array elements. As training progresses, the output of each DPS layer—normalized logits—gradually approximates the binary selection vector. Once the unified soft selection vector is obtained, it is paired with the corresponding data and used to compute the loss.

C. J-DPSC Framework for Bi-static Mode

A key capability of a distributed radar network is its ability to measure both cross-paths and direct paths between two sensors. This feature enables the network to capture bi-static responses, where the transmitter and receiver are non-co-located, provided that the synchronization requirements are met. The proposed J-DPSC framework for bi-static mode is shown in Fig. 1.

In the setup, we choose to have two sensors that have mirror symmetry with reference to their antenna arrays since two bi-static responses will result in a larger virtual array around the center. Fig. 2 illustrates the corresponding geometry, where the target is located in the far-field region relative to each individual sensor; however, the baseline primarily determines the Fraunhofer distance of the distributed radar system. As a result, only two parallel DPS layers are required to enable bi-static mode selection. The trained selection vector (shown in the dotted frame in Fig. 1) indicates that a single trained logits vector can represent selections for transmitters or receivers at different locations. After applying the Kronecker product, the unified selection vector is concatenated with its flipped version to represent soft selection across all bi-static responses (the two bi-static virtual arrays are flipped versions of each other due to the symmetrical placement of the sensors as shown in Fig. 2). The subsequent forward pass and backpropagation proceed as outlined in Algorithm 1, ensuring optimal sensor selection through end-to-end differentiable learning.

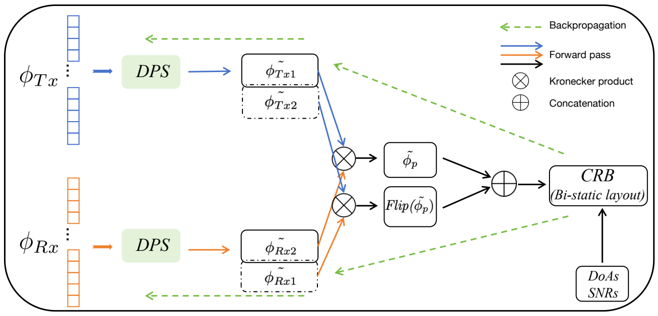

Fig. 1. Proposed J-DPSC framework for bi-static mode

IV. Evaluation

A. Training setup

We train the model using 51,200 samples over 120 epochs, with each epoch consisting of 512 simulated data samples. To account for SLL considerations, specific constraints are applied during data generation. The first DoA angle is always placed at 0° (broadside), while the second DoA angle is varied within a source separation range of 1.5° to 15°, resulting in a total angular range of [-15°, 15°]. Additionally, we introduce two different SNR's [20 dB, 10 dB] to enhance the CRB's sensitivity to SLL. This approach helps suppress SLL around the broadside while ensuring a low CRB, leading to more robust and practical sparse antenna array design.

The Adam optimizer is employed for stochastic optimization, with hyperparameters β_1 = 0.9 , β_2 = 0.999 , and $\epsilon = 1e-7$. The initial learning rate is set to $5e-2$ and follows an exponential decay strategy with a decay parameter of 0.96, helping to prevent convergence to local minima.

Given the physical size of the envisaged radar chip (6cm, around 16 wavelengths for frequency of 79GHz), the candidate positions for transmitters and receivers are defined as [0:1:15] and [-16:1:0], respectively, with positions normalized by wavelength / 2. From these candidate positions, four elements are selected for both transmitters and receivers. The proposed J-DPSC framework achieves a compression ratio CR of 6%.

B. Results

Results are shown for a system consisting of 2 sensors as explained in Section III-C. The selection results for bi-static mode are illustrated in Fig. 2. We do not claim a specific value for the baseline here; the baseline does not affect the design as we only look at the bi-statics. The number in Fig. 2 indicates the selected normalized position of transmitters and receivers.

The beampattern for the selected result is shown in Fig. 3. For comparison, we also present the mono-static beampattern for the selected array, as using bi-static mode requires certain prerequisites, such as sensor synchronization and the target being visible to both sensors. In some scenarios, only a single sensor can be operated, so we demonstrate that the mono-static layout also performs well for DoA estimation.

It is important to emphasize that this illustration serves purely as a simplified representation. The matched filter is used

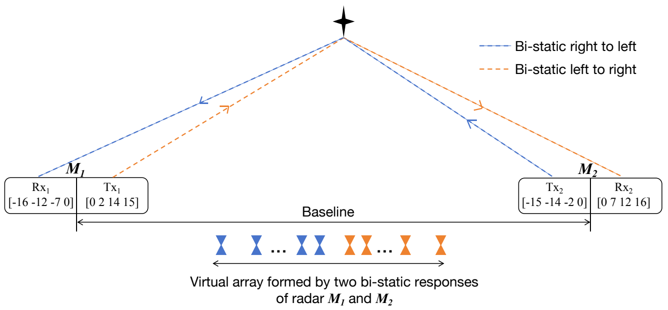

Fig. 2. Selection results and array visualization for bi-static mode

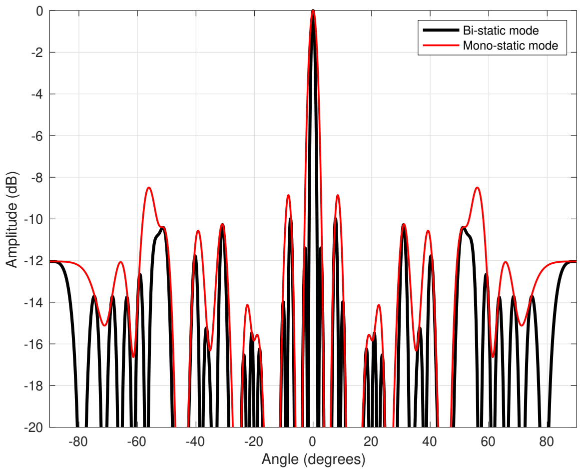

Fig. 3. Beampattern visualization for bi-static mode and mono-static mode when target located at exact broadside

here to generate the result. Thus, this visualization should not be interpreted as an exact measure of estimation performance.

The results obtained using the proposed J-DPSC algorithm in this paper are compared to a full uniform linear array (ULA) with 63 elements. Tab. 1 shows that the proposed sparse array can achieve comparable resolution with the full array while maintaining acceptable SLL. Moreover, the proposed algorithm optimizes the transmit and receive elements individually, hence a practical sensor can be realized with this approach.

Table 1. Performance Comparison of Different Array Layouts

Method	**Peak SLL (dB)**	**Resolution (deg)**
ULA-63	-13.25	1.60
J-DPSC (proposed method)	-9.99	1.60

Fig. 4 illustrates the beampattern performance of the proposed sparse array under bi-static mode, evaluated for two different settings: worst-case (same phase) and best-case (orthogonal phase) relations. The results demonstrate the array's ability to distinguish two closely spaced targets at 3° separation, with the best-case setting (black line) achieving lower sidelobe levels compared to the worst-case setting (red line). We can examine the effect of phase relationship between two targets on beampattern.

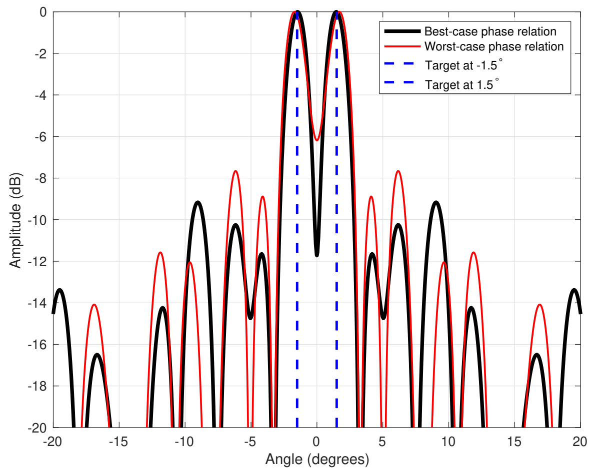

Fig. 4. Beampattern visualization for worst-case (same) and best-case (orthogonal) phase relation on bi-static mode

V. Conclusion

This paper presents Joint Deep Probabilistic Subsampling with CRB Integration (J-DPSC) for sparse antenna array design in mono-static and bi-static configurations. By incorporating structured subsampling and differentiable CRB computation, J-DPSC independently optimizes transmitter and receiver selection, enabling flexible mono-static and bi-static sensor configurations. This separate optimization of Tx and Rx makes the approach highly adaptable for practical sensor design. Not shown for conciseness, but our approach performs well also at high CR and for larger antenna selection problems, as it avoids combinatorial explosion issues and reduces the number of training parameters. Additionally, integrating dynamic range, Field-of-View, and source separation constraints into training effectively regulates the SLL without explicit penalty terms. For comprehensive details on this work, readers are referred to [8].

References

[1] C. A. Kokke, M. Coutino, L. Anitori, R. Heusdens, and G. Leus, "Sensor selection for angle of arrival estimation based on the two-target Cramér-Rao bound," in *IEEE International Conference on Acoustics, Speech and Signal Processing (ICASSP)*, IEEE, 2023, pp. 1–5.

[2] K. Diamantaras, Z. Xu, and A. Petropulu, "Sparse antenna array design for MIMO radar using softmax selection," *arXiv preprint arXiv:2102.05092*, 2021.

[3] H. Wang, Y. Zhou, E. Pérez, and F. Römer, "Jointly learning selection matrices for transmitters, receivers and Fourier coefficients in multichannel imaging," in *IEEE International Conference on Acoustics, Speech and Signal Processing (ICASSP)*, IEEE, 2024, pp. 8691–8695.

[4] I. A. Huijben, B. S. Veeling, K. Janse, M. Mischi, and R. J. van Sloun, "Learning sub-sampling and signal recovery with applications in ultrasound imaging," *IEEE Transactions on Medical Imaging*, vol. 39, no. 12, pp. 3955–3966, 2020.

[5] E. Jang, S. Gu, and B. Poole, "Categorical Reparameterization with Gumbel-Softmax," *arXiv preprint arXiv:1611.01144*, 2016.

[6] P. Stoica and A. Nehorai, "MUSIC, maximum likelihood, and Cramer-Rao bound," *IEEE Transactions on Acoustics, speech, and signal processing*, vol. 37, no. 5, pp. 720–741, 2002.

[7] H. L. Van Trees, *Optimum Array Processing: Part IV of Detection, Estimation, and Modulation Theory*. John Wiley & Sons, 2002.

[8] J. Li, "Design of sparse MIMO radar antenna arrays using DPS with integrated CRB evaluation," *M.Sc. thesis, TU Delft*, 2025.